PRODUCTION OF PROTON–RICH NUCLEI BETWEEN NICKEL AND ZIRCONIUM

By

MICHAEL FLORIAN MOHAR

A DISSERTATION

Submitted to
Michigan State University
in partial fulfillment of the requirements
for the Degree of

DOCTOR OF PHILOSOPHY

Department of Chemistry

1991

ABSTRACT

Production of Proton–Rich Nuclei Between Nickel and Zirconium

by

Michael Florian Mohar

Two experimental methods were explored to produce nuclei along the proton–drip line between nickel and zirconium. The initial study was the fusion of an E/A = 8 MeV ^{36}Ar beam with a ^{40}Ca target using the K500 cyclotron at the National Superconducting Cyclotron Laboratory, Michigan State University. The evaporation residues were collected and identified using the S320 spectrometer equipped with a newly designed focal plane detector. The goals of this experiment were twofold: first, to identify any new isotopes produced in the reaction; and second, to measure the zero degree momentum distributions of the products to learn more about the reaction mechanism. The performance of the new detector was limited, and the results were difficult to interpret. However, a viable analysis method is demonstrated and suggestions are made for the improvement of the detection system.

The second study utilized the projectile-fragmentation mechanism to produce exotic nuclei. An E/A= 65 MeV ^{78}Kr beam from the K1200 cyclotron was used in conjunction with the newly commissioned A1200 beam analysis device to create new proton–rich isotopes. The purpose of this experiment was to identify exotic nuclei at the proton–drip line and measure their production rates so that further experiments could be designed to measure their halflives, decay modes, and masses. Six new isotopes, ^{65}As, ^{61}Ga, ^{62}Ge, ^{63}Ge, ^{69}Br, and ^{75}Sr, were identified in this experiment, and

the observation of these nuclei is discussed in terms of the astrophysical rp-process. It was also notable that ^{73}Rb, another nucleus important to the rp-process, was not produced in this experiment.

The relative merits of the two isotope production methods illustrated in this work are difficult to compare because the results of the fusion/evaporation are uncertain. However future studies of exotic nuclei along the proton–drip line are discussed.

A very special professor went far beyond his normal classroom duties to introduce me to the wonders of nuclear science when I was a freshman chemistry student at The University of Chicago. His fatherly wisdom and patience made a difference in both my career and my personal life. Therefore, I respectfully dedicate this dissertation to the fond memories I have of Professor Nathan Sugarman.

Acknowledgements

When I first put my dissertation on display in the library before my defense a number of people stopped by my office to point out that I hadn't written the Acknowledgements section yet. Very few seemed all that interested in the contents of my work, but rather with what I had to say about my fellow workers. Much of that may have to do with my own personality and what people were expecting from me, but this certainly made me stop and think about what I was really supposed to say here.

Unfortunately, after all that thought the best I could come up with is that I should just use the space to acknowledge stuff. So here goes:

I acknowledge that graduate school is not always a lot of fun. In fact, I can honestly say that I didn't want to be here at times. There were mornings when I spent an hour convincing myself that I really should go to work, and an equal number of days where I simply stayed in bed. Read Chapter Two and tell me how much you'd like to face that data each day!

I acknowledge that graduate school is often a lot of fun. There were days when I couldn't leave the lab. I've got to admit, I love doing experiments. It didn't matter if they were my experiments or not – I loved doing them all. In particular, the work in Chapter Three was ecstasy! I even enjoyed working on the analysis of that one.

I acknowledge that I got to work with some really cool people here at the cyclotron lab. The professors, staff, and technicians are all four-star in my book. Allow me to enumerate: My boss, David J. Morrissey (A.K.A "The Boss") put up with as much as was humanly possible from me. He taught me a great deal about our science, and I hope that I can live up to his expectations. I also hope that I taught him more than to carefully screen his prospective students. Then there's Walt Benenson (A.K.A. "Dr. Walt", "Dr. Mantra", "I know a good restaurant...") who was both

a scientific and spiritual advisor to me. He's one of those people who can look at a spectrum that has everyone else completely baffled and come up with a statement like, "Obviously this is a (blank) problem. We saw the very same effect in an experiment I did back in the late 60's..." He was always right, too! Dr. Walt was also the one who told me when my aura was out of wack and my mantra needed adjustment. Brad Sherrill (A.K.A "The Dad") was also very important to my work at MSU, which was basically a continuation of his own dissertation. He helped immensely in the S320 work, and we couldn't have done the isotope identifications if he hadn't built that A1200 mass separator. John Winfield (A.K.A. "Lord Melbeck") made my life interesting with with all the "little bugs" we found in some of the analysis codes. We had a good time wrenching on the S320 together, too. Michael Wiescher and Joachim Görres (no known aliases) from Notre Dame University assisted me with the astrophysics and provided some figures and text. Ron Fox (A.K.A. "RF") helped me learn a little about computers and sushi... they don't mix. And who could forget those starry, −40 degree nights (C or F, your choice) in Saskatoon, Saskatchewan, with Jim Clayton (A.K.A. "JC", "Bhudda", "Stop snoring or else!")? We, along with Takeshi Murakami (A.K.A. "Ken") made up Team Golden of High Energy Gamma World Tour '87 (album available on 9–track tape or CD from Columbia). Jeff Karn ("Zeke") was my "Roomie" for a couple years and helped me write computer codes for work and play (he got the modems to call up the lab paging line and play "Mary Had a Little Lamb). I must also mention the Coffee Shop Gang, Nigel "Niggles" Orr, Daniel "Baby-Face" Bazin, and Mats "Swede" Cronqvist. These guys helped with experiments, analysis, and taught me how to act like a Moody European. Niggles also provided some background material that I used in Chapter One, with his permission. The Swede was instrumental in teaching me the proper way to drink vodka and to sing various drinking songs (including the Swedish National Anthem). Keith McDonald

("Flounder", "Fishman", "Sparty") did a lot of analysis on the calibration data for the S320 experiment when he wasn't busy making targets, going to class, or trying to find an easy way out of doing his homework.

This list of people gets long in a hurry! Let me just say that I appreciate the help I got from the designers, the machinists, the staff scientists, the detector lab people, the electricians, the welders, the electronics personnel, the RF group, the various people with whom I've shared office space, and everyone else at the lab. Last but definitely not least, I'd like to thank the ECR group, the cyclotron operations staff, and everyone from the UP who helped out.

There's a lot more I could acknowledge that I'd rather not have in writing anywhere, so I'll leave those items to the oral historians of the lab. All-in-all I have had a very positive experience at the NSCL and I will always remember my tenure here. Hopefully I'll be able to come back to do work at MSU in the future.

Finally, I want to say something about the two people who brought me into this world — Mom and Dad. They have put up with me for longer than anyone else I know, and deserve some kind of world prize for that. It's got to be tough to respond enthusiastically when your son calls home to tell about the newest frazostat he made to study some fritsosphere. The excited "Oh, that's nice dear..." was really appreciated, even though I knew you folks never understood a word I was saying. Regardless, my accomplishments are your accomplishments. Enjoy!

Contents

List of Tables

List of Figures

Chapter 1

Introduction

I Scientific Background

The first artificially produced unstable isotope was synthesized by Curie and Joliot in 1934[cu34]. Since then, approximately 2000 such nuclei have been created (of the 6000 to 8000 predicted to exist) and studied to provide additional information to that derived from the 263 stable and 60 radioactive isotopes found in nature. The nuclear properties that can be measured include their masses, half-lives, decay modes, spins, moments, sizes, shapes, densities, excited states, and so on. The goal of these studies is to understand the interaction between nucleons well enough that a single physical model can describe the properties of any known nucleus and correctly predict the properties of a nucleus that has yet to be observed. A universal nuclear model would have an immediate application in astrophysics to help understand how various stellar processes occur. One can also imagine applications in designing efficient nuclear reactors and safely disposing of their wastes, or perhaps synthesizing nuclei in higher yields for nuclear medicine and radiotracer studies.

The question arises, how does one approach this goal? Is it necessary to study every particle bound nucleus that every model predicts? Clearly, the existing models must be compared to determine the regions of discrepancy among them. The

properties of the nuclei in such regions then provide a test for the validity of the models.

One of the most basic properties of a nucleus is its mass. The models that predict nuclear masses can be divided into three groups: those based on macroscopic properties of nuclei, those based on microscopic properties of nuclei, and those based on a combination of microscopic and macroscopic properties. One simple formulation of the macroscopic model of Bethe and Weizsäcker[we35,bb36] is shown in equation 1.1. It is referred to as the liquid-drop model, since the stability of a nucleus is expressed in terms of its volume and surface area, as in a drop of water. Additional terms are present to account for the Coulomb repulsion of protons, the instability of extremely neutron-rich or proton-rich nuclei, and the tendency for paired nucleons to provide more stability than unpaired nucleons. The binding energy of a nucleus with mass A, neutron number N, and proton number Z, is then

$$B(N,Z) = -a_V A + a_S A^{2/3} + a_C \frac{Z^2}{A^{1/3}} + a_I \frac{(N-Z)^2}{A} - \delta(A) \qquad (1.1)$$

where a_V is the volume term, a_S is the surface term, a_C is the Coulomb term, a_I is the symmetry term, and $\delta(A)$ is the pairing term. These constant terms are obtained by a fit to known nuclei, and a comparison to experimental results is shown in Figure 1.1[ri80a,ho75].

The microscopic models take a quantum mechanical approach to the nucleus. Nucleons are considered to be independent particles in single-particle orbits. The interaction is two-body and there is a strong spin-orbit term in the nuclear potential which is compatible in strength to the nuclear force. The Schrödinger equation then takes the form:

$$H_0\Psi = \left\{\sum_{i=1}^{A} h_i\right\}\Psi = \sum_{i=1}^{A}\left\{-\frac{\hbar^2}{2m}\nabla_i^2 + V(\vec{r}_i, s_i, t_i, \ldots)\right\}\Psi = E\Psi. \qquad (1.2)$$

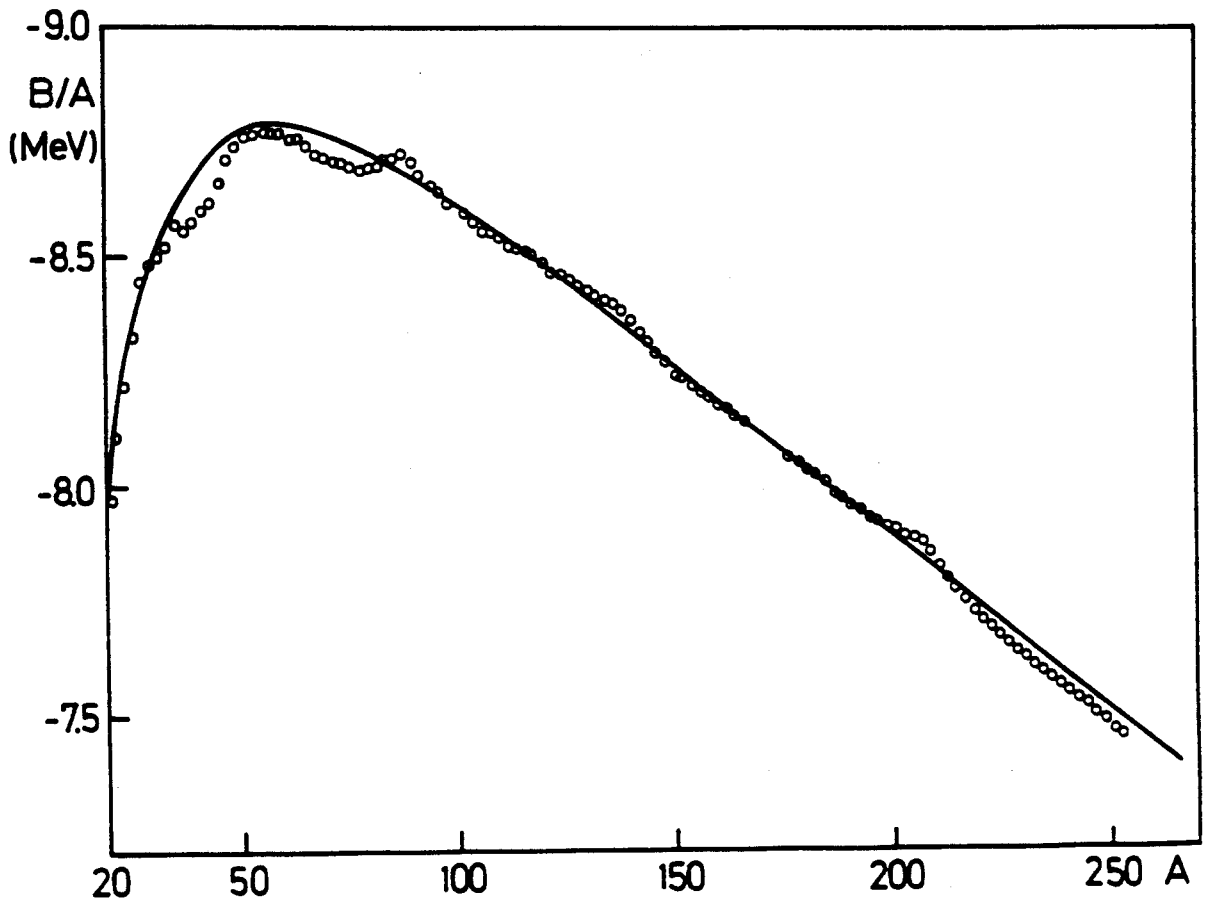

Figure 1.1: Experimental values of B/A for β-stable odd-A nuclei and the calculated values from the Liquid Drop Model [ho75].

The wavefunctions, Ψ, are anti-symmetrized products of single-particle functions that are eigenfunctions of the single-particle Hamiltonian, h_i. The potential, V, is a function of the particle's position, $\vec{r}_i$, spin, s_i, particle type, t_i (1/2 for protons, –1/2 for neutrons), and so on. The energy levels that result from solving the many-body Schrödinger equation are shown schematically in Figure 1.2. One obvious reason the shell model for nucleons is different from that for electrons in an atom is that there are two types of nucleons, differentiated by t_i. Two separate potential wells result, one for $t_i = 1/2$ (protons) and another for $t_i = -1/2$ (neutrons). The Coulomb force must be added to the proton potential as well as a symmetry term as described for the macroscopic model. Particularly stable nuclei, known as "magic" nuclei, exist whenever a nucleus has a full shell of protons, neutrons, or both.

Table 1.1 shows a comparison of ten mass models in terms of the number of parameters and database nuclei used and their ability to predict the masses of known nuclei. All of these models give reasonable values of the nuclear masses near the valley of stability, but they begin to diverge near the nucleon-drip lines. The drip line is the limit where if, for example, another proton is added to a nucleus at the proton-drip line, it simply "drips off" since there is not enough binding energy for the nucleus to exist. The proton and neutron-drip line nuclei are then the most extreme tests possible for these mass models, particularly in regions where the models disagree as to whether a nucleus even exists. For example, in the case of ^{29}Ne[lan85], it was enough to simply produce a few nuclei in a reaction to show that only the microscopic model of Uno and Yamada[uno82] was correct in predicting that the nucleus was bound.

Studies of the excited state structure of nuclei can also determine whether a nucleus exhibits a single-particle (microscopic) or multi-particle (macroscopic) behavior. The microscopic models indicate that magic nuclei should be strongly microscopic, whereas macroscopic properties are more prevalent in nuclei with higher masses. The

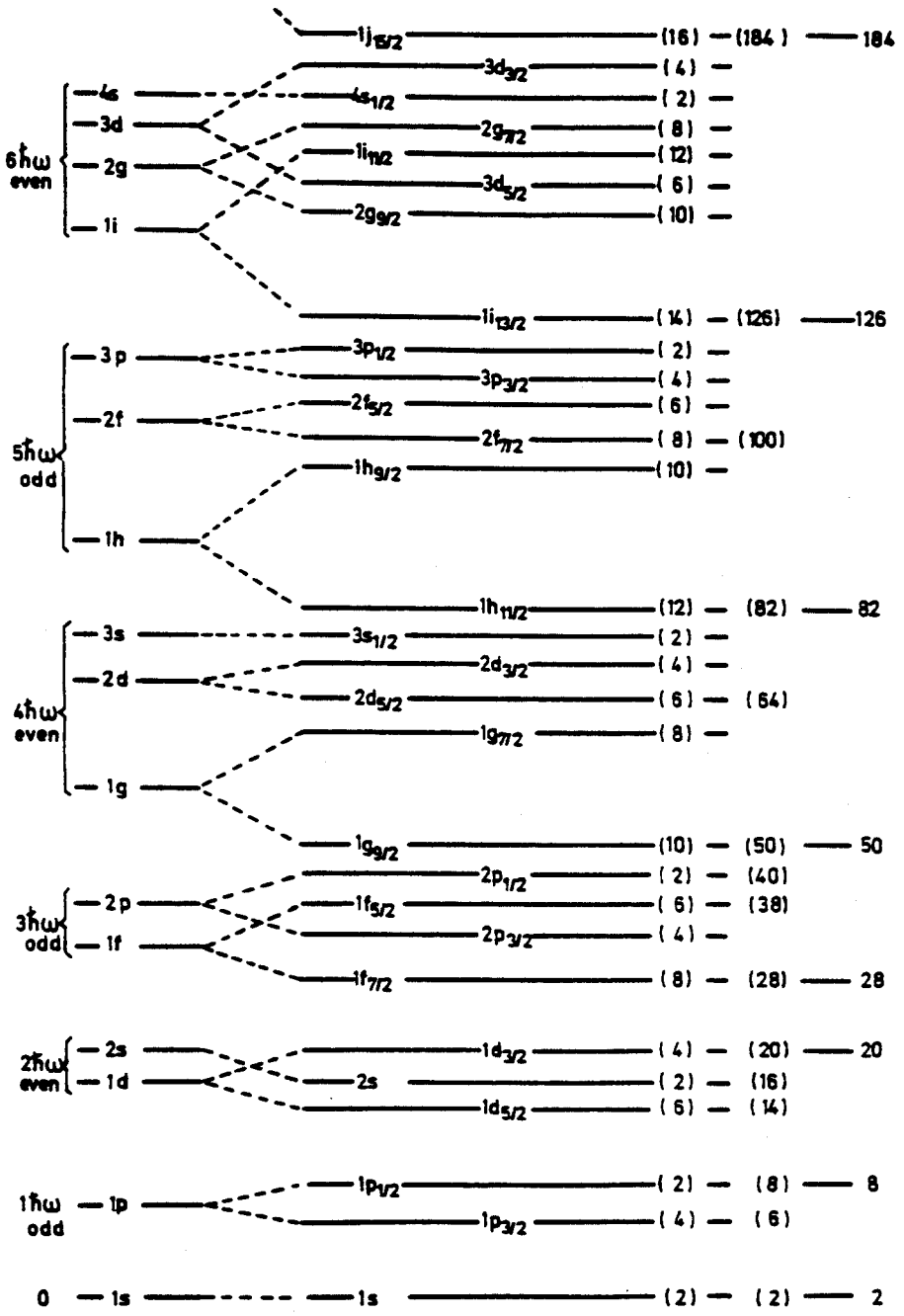

Figure 1.2: Schematic nuclear levels of the Shell Model with spin-orbit term. [ri80b,mj55].

Table 1.1: Comparison of mass models based on microscopic (μ) properties of nuclei, macroscopic (M) properties of nuclei, and a combination of microscopic and macroscopic properties (M,μ)[hass].

Mass Model	Parameters Used	Database Nuclei Used	RMS Deviation (keV)	Average Deviation[a] (keV)	Nuclei[b] Predicted
Pape and Antony (μ)	*c*	85	271	123	381
Dussel, Caurier, and Zuker (μ)	45	1328	287	-13	1984
Möller and Nix (M,μ)	26	1593	849	13	4635
Möller, Myers, Swiatecki, and Treiner (M,μ)	29	1593	777	14	4635
Comay, Kelson, and Zidon (μ)	*d*	1541	431	10	6537
Satpathy and Nayak (M)	238	1593	456	1	3481
Tachibana, Uno, Yamada, and Yamada (M,μ)	281	1657	538	22	7204
Spanier and Johansson (M)	12	652	512	0	4162
Jänecke and Masson (μ)	928	1535	343	16	5860
Masson and Jänecke (μ)	471	1504	346	14	4383

[a] Based on the convention: $Deviation = Calc.Mass - Exp.Mass$.
[b] Includes database nuclei used.
[c] Two parameters to calculate b of isobaric mass equation.
[d] Subsets of the known nuclei.

magic nuclei tend to have higher nucleon separation energies and fewer low-lying excited states, as well as higher energy first electric quadrupole (E2 or 2^+) excited states. Generally, the E2 transition is considered to be a multi-particle property – often described as a surface vibration. Nuclei with particularly low energy E2 transitions are highly deformed compared to the magic nuclei, which are spherical. A general trend (Figure 1.3) is for the first E2 transition to decrease in energy for heavier nuclei, thus indicating an increase in multi-particle behaviour with mass. The figure, however, shows the single-particle nature of the magic nuclei. Thus, for years scientists have been trying to produce exotic magic nuclei like ^{100}Sn to test the models, since such a nucleus is relatively high in mass (A = 100), and doubly magic (N = Z = 50). Nuclei like ^{100}Sn may provide insights into a possible link between the single-particle and multi-particle properties of nuclei.

II EXPERIMENTAL MOTIVATIONS

The region of nuclei chosen for the present study in this dissertation lie along the proton-drip line above mass A = 50. These nuclei are interesting because of their nuclear structure and shapes, their exotic decay properties, and their importance to mass models and astrophysical model predictions. For example, ^{76}Sr and ^{80}Zr are two nuclei with ground state deformations among the largest known to exist[lis90]. However, the abrupt increase in deformation between ^{72}Kr and ^{76}Sr is inconsistent with the present predictions of a smooth increase in deformation among the N = Z nuclei in this region. Further spectroscopic studies are needed, and hence a means of producing these nuclei at high rates is also needed in order to understand this phenomenon.

A number of studies[ro90,hour89,hot88] have attempted to identify the ground state

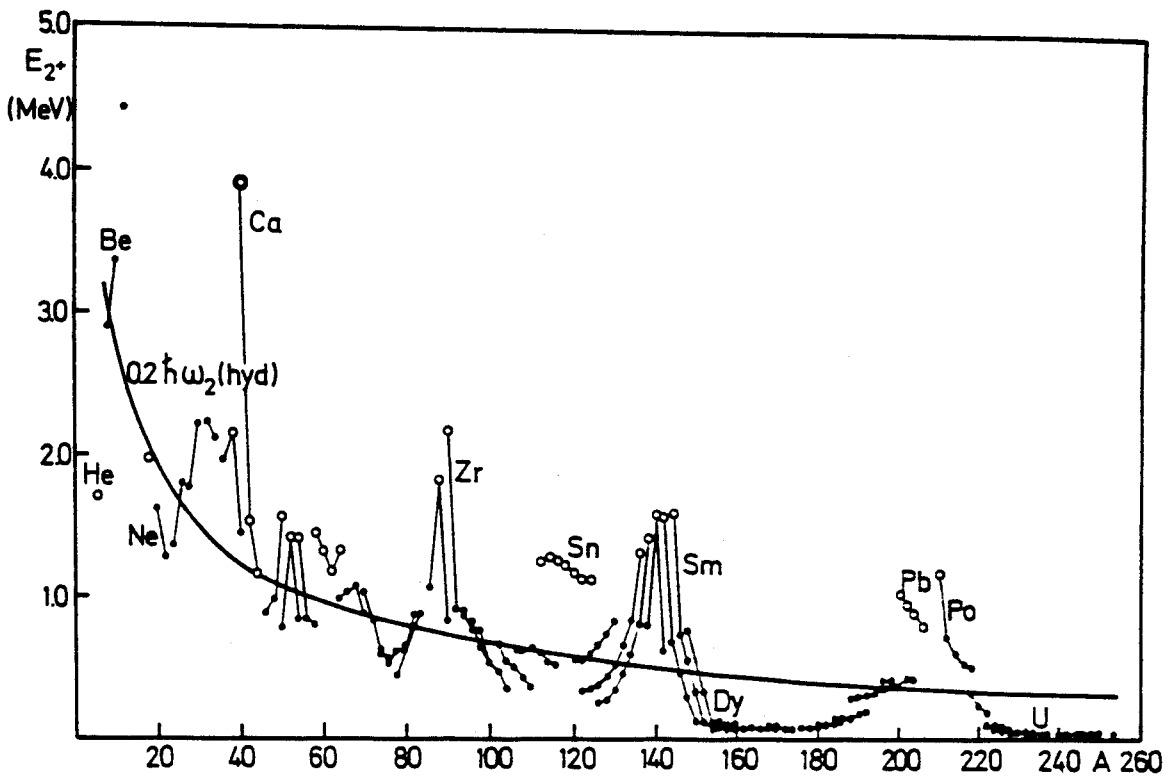

Figure 1.3: Energy of the first 2^+ state in even-even nuclei. Closed shell nuclei are indicated by open circles [ri80c,nn65].

proton decay of ^{65}As and ^{69}Br. However, no evidence for such activity, which has been seen in only four other nuclei: ^{151}Lu[hof82], ^{147}Tm[kl82], ^{113}Cs[fae84], and ^{109}I[fae84], has resulted. In fact, there is no previous evidence that either ^{65}As or ^{69}Br exist, and the mass models disagree as to whether they are bound. In the proton decay studies of ^{65}As and ^{69}Br the absence of decay products that can be assigned to these nuclei can mean that the nuclei do not decay by proton emission, that the nuclei were not produced in the particular reaction, or that the nuclei simply do not exist. Therefore, it is important to design an experiment that will unambiguously identify these nuclei so that subsequent experiments can be planned to study their properties.

Perhaps the most interesting reason for studying nuclei in this region is that their properties must be known to understand certain astrophysical processes. Again, the particle stability of ^{65}As has been of interest in recent years – in this instance with respect to the duration and termination of the rapid-proton capture (rp) process. The rp-process was first postulated by R.K. Wallace and S.E. Woosley[wa81] as a means of nucleosynthesis which involves the capture of protons on nuclei at a rate much higher than the rate at which nuclei can beta decay. The high temperatures (10 keV to 100 keV, or 10^8K to 10^9K) and densities ($\rho \approx 10^3$ to 10^6g/cm^3) required for such hydrogen burning are not found in the interiors of main-sequence stars. However, there are several astrophysical environments where such a process can occur. In particular, much interest has been shown in applying the the rp-process model to accretion neutron stars and the x-ray bursts that are observed[wa81,wa84,ay82,gr76,woo76].

In the Wallace and Woosely formulation of the rp-process, the dominant process of generating energy in the hydrogen-rich sites at such high temperatures is the β-limited carbon-nitrogen-oxygen (CNO) cycle. The CNO cycle reactions can be expressed in short hand notation as:

$$^{14}O(\beta\nu)\ ^{14}N(p,\gamma)\ ^{15}O(\beta\nu)\ ^{15}N(p,\alpha)\ ^{12}C(p,\gamma)\ ^{13}N(p,\gamma)\ ^{14}O$$

or graphically as shown in Figure 1.4. This is a catalytic cycle of nuclear reactions that converts four protons into a helium nucleus plus two positrons and two neutrinos. In the temperature range of the rp-process, leakage from the CNO cycle is initiated via the reaction $^{15}O(\alpha,\gamma)\ ^{19}Ne$ when the concentration of α particles becomes sufficiently high. If the hydrogen density is also sufficiently high, then ^{19}Ne will capture a proton to form ^{20}Na. Once ^{20}Na is formed, the flow continues via proton capture along the proton drip line, bypassing nuclei with long beta life times.

Weakly bound nuclei at the drip line are susceptible to photodisintegration – (γ,p) reactions – if the stellar temperature is comparable to the binding energy of the nucleus. Also, further synthesis to higher masses depends on the occurance of β^+-decay or electron capture at these waiting points before the process can continue. This is analogous to the more common r-process of neutron capture and β^--decay in stellar nucleosynthesis. Unlike the common r-process, however, the rp-process is hindered by an increasing Coulomb barrier for proton and alpha capture as heavier masses and higher nuclear charges are produced.

In the study of flow above A=56, the astrophysical phenomenon of x-ray bursts in neutron accretion stars has been a topic of particular interest[wa81,wa84,ay82,gr76,woo76]. The basic model for these x-ray bursts is that matter is accreted onto the surface of a neutron star from a hydrogen-rich companion in a binary star system. When sufficient hydrogen density ($\rho \approx 10^3$ *to* $10^6 g/cm^3$) is reached on the surface of the neutron star, the rp-process begins and a thermonuclear runaway occurs. The run-away continues for some time period (approximately one minute), until the accreted material is burned and thus results in an x-ray burst of finite length.

The energy generated at late times in x-ray bursts and the occurence of multiple

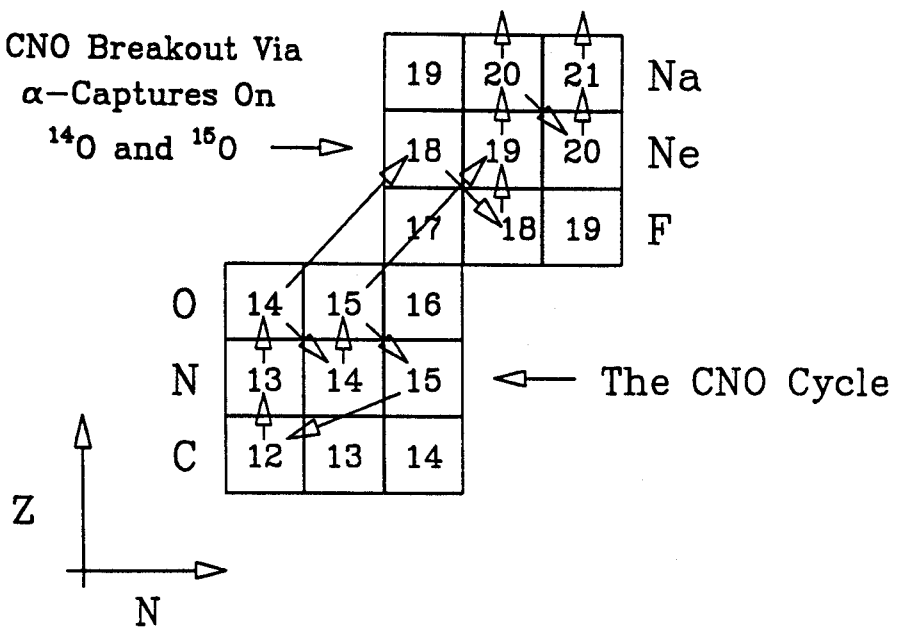

Figure 1.4: The β-limited CNO cycle.

bursts in short time periods may depend critically on the production of isotopes with mass greater than ^{56}Ni (see Figure 1.5). At this point the mass flow and energy generated for A> 56 is completely determined by the reaction ^{56}Ni(p,γ) ^{57}Cu, since the halflife of ^{56}Ni (6.1 days) is much longer than the astrophysical event. If the flow could not continue through ^{57}Cu the process would cease with a buildup of ^{56}Ni. The mass measurement and subsequent structure studies of ^{57}Cu by Sherrill *et al.*[sh85] have lead to new calculations which indicate that sufficient ^{57}Cu is produced in the rp-process to allow the synthesis to continue to higher masses following its β^+-decay. Such a point along the mass flow is called a *bottleneck* since it is the only possible path of flow to higher masses. The next bottleneck occurs at ^{60}Zn, which has a 2.4 minute halflife. The flow rate beyond A=60 will depend on the degree of binding in ^{61}Ga, which has not been previously identified. Since there is little or no data for the proton-rich nuclei in this region, semi-empirical mass models have been used to estimate the binding energies[ha88]. However, because of uncertainties in the models, nuclei that occur at such bottlenecks in the rp-process calculation may be either proton-unbound or so loosely bound that they photo-dissociate at high stellar temperatures.

This point is further illustrated by the bottleneck nucleus ^{65}As, shown in Figure 1.5. It is near the proton-drip line and there is some question as to whether it is proton bound. If ^{65}As is particle-unbound, then in order for the rp-process to produce nuclei larger in A and Z, ^{64}Ge must decay to ^{64}Ga and subsequently capture a proton. However, since the halflife of ^{64}Ge ($\approx$ one minute) is much longer than the time necessary for a proton capture, the mass flow would be impeded in this case. In fact, all of the above reactions come to equilibrium at a time dependent on the halflives, binding energies, proton capture rates, and abundances of the species involved. The overall rate through this bottleneck will then determine the flow to higher masses. A series of differential equations can be used to calculate this flow, given that the rates

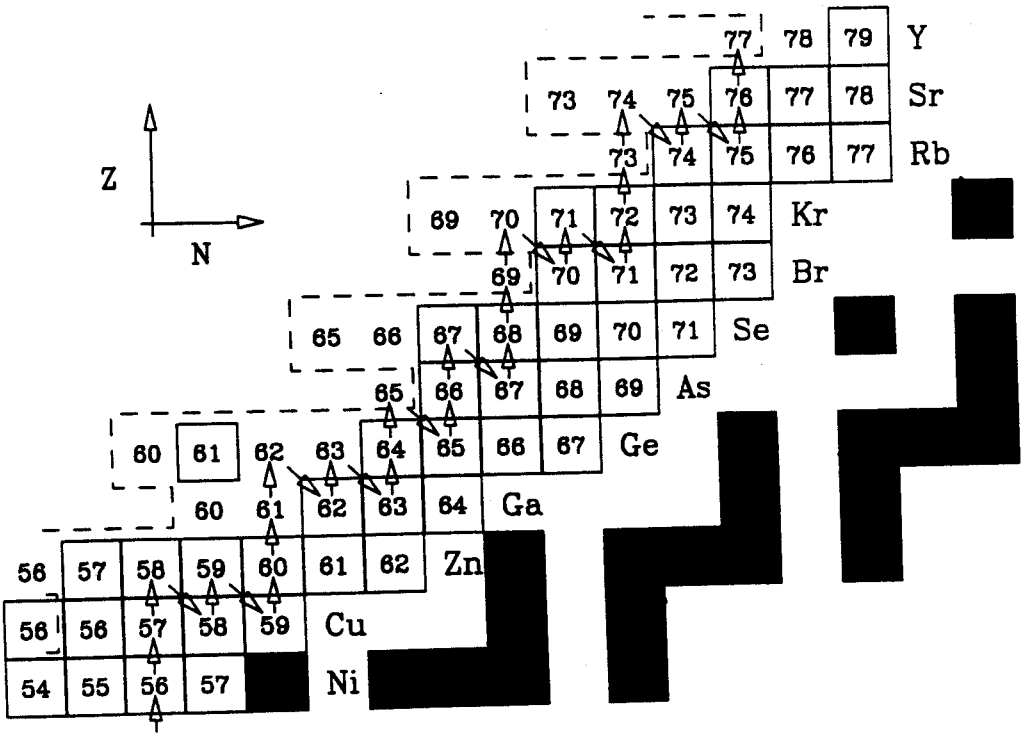

Figure 1.5: Mass flow above A=56 for $\rho = 10^6$ and T = 10^9K [wa81].

for each of the reactions can be determined. This is very similar to having a multi-step chemical reaction, where the resulting products and the rate of the reaction is dependent on the intermediate species formed. For the present case three groups of reactions can be written for the path through ^{64}Ge to ^{66}As and beyond:

$$^{64}\mathrm{Ge} + \mathrm{p} \rightleftharpoons {}^{65}\mathrm{As}\ (\mathrm{Fast})$$
$$^{65}\mathrm{As} + \mathrm{p} \rightleftharpoons {}^{66}\mathrm{Se}\ (\mathrm{Fast})$$
$$^{66}\mathrm{Se} \longrightarrow {}^{66}\mathrm{As} + \beta^{+} + \nu\ (\mathrm{Slow})$$

$$^{65}\mathrm{As} \longrightarrow {}^{65}\mathrm{Ge} + \beta^{+} + \nu\ (\mathrm{Slow})$$
$$^{65}\mathrm{Ge} + \mathrm{p} \rightleftharpoons {}^{66}\mathrm{As}\ (\mathrm{Fast})$$

$$^{64}\mathrm{Ge} \longrightarrow {}^{64}\mathrm{Ga} + \beta^{+} + \nu\ (\mathrm{Slow})$$
$$^{64}\mathrm{Ga} + \mathrm{p} \rightleftharpoons {}^{65}\mathrm{Ge}\ (\mathrm{Fast})$$
$$^{65}\mathrm{Ge} + \mathrm{p} \rightleftharpoons {}^{66}\mathrm{As}\ (\mathrm{Fast})$$

The equilibrium reactions representing the proton capture and photodisintegration are fast steps, and the higher binding energies of the products will increase their abundances. The beta decays occur at a much slower rate, and are thus the rate-determining steps for the flow. If ^{65}As is sufficiently bound and either of the first two groups of reactions dominate, then the mass flow will move relatively quickly through the ^{64}Ge bottleneck, since the halflives of ^{65}As an ^{66}Se are predicted to be on the order of a second or less. However, if the majority of the mass flow must proceed through the third set of reactions, there will be a significant slowing because of the long beta halflife of ^{64}Ge ($\approx$ 1 minute). This time is comparable to the time scale of the rp-process, so the process would simply build up ^{64}Ge. Thus, simply showing ^{65}As to be particle bound has some implications on the extent of the proton burning in the rp-process. Similar critical points exist for the nuclei ^{69}Br and ^{73}Rb.

The calculations used to simulate the rp-process must take into account all possible pathways and depend on accurate nuclear data to calculate the mass flow. From the example illustrated above, it is clear that the properties of individual nuclei can have a large effect on the outcome of such predictions. The results of calculations by Wiescher, *et al.*[wie91,gor91] are shown in Figure 1.6, where the predicted abundances of the mass A = 64 and 65 nuclei are plotted versus time. In the calculation that produced this figure, ^{65}As was assumed to have a binding energy of 165 keV, and ^{66}Se was assumed to be unbound. The mass A = 64 and 65 grow in as ^{60}Zn is consumed, and then reach a maximum and decrease in abundance as they are processed into higher mass nuclei. The ^{65}As abundance is approximately 2 orders of magnitude less than the ^{64}Ge due to the high rate of photodissociation. Then, if ^{66}Se is included in the calculation, as shown in Figure 1.7, the time at which the A = 64 and 65 nuclei are processed into higher mass nuclei is reduced by a factor of ten. These figures emphasize the complexities of such calculations and the importance of having accurate nuclear data as input.

III Production Methods

A wide variety of methods have been developed for the production of nuclei far from stability. The techniques range from low energy, light particle reactions to relativistic heavy ion studies. For example, low kinetic energy reactions (E/A $<$ 10 to 15 MeV) using both light and heavy ions have been employed. Such reactions using light ions provide accurate spectroscopic information and precise mass measurements through Q-value determinations, however the mechanism can only reach nuclei relatively near the valley of β-stability[tho84,dav85]. Light and heavy ion multi-nucleon transfers[wil73,sco74,wod85,fif85,wod86,mo88] (E/A $\approx$ 10 to 500 MeV) produce nuclei somewhat further from stability and populate a wider variety of levels than light ion reac-

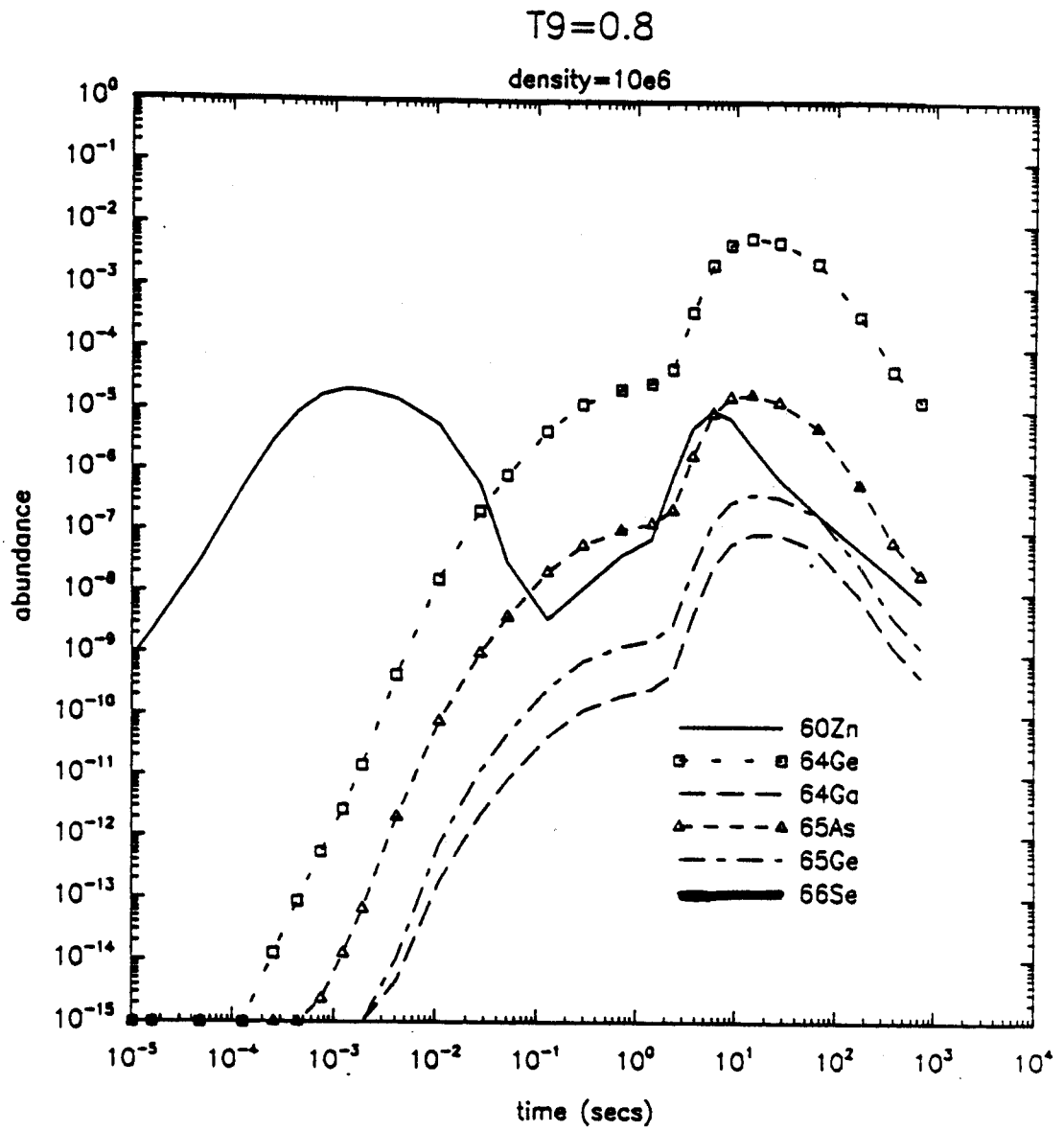

Figure 1.6: Calculation of abundance versus time for A=64,65 nuclei. $\rho = 10^6$, T = 0.8×10^9K, and ^{66}Se is assumed unbound [gor91].

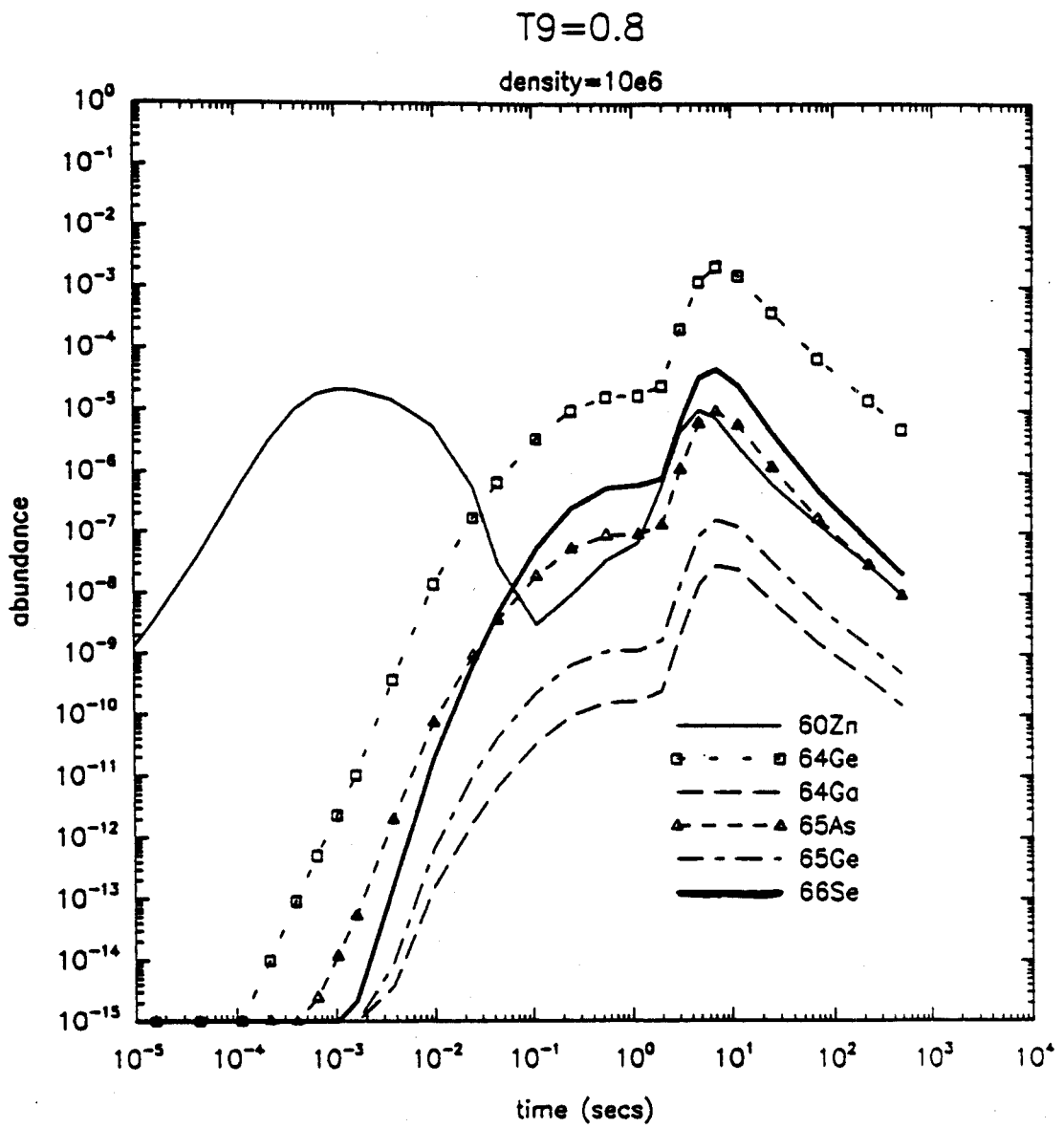

Figure 1.7: Calculation of abundance versus time for A=64,65 nuclei. $\rho = 10^6$, T = 0.8×10^9K, and ^{66}Se is assumed bound [gor91].

tions. However, multi-nucleon transfers result in much lower yields and the reaction mechanism is poorly understood – especially for the transfer of three or more nucleons. Despite the poorer resolution compared to the light ion reactions, reasonably precise mass measurements can still be made with such reactions.

Heavy ion beams have also been used to produce exotic nuclei via the fusion/evaporation reaction mechanism. This method was used extensively to study the β-decay of neutron-rich nuclei during the 1970's[goo74]. The observation of coincident γ-rays following the β-decay of the parent nucleus provides a means to determine the excited state structure of the daughter nucleus and infer the spins and parities of the levels. In addition, if the level scheme of the daughter is known sufficiently well, a beta end point energy measurement can be used to determine the mass of the parent to within 100 – 200 keV. Experiments have also been performed to study evaporation products by detecting coincident protons or alphas particles[pan81]. The technique has been further refined by demanding a three-fold coincidence of two charged particles and a γ-ray from a system formed in a fusion reaction. Nuclei such as ^{64}Ge, ^{65}Ge[gor87], and ^{40}Cl[koz88] have been studied in this manner.

Other methods have been used to produce and study exotic nuclei, such as heavy ion induced fission[des76,rei76] and pion-induced double charge exchange[gil84,set78,nan80]. However, the advent of higher energy heavy ion accelerators has lead to a wealth of new nuclear studies to complement the work done at relativistic proton machines. In the intermediate (E/A $\approx$ 20 to 100 MeV) and high (E/A $>$ 1 GeV) energy regimes, protons, light ions, and heavy ions have been used to produce and then study exotic nuclei. High energy proton and light ion spallation, or target fragmentation, reactions have been performed to produce a variety of neutron-rich nuclei[bow74,sue90]. The isotope separator ISOLDE[des81] at CERN uses this method to produce exotic nuclei. Similarly, the TOFI recoil spectrometer at the LAMPF accelerator at Los

Alamos[vie86] uses this method to measure the masses of light neutron-rich isotopes. The inverse reaction, heavy ion projectile fragmentation, is presently providing a rich source of unknown nuclei. Fragmentation of relativistic heavy ions at Lawrence Berkeley Laboratory has produced a variety of exotic nuclei[wes79]. Using various projectiles at intermediate energies (E/A = 20 to 100 MeV), groups working at GANIL in Caen, France, have obtained relatively high production rates of nuclei up to Z = 27, many of which are at the nucleon-drip lines[lan85,lan86,pou87]. The relatively high rates of production coupled with the LISE[duf86b] and SPEG[bir81] spectrometers provide a powerful tool for measuring masses via time of flight techniques[gil86,gil87], and daughter level schemes from $\beta\gamma$ coincidence spectroscopy[duf86a]. Such experiments have also been performed at MSU to study light neutron-rich isotopes using the Reaction Product Mass Separator[mik88].

IV PRESENT WORK

In the present work, two separate experiments were undertaken in attempts to produce ^{65}As and ^{69}Br. Chapter 2 describes an experiment which employed a low energy fusion/evaporation reaction using a beam from the K500 Cyclotron at MSU. Using this mechanism, the resulting reaction products were separated and identified using the S320 spectrometer and a new focal plane detector specifically designed for this work. Due to time constraints with the construction of the K1200 cyclotron and beamlines there was limited testing of the new detector design. The experiment was carried out none-the-less, but, as will be shown, the nuclei of interest could not be unambiguously identified. However, a viable analysis technique will be demonstrated, as well as a better understanding of the detector design so that the experiment could be performed successfully. But rather than reconstructing the detector and performing the experiment again, a second approach was used to produce the nuclei of interest.

In chapter 3, the projectile fragmentation reaction experiment is described. As noted in the previous section, various research groups have been very successful at producing exotic nuclei nuclei using this high energy reaction, along with magnetic spectrometers to identify the reaction products. Such experiments were made possible for the first time at MSU by the combination of a high energy, heavy ion beam from the new K1200 cyclotron and the newly-commissioned A1200 beam analysis device. The results from this work were quite exciting, and future experiments to measure the halflives and decay modes of the newly identified nuclei should be possible.

Chapter 4 presents a summary of the results, as well as some speculation regarding future work.

Chapter 2

Isotope Production Using the Fusion/Evaporation Reaction

I INTRODUCTION

The fusion/evaporation reaction mechanism[pu77] is a well known method to produce and study unstable nuclei. In this mechanism, the compound nucleus is formed in statistical equilibrium with some excitation energy. The nucleus then decays by the emission of protons, neutrons, α-particles, and γ-rays with probabilities that can be predicted by the Hauser-Feshbach statistical theory[ha52]. The probability of decay to some specific final evaporation product is determined primarily by the statistical weights of the intermediate states of each product along the decay path. Various computer codes, such as CASCADE[pu77], PACE[gav80], and ALICE[pla78], use this model to predict the evaporation products from a given compound nucleus.

When proton-rich nuclei such as ^{65}As and ^{69}Br were identified as important to study, several groups tried to use the fusion/evaporation reaction to produce them. The model calculations indicated that these unusual nuclei could be produced at a level of only one part in 10^4 to 10^5 of the total reaction cross section. The evaporation products would also be produced at very low kinetic energies, making it difficult to identify the elements of interest by their characteristic energy losses and total energies.

Even the use of a spectrometer to separate the reaction products would be difficult, since the cross sections for these nuclei would also be spread over a wide distribution of ionic charge states. Therefore several groups carefully designed experiments to look for unusual decay characteristics of the nuclei of interest. Since ^{65}As and ^{69}Br are predicted to decay by ground state proton emission[ha88], it was thought that these residues could be uniquely identifiable among the other evaporation products.

Hotchkis, *et al.*[hot88], used the Daresbury Recoil mass separator (DRMS) to select the interesting masses from the evaporation products. Products from the reactions ^{28}Si(^{40}Ca,p2n)^{65}As at 140 MeV and ^{40}Ca(^{32}S,p2n)^{69}Br at 125 MeV were separated by mass and implanted in a silicon detector at the focal plane of the DRMS. The primary beam was pulsed so that any proton decay could be detected after implantation without beam background. The decay energies of the protons could be measured, as well as the time of the decay relative to the implantation time. However, in the experiment no proton decays were found that could be attributed to ^{65}As or ^{69}Br. The experimenters concluded that it is possible these nuclei decay mostly by positron emission, or that their halflives are shorter than the minimum five microsecond measurement time of the experiment.

Another group, Hourani, *et al.*[hour89], used the same reactions to attempt a similar experiment at the Orsay Tandem accelerator. They used the superconducting solenoidal coil Soleno[sch84] to collect and focus the evaporation products onto a gas-filled detector. The detector was designed so that the entering ions would be stopped in the gas volume and subsequent proton decays could be detected. Again, the beam was pulsed to allow time to observe the proton decays. This experiment was designed for protons from 250 – 600 keV with decay times from 10 μs to 100 ms. As in the Hotchkis work, no proton decays could be attributed to either ^{65}As or ^{69}Br.

Robertson, *et al.*[ro90], at the Lawrence Berkeley Laboratory 88 inch cyclotron,

tried a slightly different experimental approach. They mounted catcher foils on a rotating wheel behind the target and directly collected the recoil nuclei. The recoils were collected for some time, the beam was pulsed off, and then the wheel was rotated to position the foil in front of a detector telescope to detect any emitted protons. The telescope consisted of a gas-filled δE detector followed by a 300 micron thick silicon detector. The combination of the δE signal from the gas detector and the E signal from the silicon detector gave separation between the protons and betas from the residue nuclei. This system was designed to identify protons from 200 keV to 5.5 MeV, and measure decay times longer than 100 μs. Once again, no proton decays could be assigned to either ^{65}As or ^{69}Br.

The work presented in this chapter represents yet another approach to the observation of ^{65}As and ^{69}Br. This study addresses the more fundamental question of whether or not these nuclei can be produced in the first place. Instead of attempting to identify a decay product, a magnetic spectrometer was used to identify the nuclei produced in the fusion/evaporation reaction directly and to measure their zero-degree momentum distributions. Then, an experiment could be designed to study the decay properties and halflives knowing for certain that the ions of interest were being produced in the reaction. Also, the isotope identification results and the zero degree momentum distributions could be compared to the various fusion/evaporation models to test their predictive power for the drip line nuclei.

The reaction was chosen based on the predictions of the codes CASCADE and ALICE. A primary consideration was that the products must have enough kinetic energy to be detectable in the focal plane detectors of the spectrometer. The design of the detectors was such that ions in the region of interest with energies of E/A = 1.2 MeV or greater could be detected and resolved. Other considerations were the availability of beams from the K500 cyclotron and reasonable target materials. On

Table 2.1: Predicted cross sections from CASCADE for the ions of interest. The beam energy was E/A = 7.8 MeV, and the default level density parameters were used in the calculation.

Nucleus	Predicted Cross Section (μbarns)
^{76}Sr	47.2
^{69}Br	1.55
^{65}As	13.2
^{63}Ge	75.6
^{62}Ge	0.86
^{61}Ga	53.6

the basis of availability alone, the only target and beam combination that showed some production of ^{65}As in the calculations was an ^{36}Ar beam with a ^{40}Ca target. The calculations showed that the the ^{36}Ar beam energy would have to be in the range of E/A = 6.0 MeV to E/A = 8.5 MeV to produce a reasonable rate of ^{65}As with the kinetic energy constraints of the detector. Because of operational considerations of the cyclotron, the beam energy of E/A=8.0 MeV was chosen. A simple calculation shows that this gives evaporation products with energies centered around E/A = 1.8 MeV :

$$\left(\frac{E}{A}\right)_{\text{PRODUCTS}} = \frac{E_{\text{PRODUCTS}}}{A_{\text{BEAM}} + A_{\text{TARGET}}} = \left(\frac{E}{A}\right)_{\text{BEAM}} \left(\frac{A_{\text{BEAM}}}{(A_{\text{BEAM}} + A_{\text{TARGET}})}\right)^2 \quad (2.1)$$

where E represents kinetic energy and A is the mass number. Thus, the minimum energy requirement for the detector is met. The results of the CASCADE calculations are given in Table 2.1.

There were many experimental difficulties encountered in choosing to proceed with this type of experiment. Also, some extraneous time constraints due to the construction of the K1200 cyclotron limited the amount of detector testing and development that could be performed. The results of these measurements are unfortunately lim-

ited. However, the following results will show that such an experiment can be designed to identify the evaporation products directly. They will also show that a viable analysis technique has been demonstrated which can be used to identify exotic nuclei and enable more detailed studies of the fusion/evaporation reaction mechanism.

II Device and Detector Developments

The instrument chosen for this study was the S320 spectrometer[win90] at the National Superconducting Cyclotron Laboratory, Michigan State University. This device could be adapted to completely identify the reaction products from their mass-to-charge ratios as well as their time-of-flight, energy loss, and total energy. It is a medium acceptance, medium resolution device consisting of a quadrupole doublet, dipole, sextupole, and octupole magnets. The spectrometer enables the measurement of momentum distributions as well as the identification of the reaction products so that reaction mechanisms can be studied in detail.

In order to utilize the S320 in this work, modifications had to be made to its alignment, control system, vacuum system, and focal plane detection system. While some of the improvements were made with this specific experiment in mind, many of the modifications were made to improve the overall operation of the device, making it more reliable and easier to use.

A The S320 and its Controls

A test run had shown some alignment problems in the spectrometer, and after sighting with a transit back to a reference point in the beamline, it was found that the target ladder was out of alignment by two millimeters to the right of center (facing towards the focal plane). Since the target ladder's lateral motion is fixed in the target chamber,

Table 2.2: Calibration constants to convert $B\rho/\rho_0$ into amps based on the elastic scattering of E/A = 8 MeV ^{36}Ar from a thin gold target (the dipole field is measured directly).

Magnet	Constant $\{Amps = Constant \cdot \frac{B\rho}{\rho_0}(Tesla)\}$
Quadrupole # 1	147.94
Quadrupole # 2	124.16
Octupole	48.55
Sextupole	54.14

a new viewing scintillator was marked with the true alignment for a focus at the target position.

With the compensated alignment and the installation of new magnet power supplies, a short test run was performed to determine the best settings of the quadrupole doublet, dipole, sextupole, the octupole magnet supplies. The test was carried out by elastically scattering an E/A=8 MeV ^{36}Ar beam, and the results were incorporated into the code used to predict spectrometer settings[win90]. The resulting scaling parameters for the magnetic elements are shown in Table 2.2.

A practical test of the S320 control system was made during a second test run for the fusion/ evaporation experiment. The magnet power supplies were controlled and monitored not only at the control console in the cyclotron control room, but in the data taking area as well. This was made possible using a program written by Ron Fox called PARAM101[fox] that was run on the control system μVAX computer. The program reads the control parameters over a computer interface to the control system and displays them on a terminal screen. The control parameters may also be sent to a printer using this new program.

The vacuum system modifications were minor, however they were important for

running the system with thin targets and fragile detector windows. Throttle valves were added to the target chamber and detector box roughing pump lines so these can be pumped out gradually to avoid damage to thin targets or detector windows. The valves are manually operated near viewing windows so that sensitive targets and detectors can be monitored during this process. A second modification was made to the roughing pump line to enable it to be vented after the roughing pump is shut off. This prevents pump oil from backstreaming into the spectrometer and contaminating targets or reducing the efficiency of the cryopumps. This vent valve is interlocked via the control system to protect the targets and detectors from being damaged by accidental venting.

B THE S320 FOCAL PLANE DETECTORS

The proposed project placed some important experimental constraints on the focal plane detector system. Unit Z resolution in the region of $20 \leq Z \leq 40$ and unit charge resolution up to q=35 were required, thus a detector with a wide dynamical range and with an energy resolution of two to three percent was needed. Position resolution at the focal plane of better than one millimeter full width at half maximum (FWHM) was necessary in order to obtain a one-part in 600 momentum resolution. The time-of-flight (TOF) had to be measured to better than 0.8 nanoseconds FWHM in order to obtain a one-part in 600 velocity resolution. Also, since the flight times were long compared to the cyclotron RF period, a start detector was needed at the acceptance aperture of the spectrometer and a stop detector at the focal plane in order to have an unambiguous TOF measurement. All of these requirements were combined to give the overall resolution necessary to identify the element number, mass, and charge of each ion, and would provide information regarding the reaction mechanism producing these ions. However, the low kinetic energies of the evaporation products—

E/A<2 MeV — required that all detector window thicknesses be minimized in order to reduce energy-loss straggling and multiple scattering. Obviously, this has an impact on the detector response requirements — straggling will effect the energy resolution, multiple scattering will effect the spectrometer resolution. The need for a start detector must be balanced against the extra material it will place in the particle's path.

Initial detector tests were made with the standard focal plane system (Figure 2.1) that consists of two position sensitive wire counters, two proportional ion chambers with wire anodes, and a plastic scintillator. The gas detectors were housed in a common volume of isobutane gas. E/A=10 MeV ^{40}Ar was both elastically scattered from a gold target to check the position resolution, and interacted with a titanium target to produce fusion/evaporation products. A strong position dependence of the proportional ion chamber signals illustrated in Figure 2.2 prevented resolution of the Z's. This position dependence of the proportional signal appeared to result from a physical interaction of the ion-induced electron avalanche with the anode wires, since there was an enhancement of the ion chamber signal pulse height at those positions in the counter where the elastic scattering peaks had been previously focussed. It was thought, since the wires were being operated with voltages slightly into the proportional region, that the locations where the elastic scattering peaks were focused may have been polished by the electron avalanche; that is, the avalanche removed a deposit on the wires that may have been laid by gas polymerization. Visual examination of the wire chambers after the test run showed no clear evidence of wear, but the position dependence was experimentally reproducible. If the focal plane was evenly illuminated with a high intensity of particles, the gas gain would come to a constant value without any positional dependence. But after a few minutes of normal operation, the response would slowly return to that with enhancements in the regions

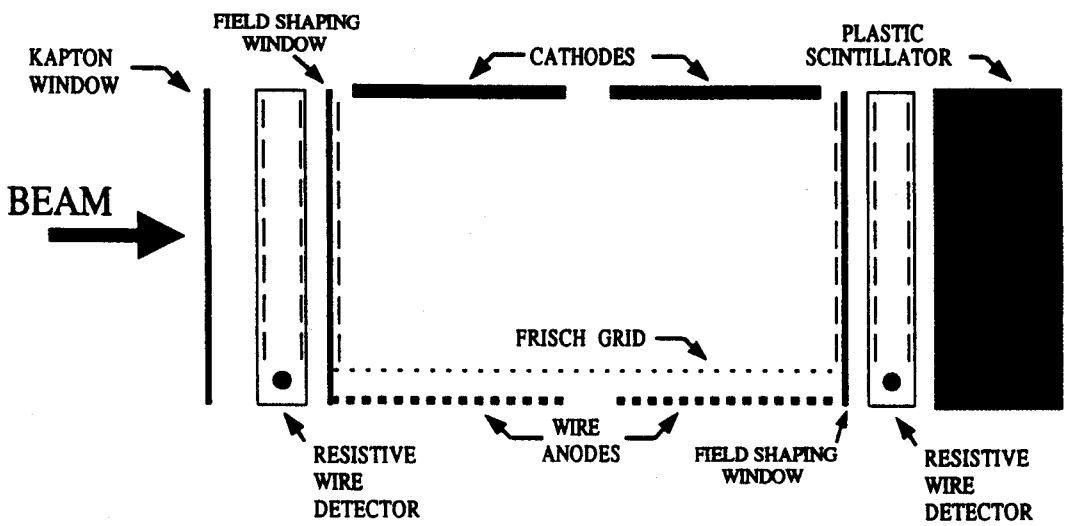

Figure 2.1: Standard S320 focal plane detector.

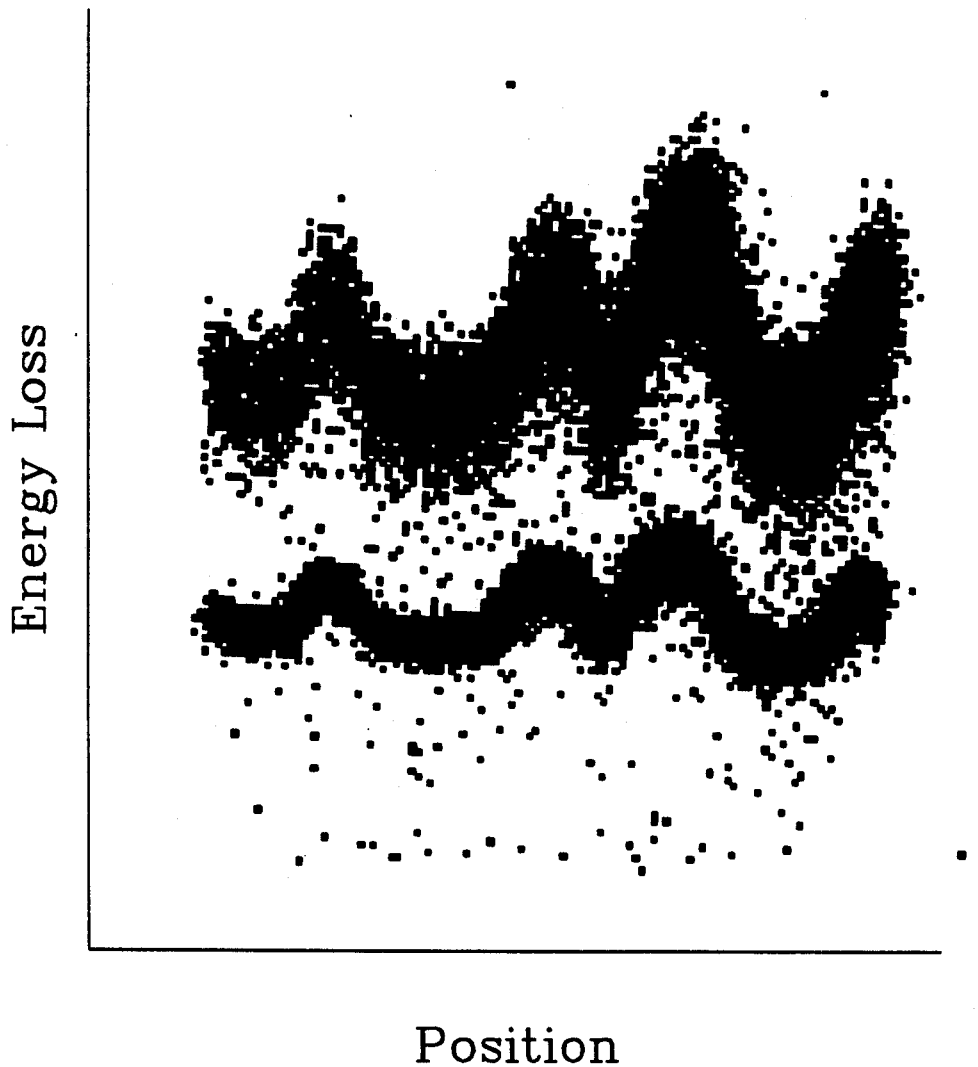

Figure 2.2: Energy loss versus position in the standard S320 detector.

where the elastic scattering peaks had been. It was decided that further tests with different detector gasses would also be beneficial. This positional dependence problem is discussed further in the Results section of this chapter.

After this test run, a new system for detecting the evaporation products was designed based on the idea that better Z resolution would be possible if the ions were stopped in a highly segmented ion chamber. That way, maximum amount of energy loss (ΔE) information could be combined with the total energy (E) information to properly resolve the Z's and to minimize the effects of ΔE straggling. To further improve the Z resolution, two position measurements were necessary so that corrections could be made for the path of the incident particle. A prototype ion chamber was built (Figure 2.3) and tested with an E/A=10 MeV ^{86}Kr beam. The spectrometer was set to accept elastic scattering and single nucleon transfer products. The front proportional ion chamber of the detector used in the previous test run was divided into two sections, with anode plates instead of wires to collect the charge. The back proportional ion chamber retained the usual wire anode. A new "windowless wire" resistive wire proportional counter was tested between the first and second anode plates. This device measured particle position by simple charge division (Figure 2.4). The wire was contained in a grounded box so that the neighboring anode plates would be shielded from its higher electric field. This maintained uniform charge collection throughout the ion chamber. In order to check for field distortions due to the windowless wire detector, the signals from the neighboring ion chambers were observed with the position detector biased and unbiased. No distortions or differences in the ion chamber signals could be observed with an oscilloscope or in the pulse height spectra, indicating that the resistive wires were sufficiently shielded and did not need additional field shaping windows. The position resolution of the windowless wire detector was 0.8mm FWHM.

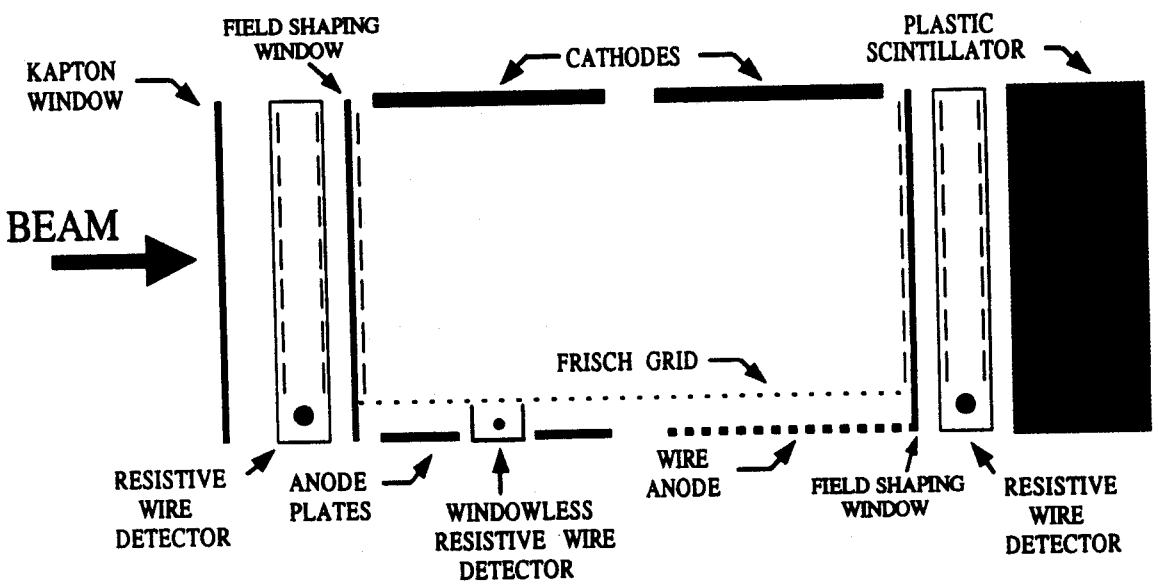

Figure 2.3: Prototype ion chamber detector for the S320 focal plane.

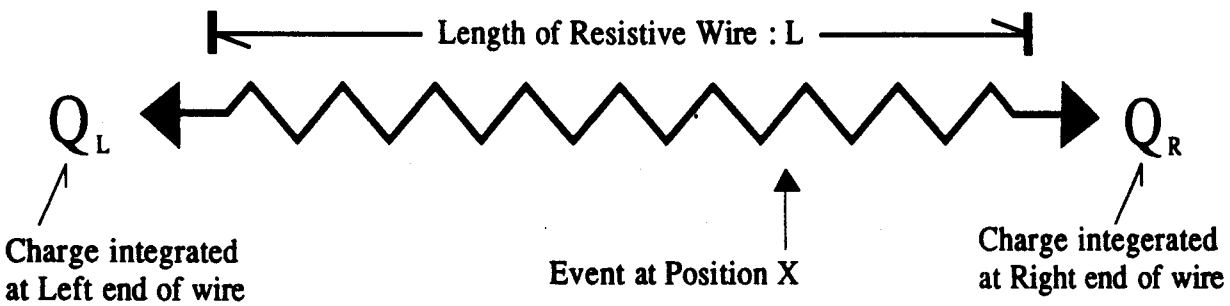

$$X = L \bullet \left(\frac{Q_L}{Q_L + Q_R} \right)$$

Figure 2.4: Illustration of simple charge division.

The prototype detector was created to test the different ion chamber anodes and field shaping using various gasses and various voltage settings. Two gasses were tested: pure isobutane and a mixture of 20% isobutane and 80% freon-14. The freon/isobutane mixture worked well and showed no sign of causing position dependences in the detector. Various tests have been done with this and other gasses at TRIUMF[ope89] showed its superior aging characteristics and highly reproducible results. The freon/isobutane mixture also has a faster recovery time from event to event, thus allowing for higher rates of ions entering the detector. Although the mixture does not have the high gas gain of pure isobutane, it still appeared from this test run that it would give an adequate signal for the slow heavy ions. The detector was able to resolve Z=36, 37, and 38 from the nucleon transfer reactions of krypton on carbon (Figure 2.5).

With the encouraging results from the anode plates and the windowless position wire, the final design for the slow heavy ion detection system was developed. Use of the freon/isobutane gas mixture required further noise reduction in the anode signals. A separated FET preamp was developed (Figure 2.6), in which the first stage amplification is mounted directly onto the anode board. This minimizes the effect of the pickup noise on the cable between the anode and the preamp, and improved the signal-to-noise ratio.

The new ion chamber was divided into twelve one-inch segments – ten for anode strips, and two for windowless position wires. The modular components could be replaced or reconfigured as necessary. The position wires could be used not only to calculate the ion angle, but they could also eliminate any ions that scatter out of the detector volume.

Since the ions are to be stopped in the ion chamber volume, the first part of the detection system has to give both time of flight and position information. A

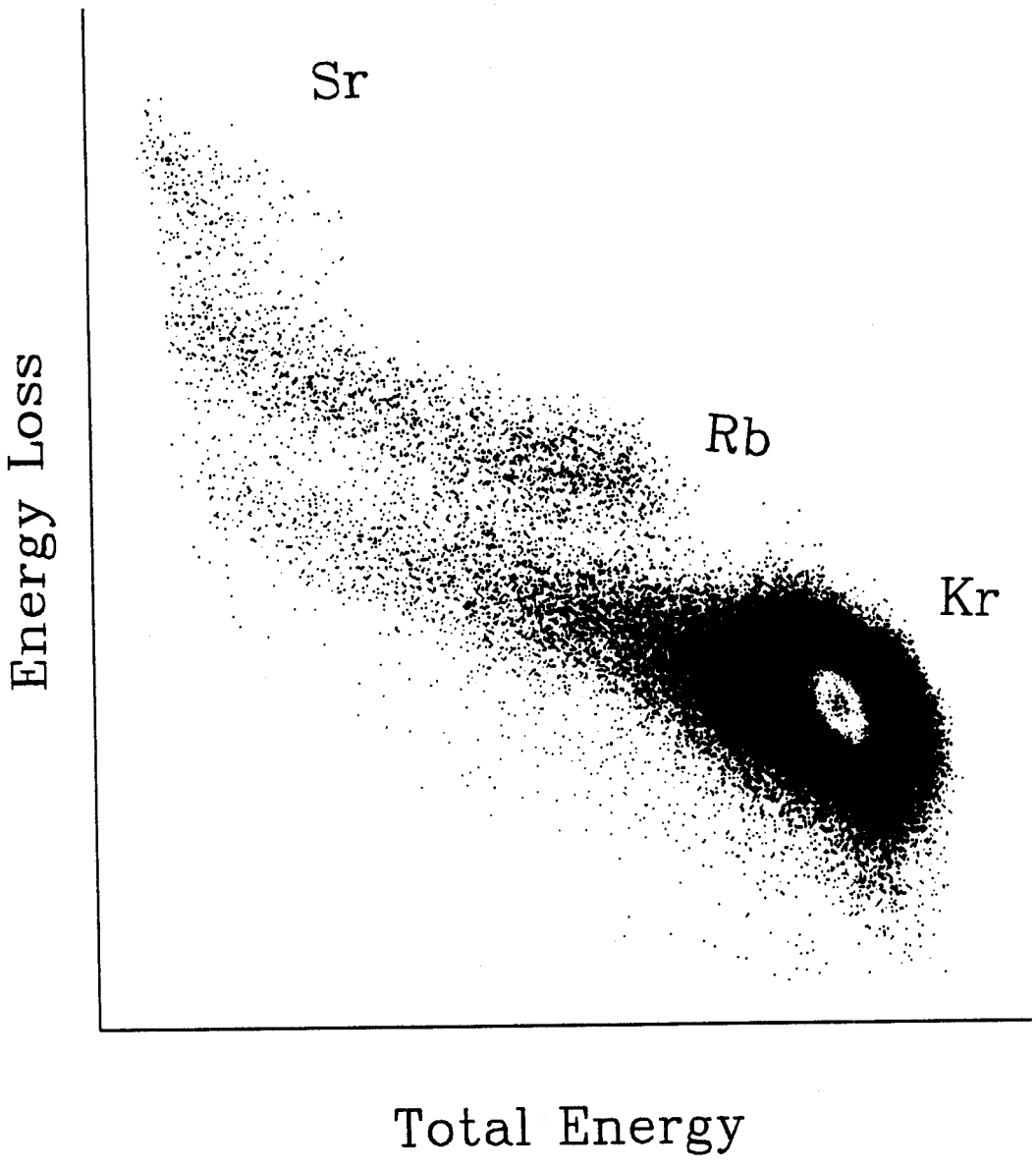

Figure 2.5: ΔE versus total energy for E/A = 10 MeV ^{86}Kr on carbon.

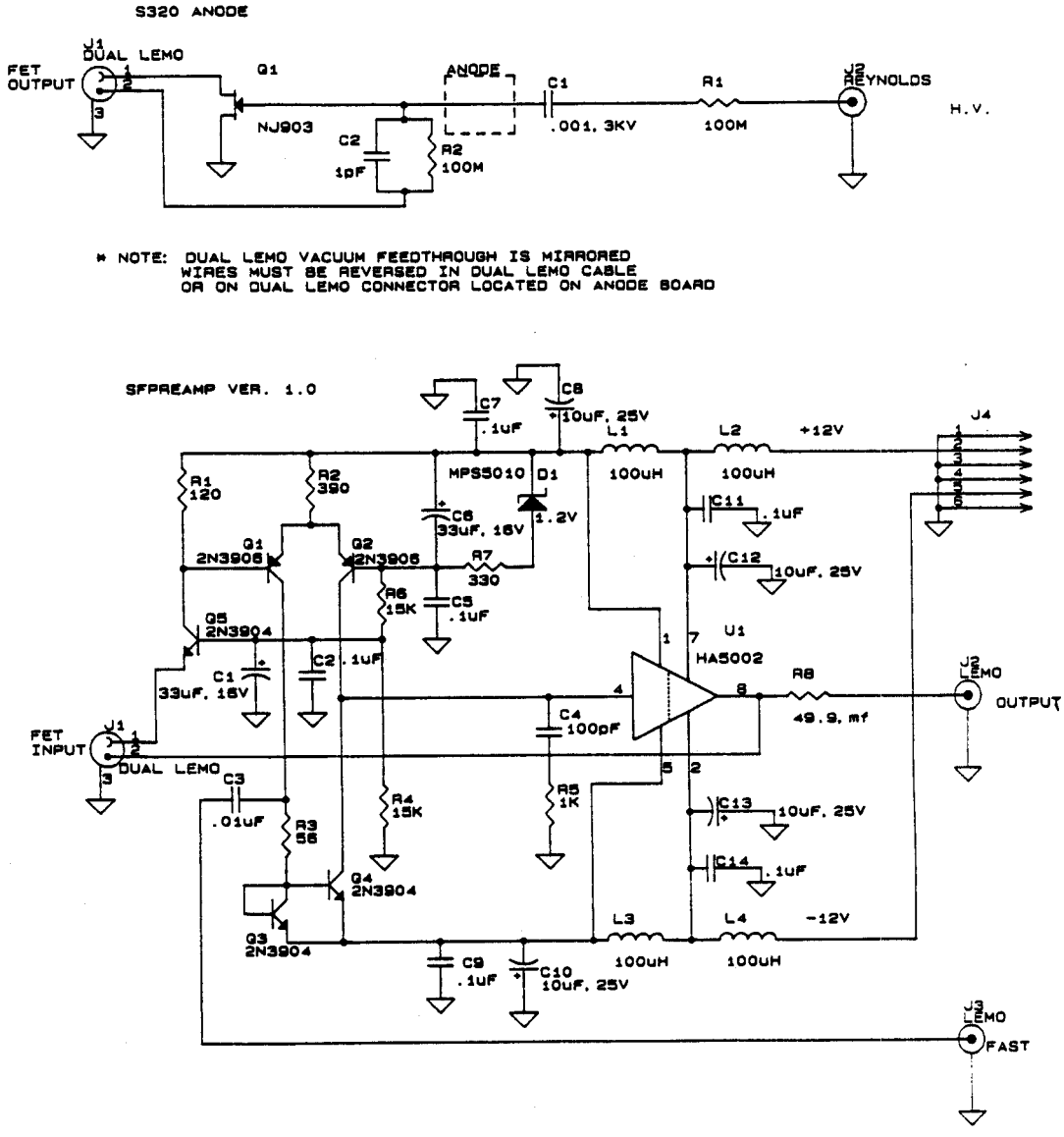

Figure 2.6: Separated FET preamp developed by the NSCL Nuclear Electronics Group.

Low-Pressure Multi-Wire Proportional Counter (LP-MWPC) was designed and built, based on the design of Breskin *et al.*[br77] Such a detector has excellent time resolution and a position resolution well within the requirements of the experiment. The timing signal comes from the anode, and the position signal comes from a delay line readout of the induced charge on two interleaved layers of cathode strips. The time delayed signal taken from either side of the detector (timed against the prompt anode signal) directly corresponds to the position of the ion in the detector. The interleaved cathode strips improve the position resolution.

A diagram of the focal plane detection system is shown in Figure 2.7. The back scintillator was kept at the exit to allow a broader dynamic range and to reject penetrating light ions.

As noted earlier, a start detector is necessary in order to obtain a time of flight resolution of less than 800 picoseconds. The start detector was a thin-foil scintillator[nor87] attached to a photomultiplier tube (Figure 2.8). The foil used during the experiment was $35\mu g/cm^2$ of Bicron BC400 plastic scintillator. The scintillator was made by dissolving 8 grams of the plastic scintillator in 90 ml of mixed xylenes. Twelve drops of this solution were applied to a round glass plate treated with a dilute solution of the wetting agent Tepol and mounted on a motorized turntable. A second glass plate was used to spread the solution evenly over the first plate, and the turntable was turned on. The plate was spun until the xylenes evaporated leaving only a thin uniform layer of scintillator on the glass plate. The foil was separated from the plate by floating it off in water. The foil was lifted from the surface of the water onto a UVT (ultra-violet transmissive) plastic frame that was subsequently glued to the face of a photomultiplier tube. The idea was to have sufficient energy lost in the detector (about four or five MeV) to provide an adequate start signal, and yet keep the detector thin enough so that it did not significantly degrade the energy or momentum

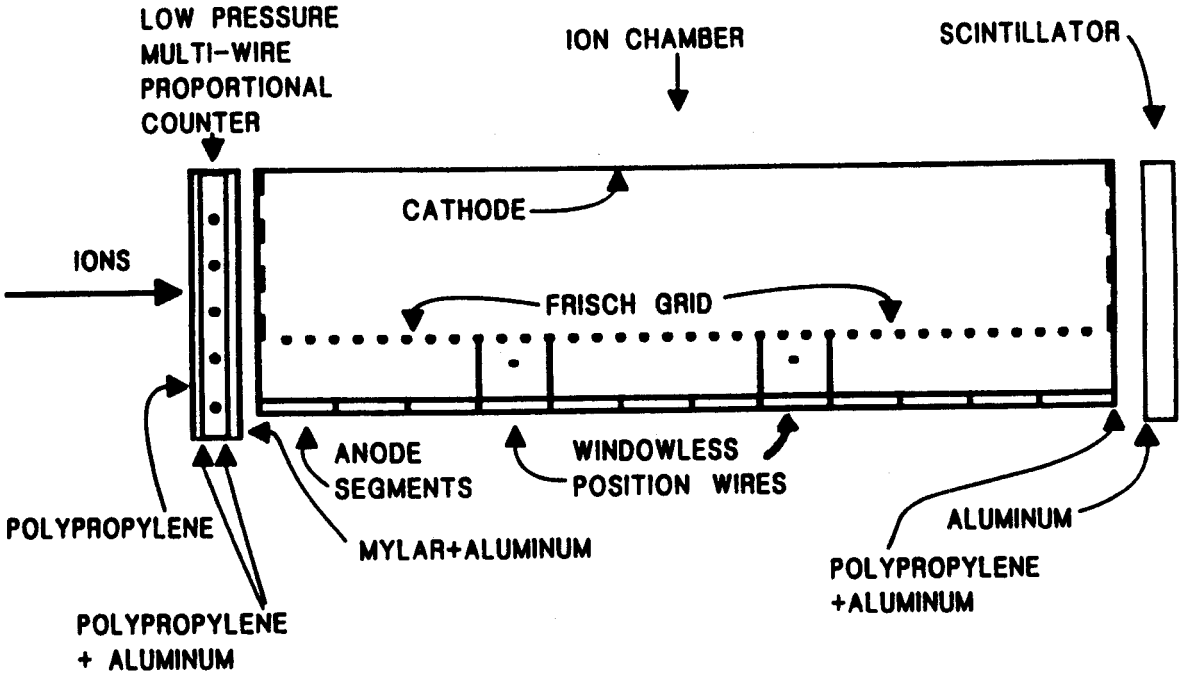

Figure 2.7: Diagram of the final detector design for the S320 focal plane.

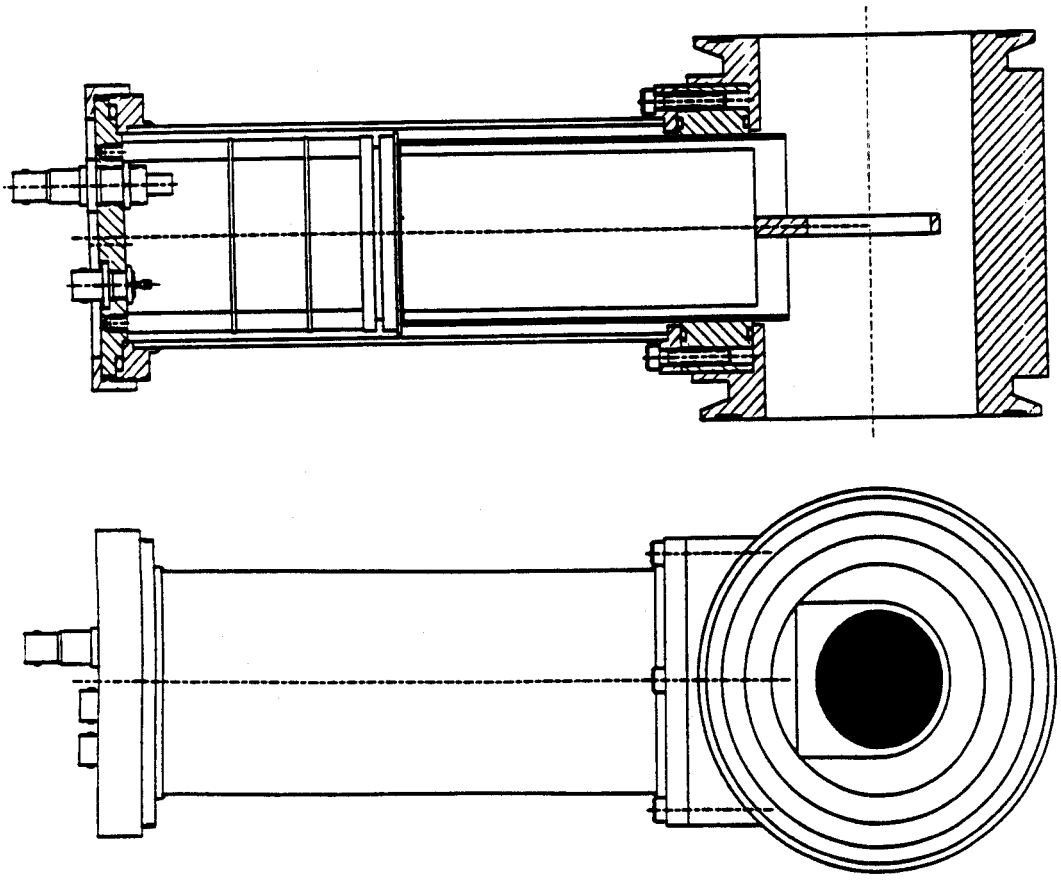

Figure 2.8: Start detector design.

resolution of the spectrometer.

C Background Rate Reduction: Permanent Dipole Magnets

It was also important, since the 0° momentum distribution was to be measured, to physically separate the beam and the elastically scattered ions at small angles from the fusion/evaporation reaction products before the start detector. A similar problem occurred for an experiment proposed for the MSU Reaction Product Mass Separator (RPMS)[cur86]. In that case, a small permanent magnet dipole was fitted into the beampipe directly behind the target providing separation before the acceptance aperture of the RPMS Wien filter. This idea was extended to the S320 by designing a samarium-cobalt (Sm-Co) permanent magnet dipole to be placed immediately after the target position. Since the fusion reaction products from ^{36}Ar on ^{40}Ca would have approximately one-half the rigidity of the primary beam, such a magnet could produce an angular separation between the evaporation products and beam velocity ions in the wedge-shaped vacuum chamber following the target chamber. Then, with the spectrometer set at some angle in the lab, the 0° evaporation products would be accepted by the spectrometer while the beam and small angle elastics would be collected in the Faraday cup in the wedge chamber. This case is illustrated in Figure 2.9.

The following small angle approximation can be used to calculate the bending angle for a dipole magnet design:

$$\theta_{\text{BENDING}} \approx \frac{\int B \cdot d\ell}{B\rho} \approx \frac{\sum B \cdot \Delta\ell}{B\rho} \tag{2.2}$$

where θ_{BENDING} is the ion's bending angle in radians, $B\rho$ is the rigidity of the particle, and B is the field in the dipole at a given point $\Delta\ell$ along the path of the particle. The assumptions here are that the velocity vector of a particle is perpendicular to

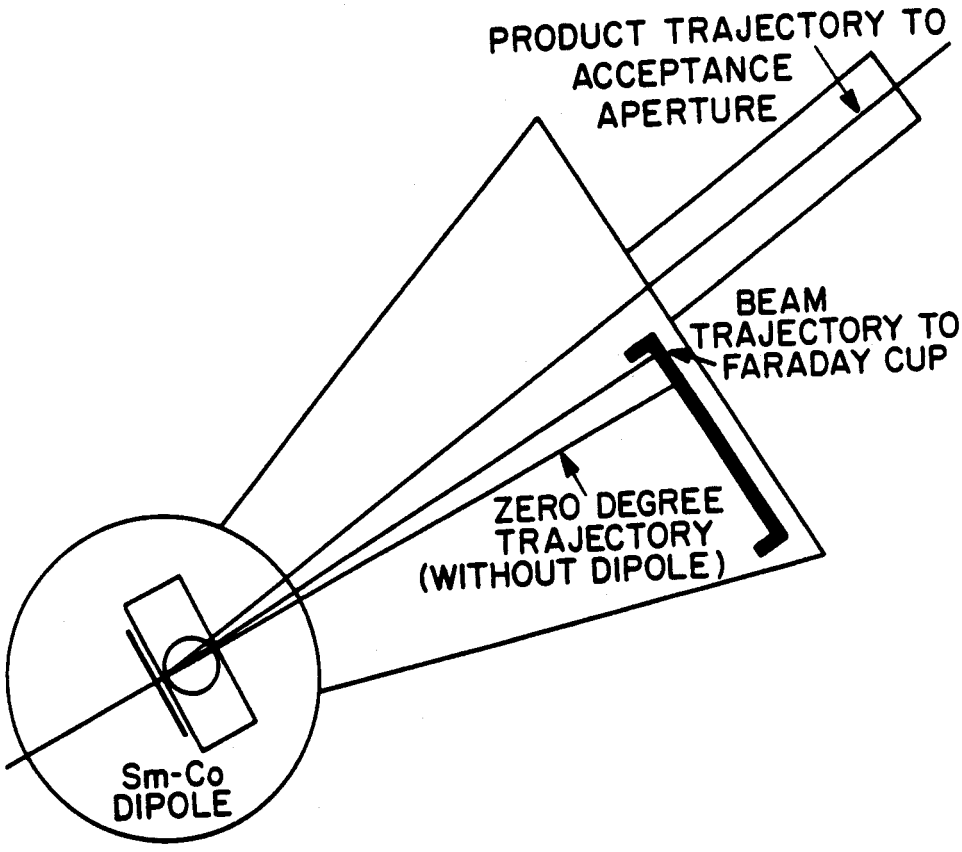

Figure 2.9: Schematic of the separation between the products and the beam-like particles in the wedge vacuum chamber.

the magnetic field vector, and that the particle path through the dipole can be approximated as a straight line. Of course, this small angle limit is the limit where $\tan\theta \approx \sin\theta \approx \theta$ in radians.

The Sm-Co dipole built for the RPMS was measured for its possible use in this experiment. A portable Hall probe was used to measure the field in a 0.25 inch grid throughout the 2x2 inch pole face and in the center of the 0.5 inch pole gap to check for uniformity. The 0.25 inch grid was used because the field of the dipole does not change appreciably inside a square of this size. Then a line was taken through the center of the dipole as the ion path, where the field is strongest ($B \approx 6$ kGauss), to calculate an upper limit of the bending angle. The straight line approximation turns out to be good since the average rigidity of the ions of interest is roughly 6 kGauss-meters, resulting in a horizontal displacement of about 0.1 inch from their point of entry to their exit from the dipole. Therefore the ions will not even be bent into the neighboring 0.25 inch grid (see Figure 2.10).

Such a magnet alone would not be strong enough to give sufficient separation between the reaction products and the beam in the S320 wedge chamber. A bend angle of at least 5° for the reaction products (about 3° for beam-like particles) was needed. Since the RPMS dipole gave almost 3° bend angle, a second dipole with a similar design was called for. A second dipole with a central field of approximately 5.5 kGauss was produced. Also, another existing permanent magnet dipole was used with a central field of 2 kGauss and a one inch path length. These three dipoles were mounted together and placed behind the target ladder in the target chamber as indicated in Figure 2.9. The three dipoles combined to give an angular separation of approximately 2.6 degrees between the beam and the reaction products.

To check the calculation, the dipoles were tested with an E/A = 8 MeV ^{36}Ar beam. According to the calculation, after passing through the target dipoles this

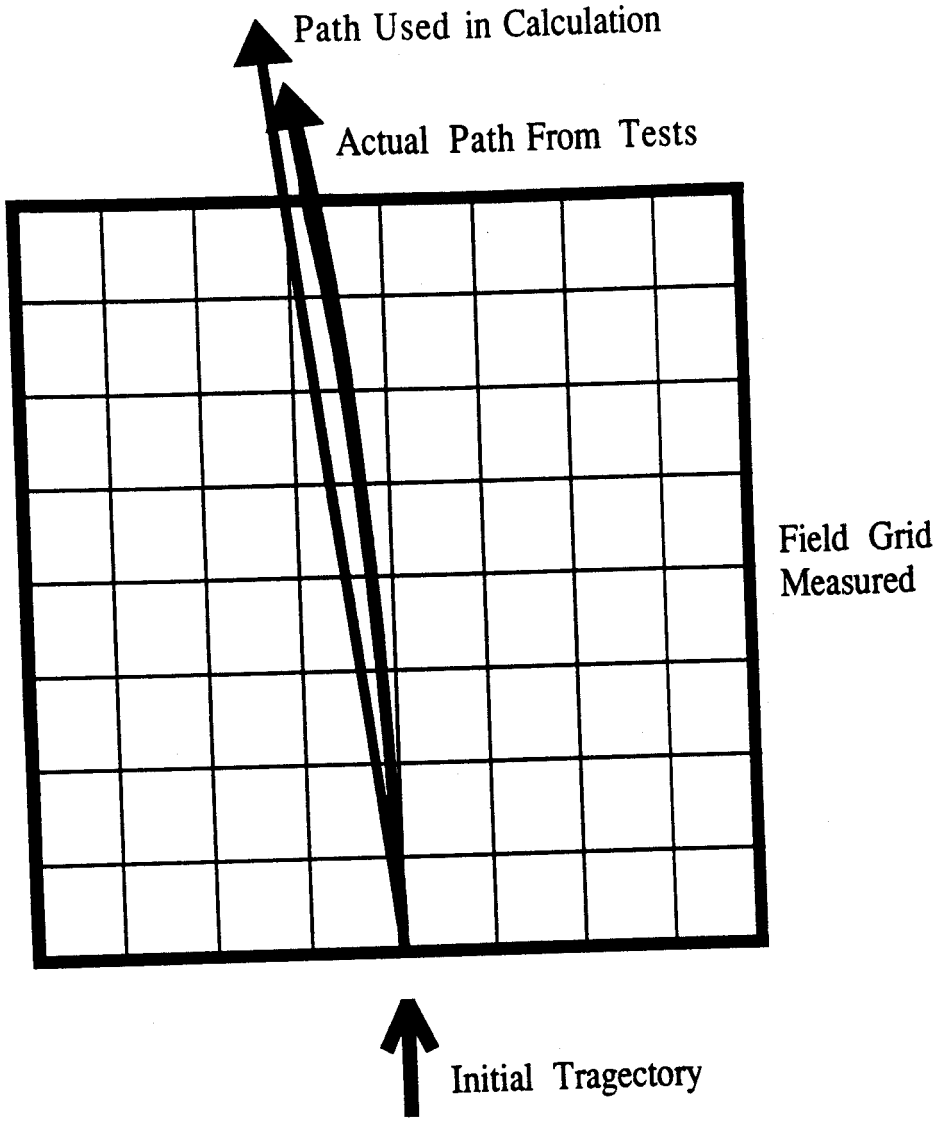

Figure 2.10: Illustration of the path of nuclei through the permanent dipole magnet. The central fields are used in the calculations since the particles are not bent into the neighboring grids.

beam should appear at the center of the S320 viewing plate with the spectrometer set at 4.5° in the lab. During the test, the beam was centered with the spectrometer at 4.65(1)°. After this test, the target dipoles were removed to check the zero degree mark of the spectrometer. This was done by centering the beam on the focal plane viewing plate, and adjusting the angle of the spectrometer in each direction until the aperture edge obscured the beam. The angle at each edge of the aperture was recorded, and the midpoint between these two angles was designated as the true zero degree mark in the lab. The measurement showed that the zero degree mark in the lab was at the indicated marking of 0.14(1)° on the S320 angle scale. Therefore, the beam angle after passing through the target dipoles was 4.51(1)°. This excellent agreement showed that the calculation was a good estimate of the offset angle for the evaporation products. It was thus determined that the spectrometer should be set to 7.18° in the lab to accept the zero degree reaction products and easily catch the beam-like particles in the wedge faraday cup between four and five degrees, as shown in Figure 2.9. This greatly reduced the background in the start detector and allows the experiment to run with a higher beam intensity.

Magnetic optics calculations using the code MIRKO[fra] also showed that these permanent magnet dipoles do not cause any detectable changes in the focal plane image. This result was also verified by observing E/A = 8.0 MeV ^{36}Ar elastic scattering peaks in ther S320 focal plane detector with and without the dipoles in place.

III EXPERIMENT

A DETECTOR CALIBRATIONS

It was important to calibrate the position and time of flight detectors and to determine the proper gas pressure necessary to stop the ions of interest in the ion chamber before the experiment was begun. For these tasks, an E/A=2.5 MeV ^{86}Kr beam was used. To calibrate the position detector, the beam was scattered from a 310μg/cm^2 Au target which produced numerous charge states. The spectrometer was set to observe the 7° elastically scattered ^{86}Kr (Figure 2.11) and the peaks corresponding to the different charge states were moved across the position detector in the focal plane by adjusting the spectrometer's magnetic fields. Then, knowing the mass (m), charge (q), dipole field (B) measured by an NMR probe, and incident energy of the ^{86}Kr, the bend radius (ρ) corresponding to the position of of the particle was calculated:

$$B\rho = \frac{mv}{q} \tag{2.3}$$

The bend radius was expanded in terms of the detector position (x) as follows:

$$\rho = a + bx + cx^2 + dx^3 + ... \tag{2.4}$$

In the present experiment, only the quadratic form of the polynomial was used. It is important to note that to perform this calibration the position in the detector representing the center of the focal plane must first be determined, since this corresponds to the central bend radius of the dipole magnet. The central bend radius has been previously measured[win90] to be 1.71918(1) meters. The center of the focal plane was found by placing a slotted mask (Figure 2.12) in front of the detectors that has a 0.5 mm slit at the position of the central bend radius. The spectrometer is then defocussed to fully illuminate the focal plane position detector with particles. The resulting pattern is shown in Figure 2.13. In this figure, the center peak is indicated,

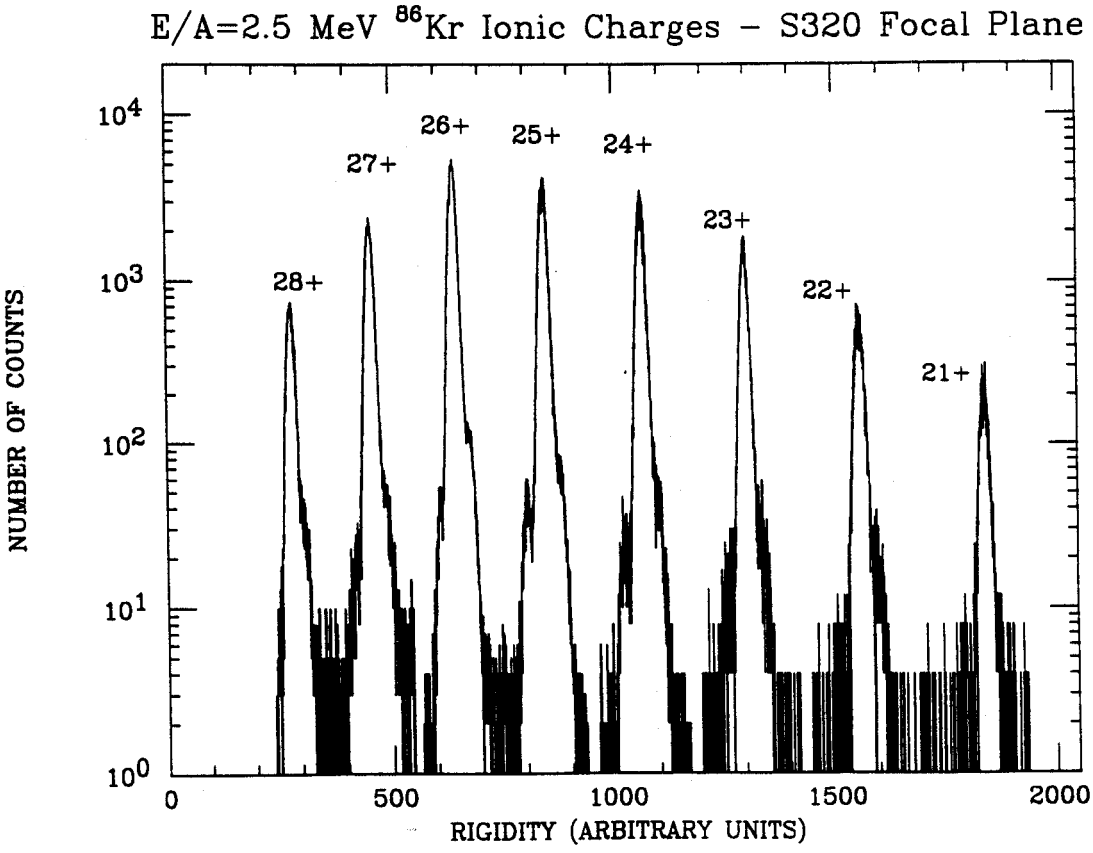

Figure 2.11: Charge state distribution for E/A = 2.5 MeV ^{86}Kr.

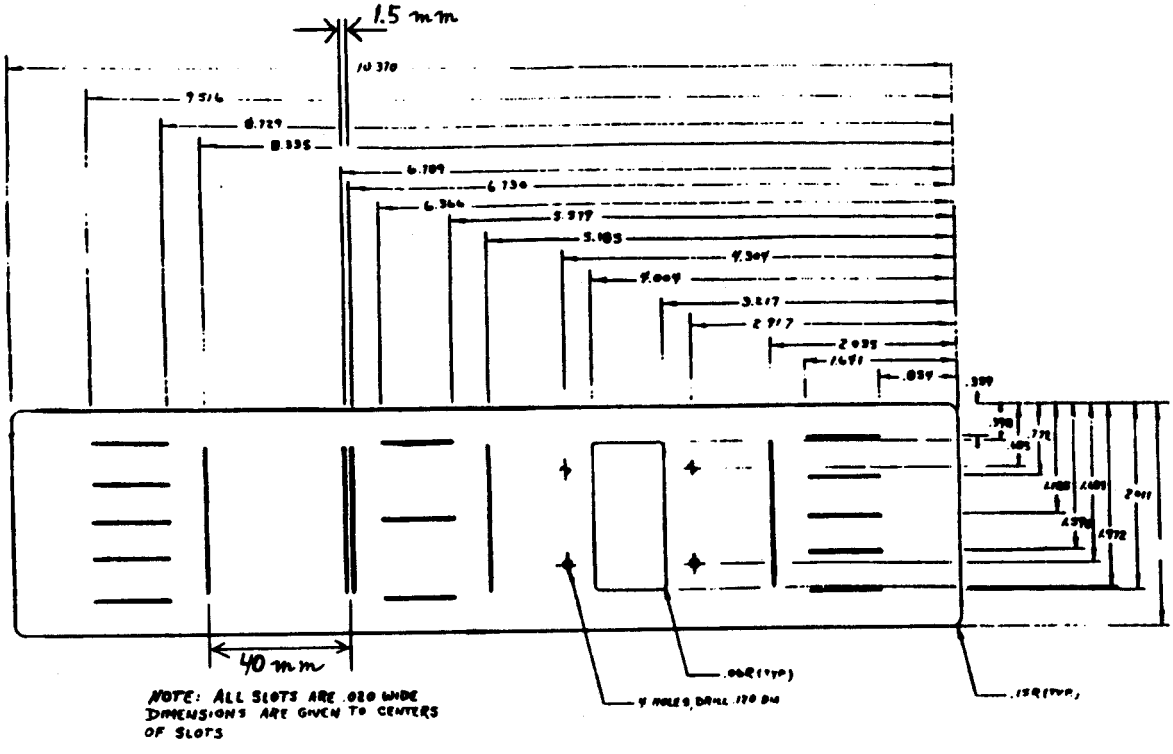

Figure 2.12: Mask pattern at the focal plane of the S320 spectrometer.

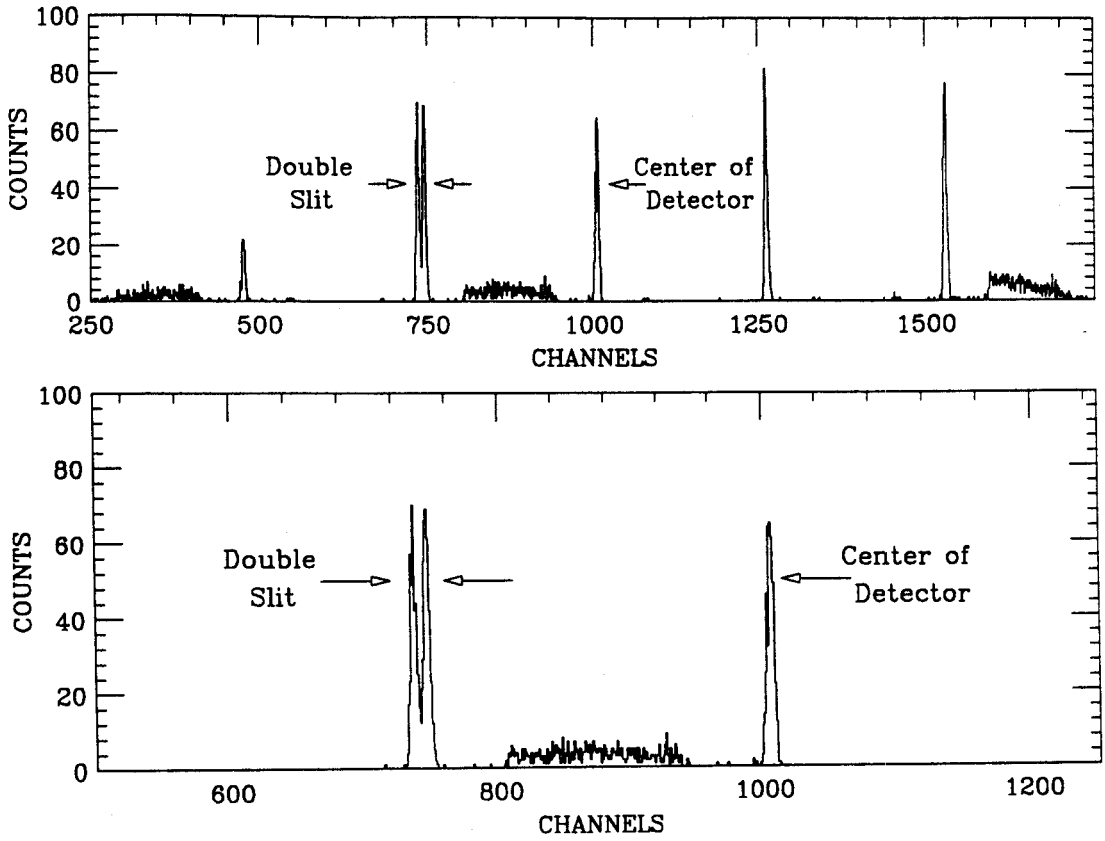

Figure 2.13: Position spectrum with S320 focal plane mask in place.

as well as two peaks corresponding to two 0.5 mm slits whose centers are separated by 1.5 mm (in other words, the edges are 1 mm apart). Gaussian fits were made to these peaks and the extracted position resolution was 0.6 mm FWHM.

The S320 magnet settings were adjusted until the centroid of the charge state peak with the highest count rate was located at the center of the position detector. An iterative approach was then used to assign the values of the charge states to the peaks. Using the formalism of (charge states)[mcm89] and the nominal beam energy, a first guess was made as to the charge state of this primary peak. Then, using the rigidity formula, Equation 2.3, the momentum of the beam was calculated. This was compared to the beam momentum expected at 7° from a relativistic kinematics calculation, taking into account the energy losses in the target and the start detector. If the two momenta agree within the nominal error of the beam energy (±2%), then the charge state was accepted. If not, then the momentum for the peak was recalculated using the rigidity formula for the next higher or lower charge state until agreement is reached. In a certain sense, this corresponds to determining the beam energy and the spectrometer calibration simultaneously with a consistent set of equations. This is possible because the atomic process of charge state production provides a number of calibration beams with integral charges. Through this procedure, the peak with the highest count rate was calculated to be $^{86}Kr^{26+}$ (Figure 2.11), and the beam energy was calibrated as E/A = 2.48 ± 0.05 MeV. Similarly, from the E/A = 8 MeV ^{36}Ar elastic scattering measurement, the beam energy was calculated to be E/A = 7.86 ± 0.05 MeV.

After the charge states were assigned and the momentum measured, the bend radius, ρ, for each position could then be calculated (Eq. 2.3) for the various dipole field settings of the spectrometer. A quadratic equation was fitted to both the krypton and the argon data to obtain the focal plane calibration shown in Figure 2.14.

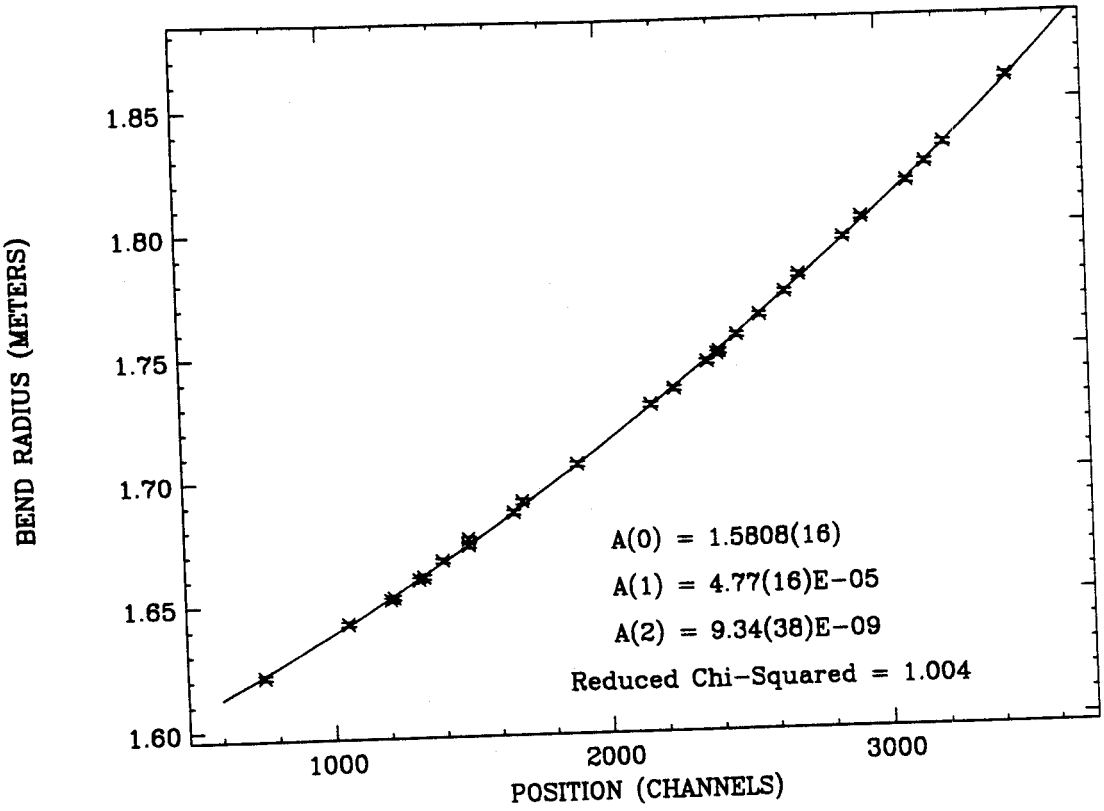

Figure 2.14: Rigidity calibration of the S320 focal plane.

With the momentum of the elastically scattered krypton ions calibrated, the time of flight (TOF) was easily calibrated with the same data. Figure 2.15 shows a schematic diagram of the detectors and electronics used to measure the TOF. The anode signal from the Breskin detector in the focal plane was used to start the time -to-analog-conversion (TAC) module, since this detector observed a lower rate of particles because of the selection made by the spectrometer dipole. The delayed start detector signal stopped the TAC timing, and the TAC signal produced was sent to an analog-to-digital (ADC) converter to be read by the data acquisition computer (see the Electronics section for further details). From Figure 2.15 it is clear that the time measured by the TAC (t_{TAC}) is simply:

$$t_{\mathrm{TAC}} = t_{\mathrm{DELAY}} - t_{\mathrm{FLIGHT}} \tag{2.5}$$

where t_{DELAY} is the difference in delay of the two detector signals before the TAC, and t_{FLIGHT} is the flight time of the ion between the start detector and the Breskin detector. The TAC full scale was set to 200.0 ns which was channel 4028 in the ADC display. Each krypton charge state was focussed on the center of the focal plane, where the spectrometer path length is known accurately, and the time peaks were measured. Each peak was then fitted with a Gaussian function and the centroids were converted from channels to nanoseconds. The flight time (t_{FLIGHT}) was calculated by dividing the flight path of 489.5(3) cm by the velocity calculated from the rigidity, Equation 2.3. Then, Equation 2.5 was solved for T_{DELAY} to give an average value of 328.9(2) ns. The flight times of the ions from the fusion/evaporation reaction, and therefore the velocities of the ions, could then be directly calculated.

Finally, it was necessary to determine the gas pressure necessary to stop the interesting ions in the ion chamber volume. The E/A = 2.5 MeV ^{86}Kr beam was scattered from a 1 mg/cm^2 carbon target which degraded the energy of the scattered beam to E/A = 1.8 MeV with the spectrometer set at 2.5° in the lab. The range

$$t_{TAC} = t_{CABLE\ 1} + t_{DELAY\ BOX} + t_{CABLE\ 2} - t_{FLIGHT} - t_{CABLE\ 3}$$

$$t_{DELAY} = t_{CABLE\ 1} + t_{DELAY\ BOX} + t_{CABLE\ 2} - t_{CABLE\ 3}$$

$$t_{TAC} = t_{DELAY} - t_{FLIGHT}$$

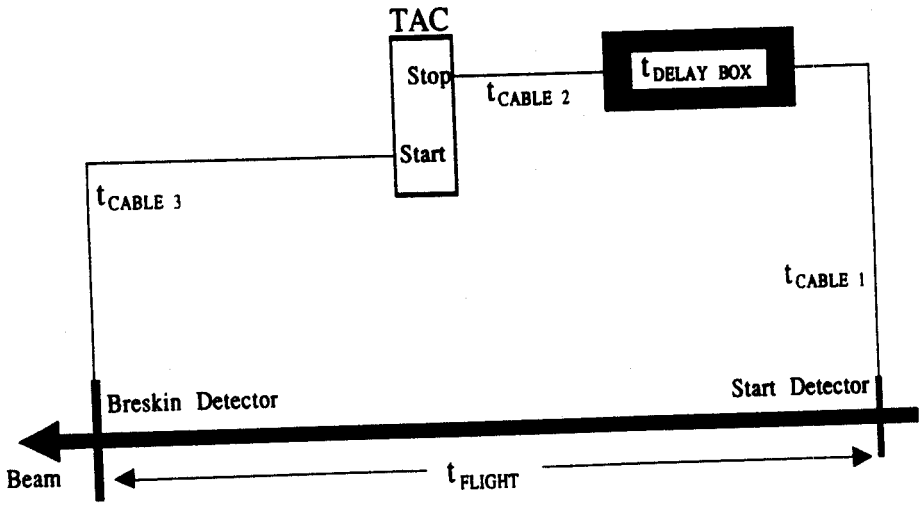

Figure 2.15: Schematic diagram of electronics and detectors used to measure the time of flight in the S320.

tables of Northcliffe and Schilling[nor70] were used to estimate the ranges of the ions in gas. It was calculated that if the ^{86}Kr ions were stopped at the last anode strip in the detector, then the ^{65}As ions from the fusion/evaporation experiment would stop approximately two-thirds of the way through the detector. The range tables indicated that approximately 21 torr of the 80% freon/ 20% isobutane gas mixture would stop the ^{86}Kr at the right position; however, during the test 27.5 torr of the gas was found to be needed. The coarse gains for the ion chamber anode shaping amplifiers were set so that the pulse heights from the degraded krypton ions were at 75% of full scale. Then, to set the fine gains for the shaping amplifiers, the elastically scattered E/A = 8.0 MeV ^{36}Ar from a 310μg/cm^2 Au target was used. These ions pass through the ion chamber, leaving approximately the same amount of energy in each strip, and stop in the plastic scintillator. The fine gains of the anode amplifiers were set so that the pulse heights for each strip were the same for the elastically scattered ^{36}Ar ions.

B Electronics and Data Acquisition

A schematic diagram of the electronics for this experiment is shown in Figure 2.16. There were 35 signals read by the front end computer for each trigger event: ADC and TDC signals for each of the ten anode strips, ADC signals for the left and right readout of the resistive position wires, charge-sensing ADC (QDC) signals for the back scintillator and the start detector scintillator, and TDC and TAC signals for timing against the cyclotron radio-frequency (RF). Also, the Breskin detector was set up with a TAC signal for the right side delay line readout of the cathode, as well as a TAC signal to measure the right delay line versus the left delay line to give position directly. There were also TAC's for the TOF measurements from the start detector to the Breskin detector, and two measurements from the start detector to the focal plane scintillator. Finally, there was a TAC to measure the drift time of the

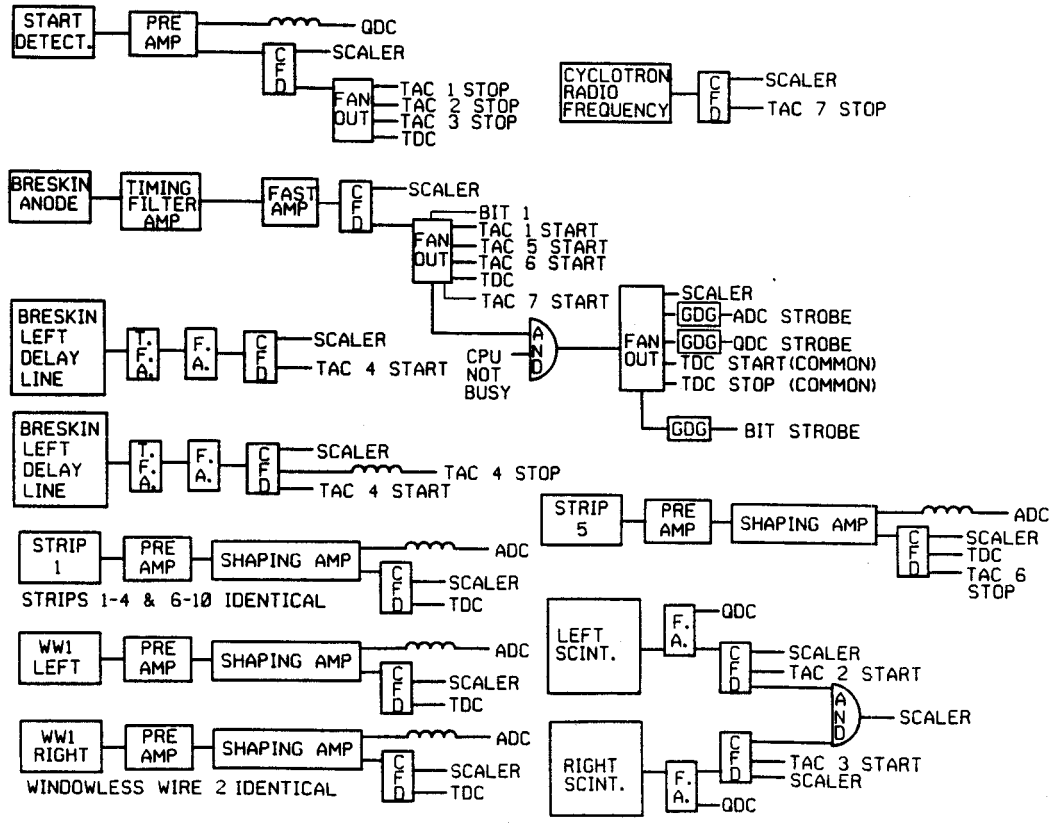

Figure 2.16: Schematic diagram of the electronics for the fusion/evaporation experiment.

electrons produced in the gas ionization to the fifth anode strip, which could be used to calculate the vertical position in the focal plane. The data acquisition hardware and software used to read the ADC's, TDC's, and QDC's and write the data to tape was the standard NSCL data acquisition system[fox89].

The event trigger was simply defined to be any signal above the constant fraction discriminator (CFD) threshold in the anode of the Breskin detector AND'ed with the NOT-BUSY signal from the front end computer. This gave a fast signal to trigger the electronics read-out whenever a particle entered the focal plane detector. The only other fast signal that might have been considered for the trigger was the start detector signal. Since the start detector gave signals for all the ions that pass through it and these do not necessarily have the correct rigidity to reach the focal plane detector, the start detector registered approximately 300 times more events than the focal plane detectors. It is obvious that such a trigger would have created a large portion of useless data on tape, and a large computer deadtime. This would further reduce the ability to detect rare events, such as ^{65}As, thus making the start detector a poor trigger choice.

Since the electronics were all triggered by the Breskin detector, the TDC's and some of the TAC's were operated in common-start mode. The time represented by such a measurement is really the difference between the stop signal time and some delay (see time calibration section for complete discussion). Some of the time signals, *i.e.*, the anode TDC's, were mostly diagnostic and were simply monitored to make sure the detectors were behaving properly.

The electronics modules that handled the signals for the Breskin detector were set up such that the left delay-line readout started a TAC and the delayed right delay-line readout was used as the stop. A second TAC was started by the Breskin anode signal and stopped by the right delay-line readout. A schematic of these TAC's is shown in

Figure 2.17. The first TAC then directly gave position of the ion in the focal plane. The purpose of the second TAC was to determine simultaneous multiple hits in the focal plane which give ambiguous signals in the ion chamber and the position TAC. With this configuration, a parameter can be calculated in the analysis software that is

$$TAC_{\text{POSITION}} - (2 \times TAC_{\text{RIGHT DELAY}}) = CONSTANT. \quad (2.6)$$

Figure 2.17 illustrates that this will be a constant value for single ion events in the detector. This parameter can then be displayed as a histogram, and gates can be established on the peak representing single events to exclude ambiguous events. However, in the early stages of the experiment the occurrence of multiple events was found to be rare, so this gate was actually not necessary in the analysis.

The remaining electronics modules were set up in the standard fast-trigger S320 configuration described in the S320 manual[win90]. The only other unique problem faced by this experiment was that there were some background beam events in the focal plane detectors, even with the permanent dipole magnets in place. These events had a much lower energy-loss in the first few ion chamber anode strips than the nuclei of interest, and a software threshold set on these strips in the front end computer kept from writing the background events onto the data tapes. This reduced the number of data tapes written by a factor of two or three, and thus simplified the data analysis process.

IV RESULTS

A ELEMENT (Z) RESOLUTION

The anode signals were checked for any positional dependences throughout the course of the experiment. The pulse height signals from each anode were plotted versus

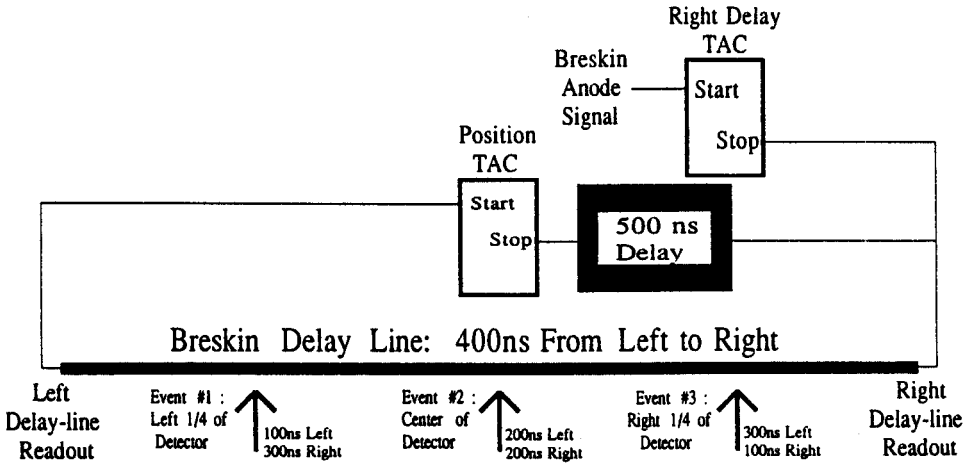

Single Events (Assume signal cable times cancel)

Event #1 : Position TAC = 300 + 500 - 100ns = 700ns
Right Delay TAC = 300ns
Position TAC - 2(Right Delay TAC) = 100ns

Event #2 : Position TAC = 200 + 500 - 200ns = 500ns
Right Delay TAC = 200ns
Position TAC - 2(Right Delay TAC) = 100ns

Event #3 : Position TAC = 100 + 500 - 300ns = 300ns
Right Delay TAC = 100ns
Position TAC - 2(Right Delay TAC) = 100ns

Simultaneous Multiple Events

Events #1 and #2 :
Pos. TAC - 2(R. D. TAC) =
600 - 2(200) = 200ns

Events #1 and #3 :
Pos. TAC - 2(R.D. TAC) =
500 - 2(100) = 300ns

Events #2 and #3 :
Pos. TAC - 2(R.D. TAC) =
400 - 2(100) = 200ns

Figure 2.17: Illustration of Breskin detector position measurement and the ability to reject simultaneous events.

position, and some positional dependence was apparent in both the first and tenth strips (Figure 2.18). As in the early test runs, these nearly matched the positions of the argon elastic scattering peaks that were used in the calibration of the spectrometer rigidity. However, it made little sense that a position dependence should exist only for the first and last anodes in the detector. Also, if there was any degradation of signal due to some kind of deposit on the anode, then this should be even more evident on the windowless wire detectors, since they have much higher voltages and a higher field gradient around the wires. However, when the pulse height signals from the left and right sides of the windowless wires were plotted versus position, the problems were seen in the first and last anode strips were not present.

This mystery was solved when the position was calibrated in centimeters and it was found that the dips shown in the spectra of Figure 2.18 have exactly the same spacing as the three screws that support the field shaping windows in the front and back of the detector. Further investigation of the detector after the experiment showed that the detector had been assembled with metal rather than nylon screws. These metal screws apparently distorted the electric field in the front and back of the ion chamber enough to effect the ion collection efficiencies at the positions of the screws. Looking back at the first test run with the wire anodes, it is not clear that the distortions in that case lined up with the metal screws also found in that detector. The distortions were obviously more extreme than in the latter case of the anode strips, but the field gradients were higher for the wire anodes than for anode plates. It is possible that the irregularities were a combination of detector aging and the field distortions of the metal screws. The prototype detector, which showed no such positional dependences, was found to have the same metal screws in the the field shaping windows. In this case it is postulated that the use of larger anode plates and low detector voltages masked any field distortions. It may be possible that the segmented anode detector

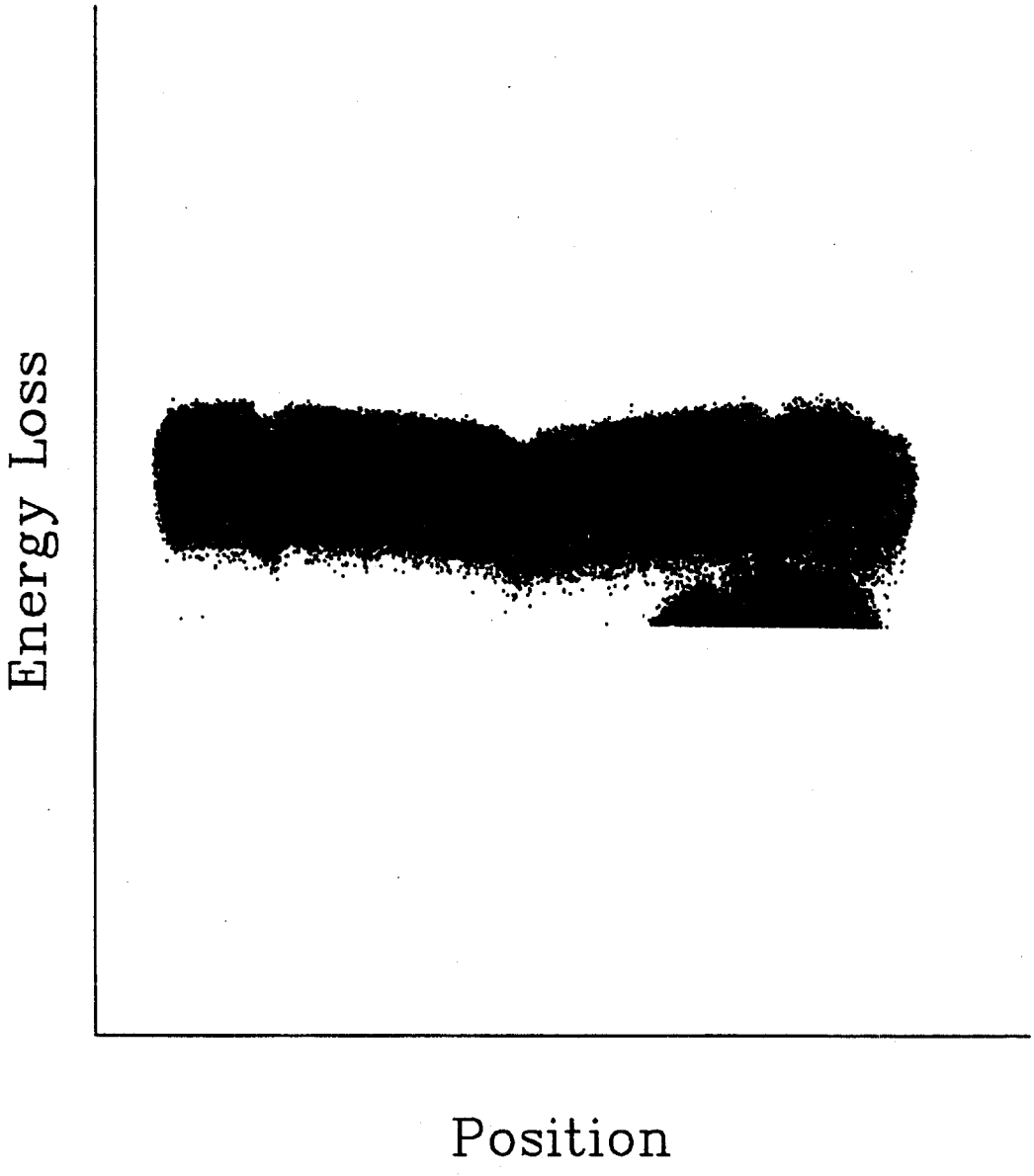

Figure 2.18: Position dependence of the first anode strip of the S320 ion chamber.

used in the present experiment will operate well using pure isobutane gas when the nylon screws are used to attach the field shaping strips. Further detector aging tests must be done to understand this matter more fully.

A position dependent gain factor was used to correct the dips in the first and last anodes. This worked well, and no other problems were encountered in the energy signals due to this positional dependence. The energy signals were also plotted versus ion path angle in the detector. No significant dependence could be observed due to the various angles of travel through the detector. At this point, the Z identification plots could be produced.

Figure 2.19 shows how the residue Z from the ^{36}Ar on ^{40}Ca reaction was identified. The sum of the energy loss in the first seven anode strips (ΔE_7) is plotted against the sum of all ten strips, ΔE_{10}, and the Z lines are resolved up to Z=32 (Ge). The Z lines are bounded on the upper left by the *punch in* line, which contains the ions that either just make it into the detector and stop in a distance shorter than the strips that make up the ΔE_7 signal. On the lower right the Z lines are bounded by the *punch through* line. This contains ions that pass through the entire ion chamber volume and into the plastic scintillator. The summed energy loss signals from only the first five anode strips (ΔE_5) versus ΔE_{10} (Figure 2.20) shows that a number of the ions on the punch in line in Figure 2.19 have moved out onto the Z lines. As expected, the new Z lines are also broadened a bit due to the effects of energy loss straggling. This effect is more clearly illustrated in Figure 2.21, in which the ΔE_3 is plotted against ΔE_{10}. These Z lines are not as well separated since the energy-loss straggling has become large compared to the ΔE signal. But it is also apparent that the higher Z bands are moving off the punch in line and are more easily resolved. These figures illustrate how changes in the choice of ΔE effect the Z resolution in these spectra. In the final analysis, ΔE_5 versus ΔE_{10} was found to give the best overall Z separation

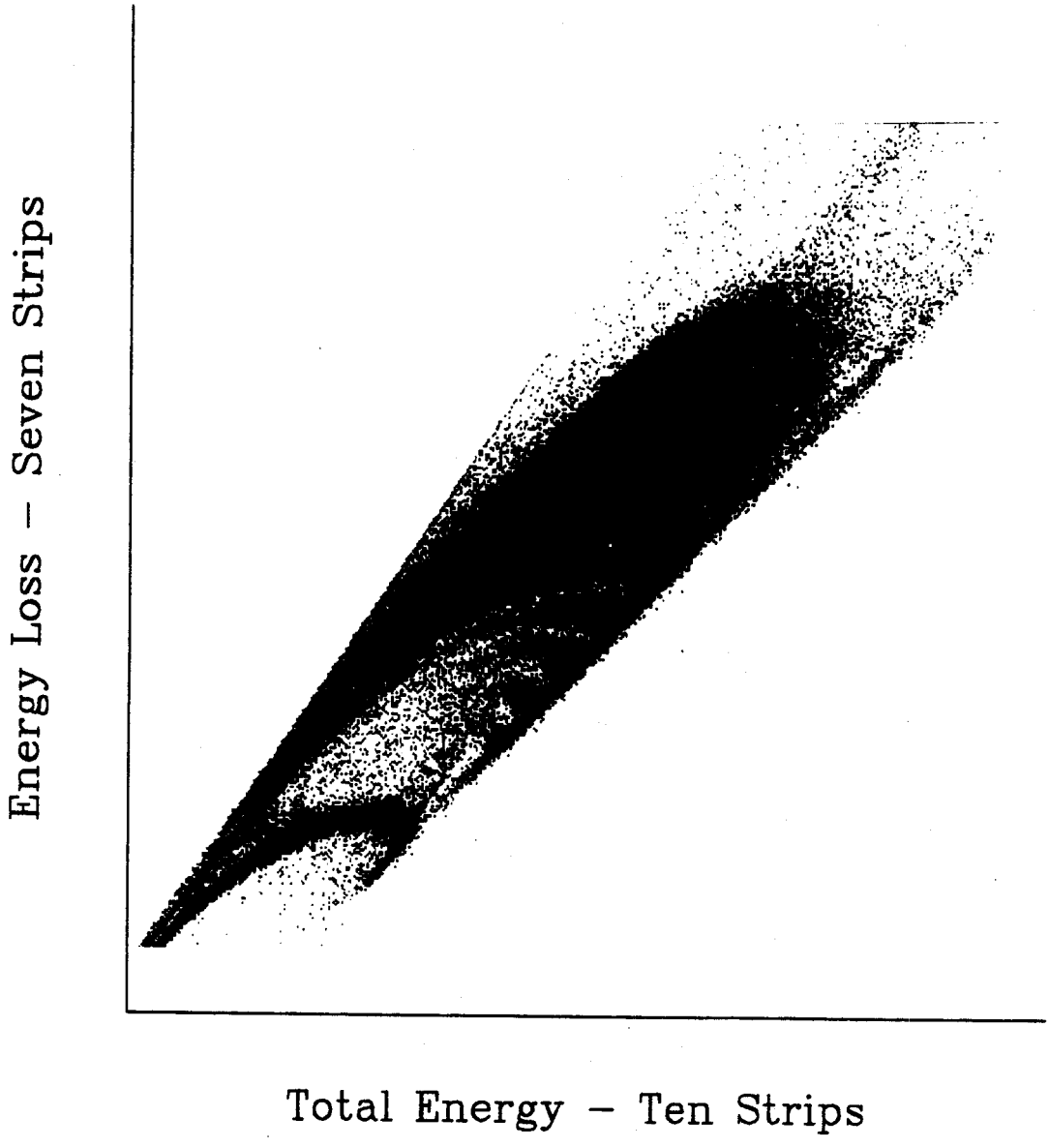

Figure 2.19: The sum of the energy loss in the first seven anode strips (ΔE_7) in the S320 ion chamber versus the sum of all ten strips, ΔE_{10}.

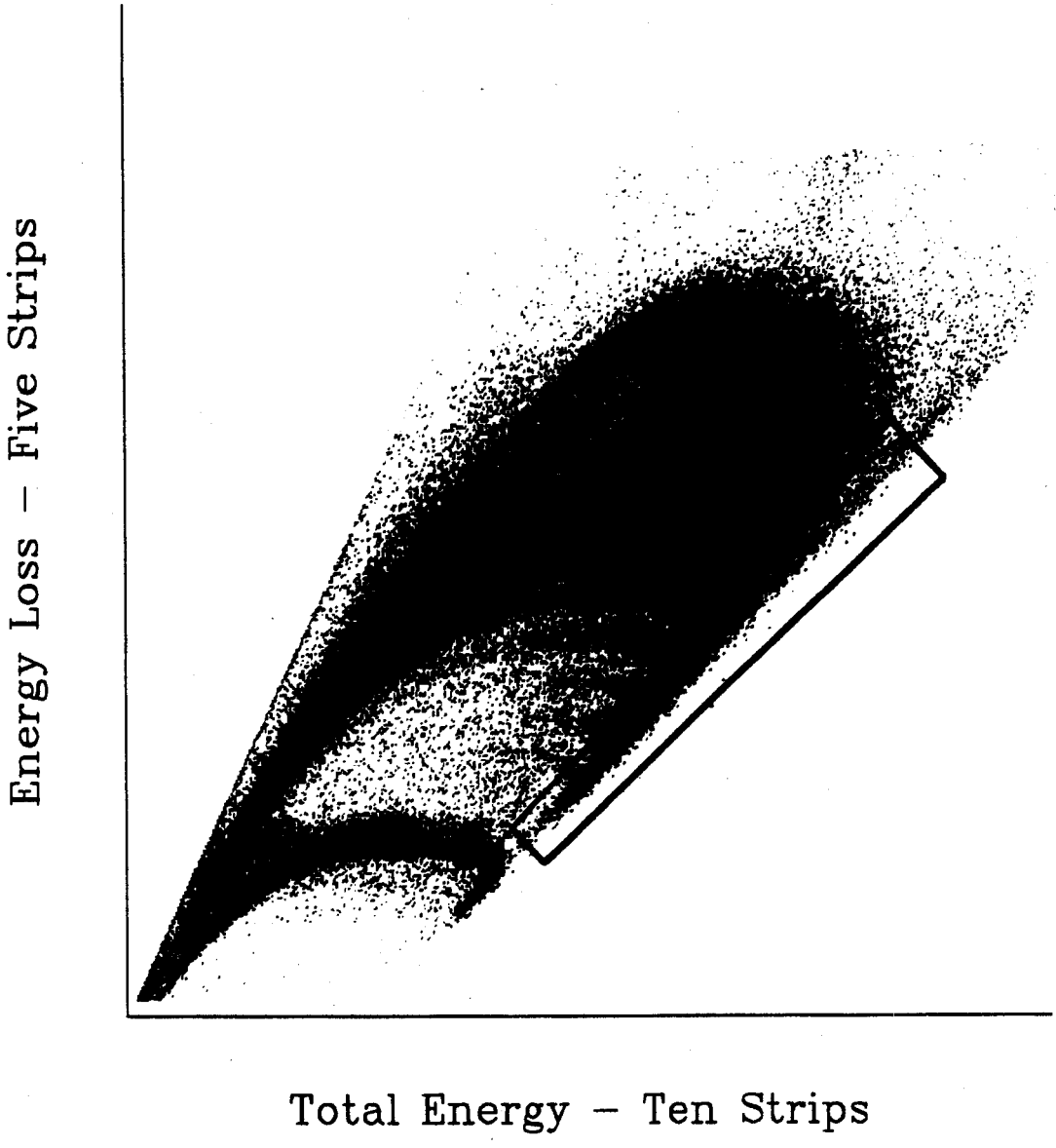

Figure 2.20: The sum of the energy loss in the first five anode strips (ΔE_5) in the S320 ion chamber versus the sum of all ten strips, ΔE_{10}.

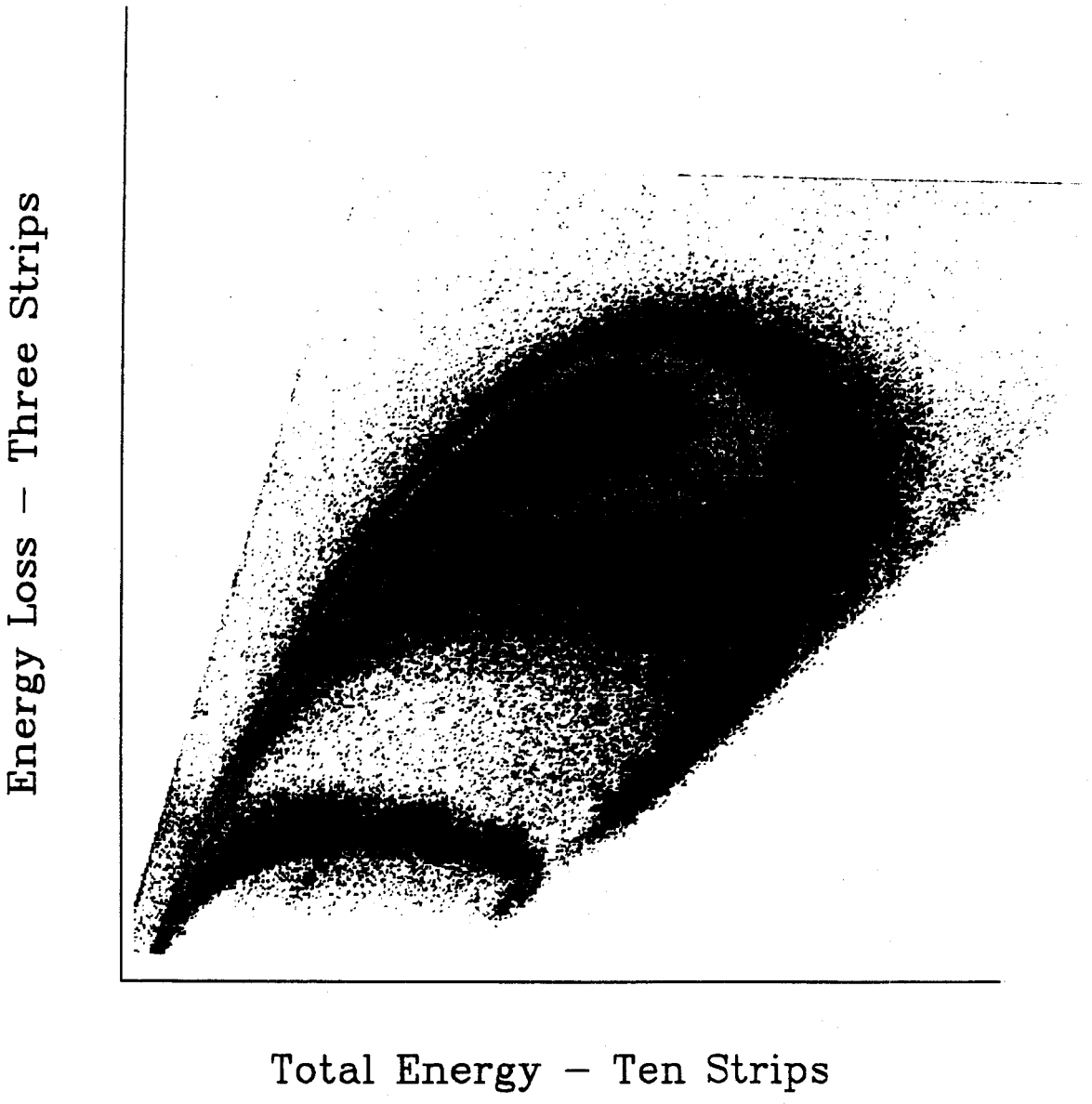

Figure 2.21: The sum of the energy loss in the first three anode strips (ΔE_3) in the S320 ion chamber versus the sum of all ten strips, ΔE_{10}.

for the ions of interest.

Another way to identify the reaction product Z is to plot the energy loss versus the TOF (Figure 2.22). If the energy loss from all ten anode strips, ΔE_{10}, is plotted versus the time of flight then the Z's become resolved for the events that were on the punch through line of the ΔE_5 versus ΔE_{10} spectra. Therefore, a broader gating scheme can be implemented where both spectra can be used to determine the Z's of the ions. First, a gate is drawn around a resolved Z in the ΔE_5 vs. ΔE_{10} spectrum. A second gate is drawn to include the punch through events for the same Z on the same spectrum (see Figure 2.20 – two gates are necessary because of the way the analysis code interprets them). The logical OR of these two conditions is applied to make the ΔE versus TOF spectrum shown in Figure 2.23. Several Z lines are shown in this figure above a certain velocity, representing the unresolved Z's on the punch through line. However, in the lower velocity region of the spectrum, it is clear that the ΔE_5 vs. ΔE_{10} Z-gate selects only one Z and some background events. A gate is then drawn on this spectrum around the Z of interest, as illustrated in the figure, and the higher velocity ions are selected. The logical AND of the ΔE_{10} vs. TOF Z-gate and the ΔE_5 vs. ΔE_{10} Z-gate is made to select a single Z of interest over a broad range of velocities.

At this point in the analysis, much consideration was given to the events that were still unresolved on the punch in line of the ΔE_5 vs. ΔE_{10} spectrum. Some events corresponding to Z = 34 – 38 were expected, yet Z = 33 was barely observed. A comparison of the number of resolved events to unresolved events showed that approximately 70% of the reaction products were on the punch in line. To investigate this matter further, an ungated TOF spectrum was made, as well as an energy - per - mass unit (E/A) spectrum. The E/A parameter was calculated from the TOF as

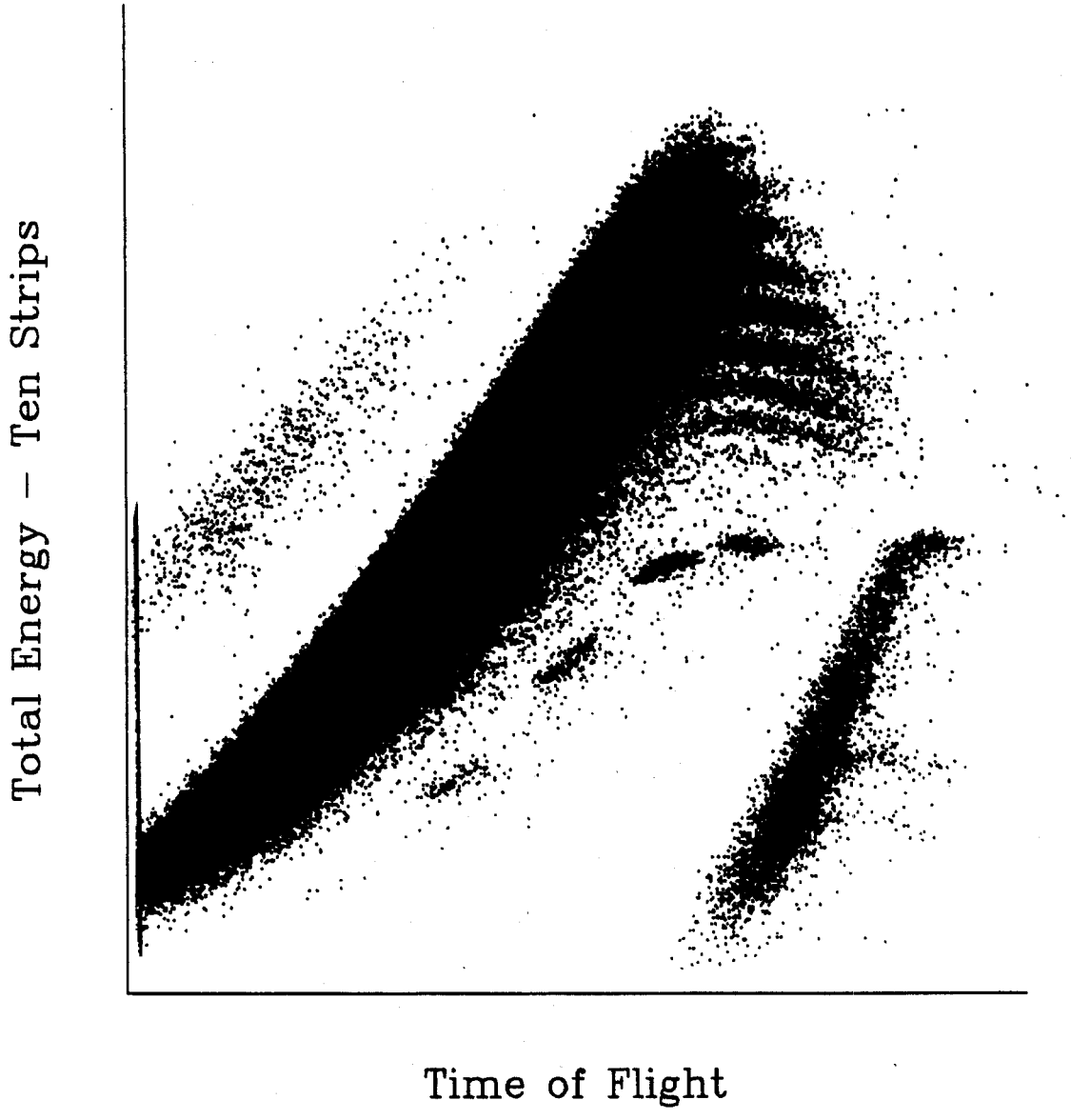

Figure 2.22: Energy loss in the S320 ion chamber versus time of flight.

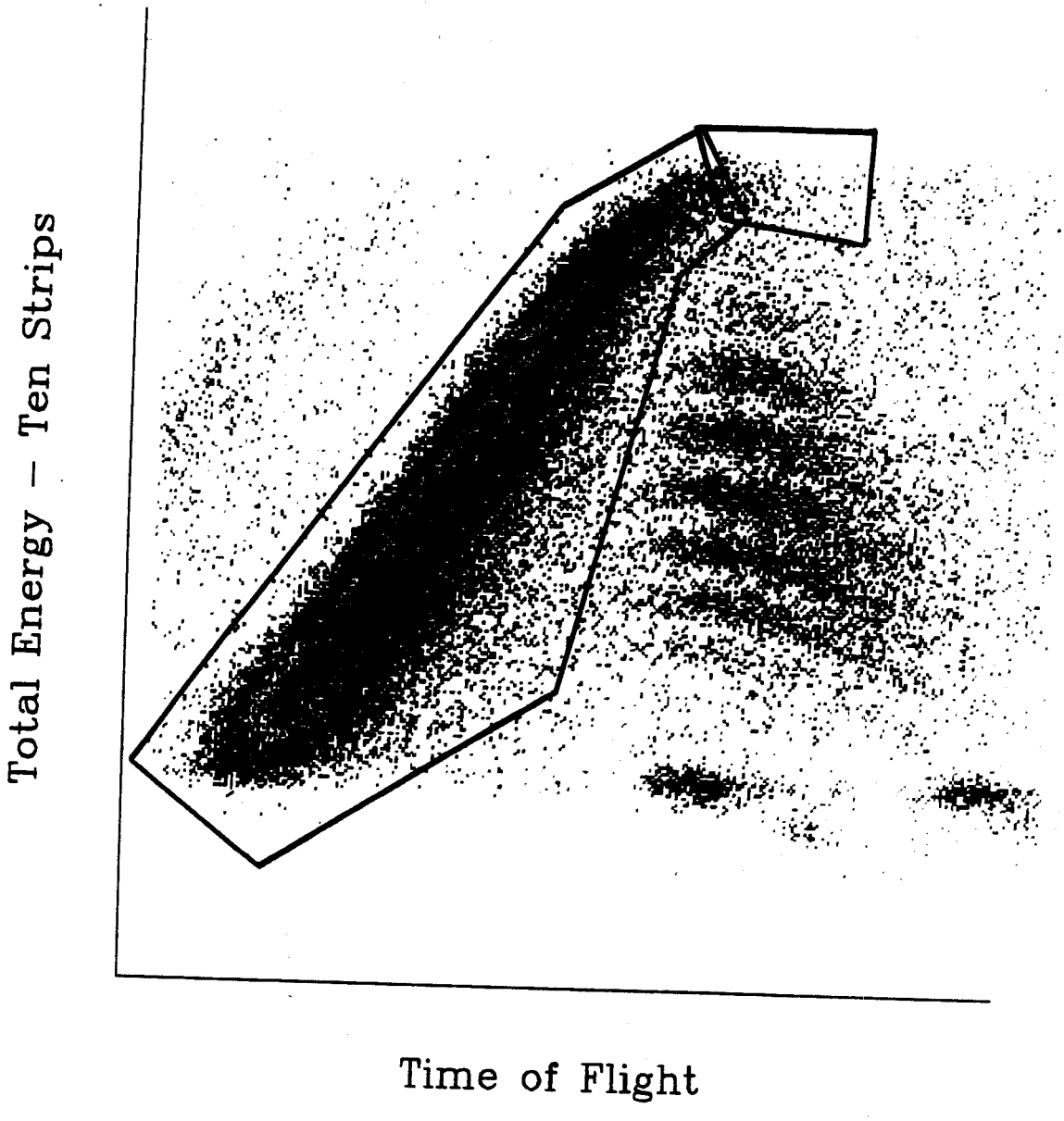

Figure 2.23: Energy loss in the S320 ion chamber versus time of flight, gated on Z = 29 in the energy loss versus total energy spectrum.

follows:

$$v = \frac{\ell}{t_{FLIGHT}}, \tag{2.7}$$

$$E = \frac{1}{2}mv^2 \tag{2.8}$$

$$\approx \frac{1}{2}A \cdot \left(931.5\frac{\mathrm{MeV}}{\mathrm{c}^2}\right)v^2 \tag{2.9}$$

$$= \frac{A \cdot 931.5\mathrm{MeV}}{2} \cdot \beta^2, \quad then \tag{2.10}$$

$$\frac{E}{A} = \frac{931.5\mathrm{MeV}}{2} \cdot \beta^2 \tag{2.11}$$

where v is the ion velocity, ℓ is the path length of the spectrometer, m is the mass of the ion, A is the mass number of the ion, and $\beta = v/c$. The Figure 2.24 shows the the ungated E/A spectrum with the spectrometer set at 3.474 kG. As expected, the figures have a distribution of energies and velocities peaked at E/A = 1.8 MeV. The same spectrum gated on resolved Z's (Figure 2.25) shows that the resolved ions all have energies greater than E/A $\approx$ 2.5 MeV. According to the initial predictions from the energy loss tables of Northcliffe and Schilling[nor70] there should not have been a problem resolving the ions with energies as low as E/A = 1 MeV. Subsequent calculations using the parameterization of Hubert[hu89] showed similar results, as did the calculations of Ziegler[zie85].

All of the calculations indicated that there was a reduction in the collection efficiency of the ionization created by the low energy events. In fact, the recent work of Vineyard, *et al.*[vin87], on a Bragg curve detector indicates that ion recombination and electron attachment are serious problems in slow heavy ion detection. Ion recombination occurs when an electron and a positive ion produced along the track of a detected particle combine to form a neutral gas molecule and a photon. Since the electron is not observed at the anode the energy loss information it represents is lost and the signal is reduced. The losses due to this process depend on the concentration

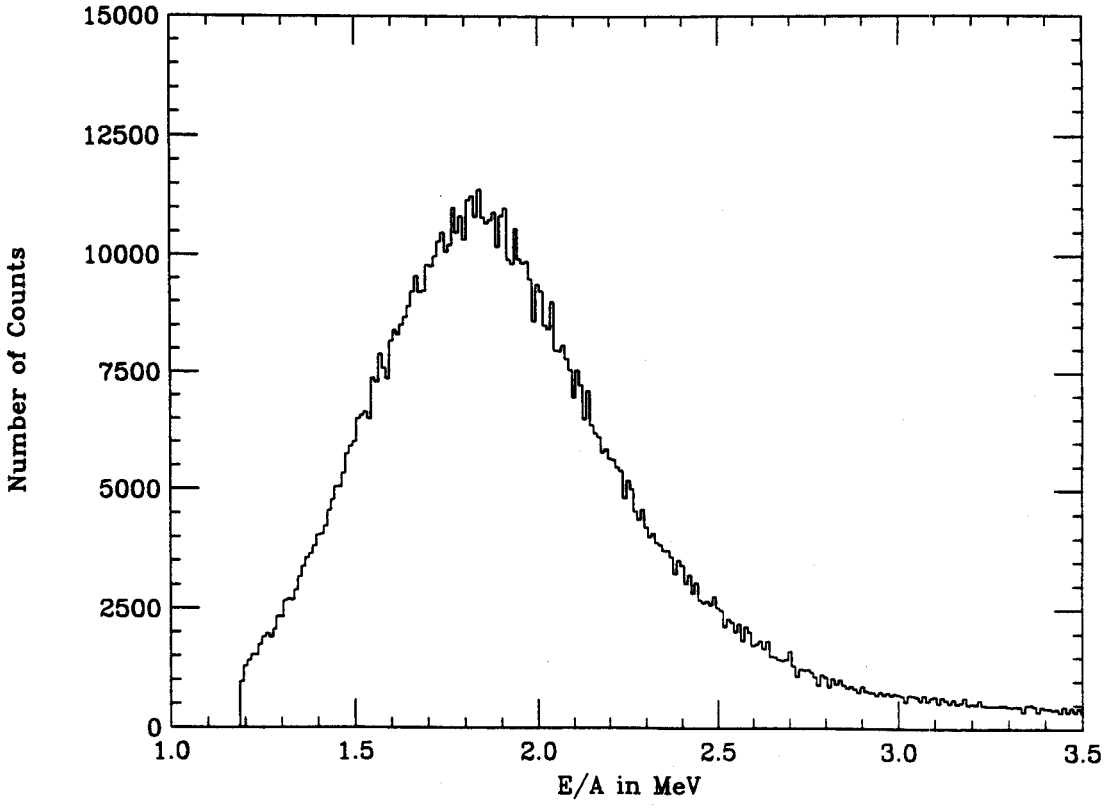

Figure 2.24: E/A spectrum with the S320 set at 3.474 kG.

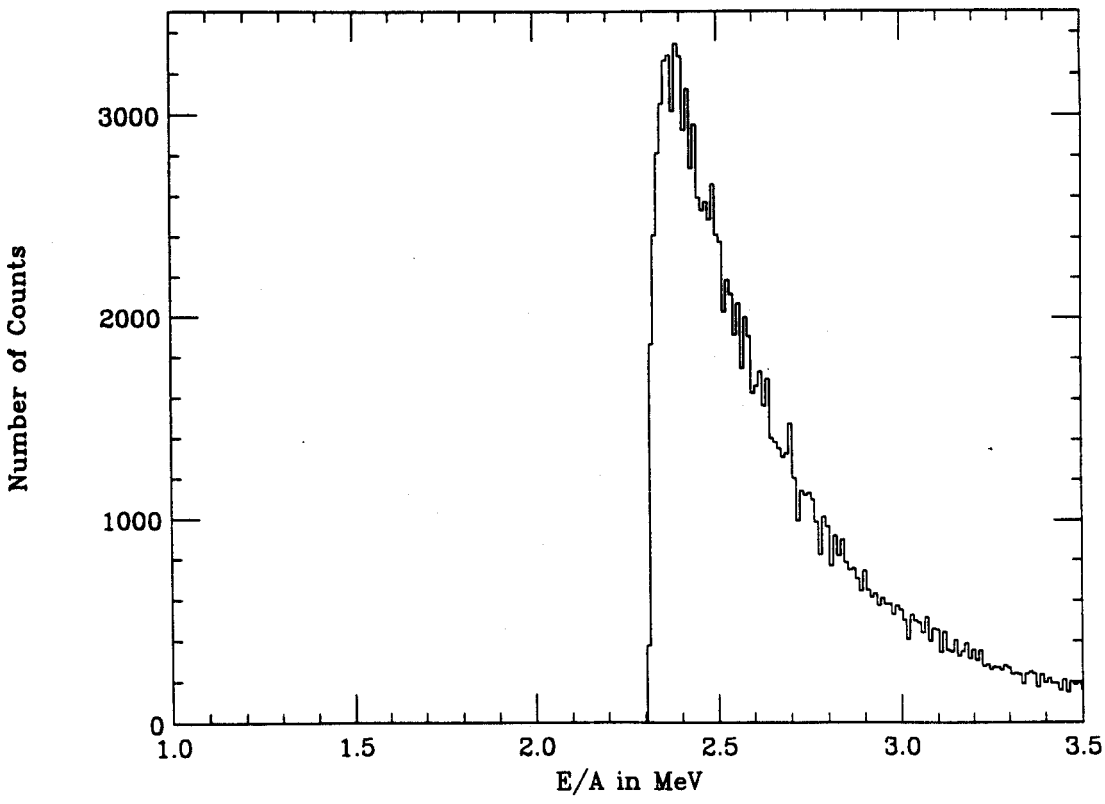

Figure 2.25: E/A spectrum with the S320 set at 3.474 kG, gated on the resolved elements in the energy loss versus total energy spectrum.

of positive and negative ions along the ionization path. Since slow heavy ions lose their energy rapidly along relatively short path lengths, ion recombination is important. To combat this problem, the detector voltages were kept as high as possible without causing electrical breakdown (sparking) in the gas volume. This kept the electron velocities high and reduced the probability for an interaction with a positive ion that would lead to recombination. Also, the large volume of the detector and low gas pressures lengthened the ionization path and helped reduce the concentration of positive ions and electrons.

The problem of electron attachment is a more likely hindrance. Electron attachment is the process whereby a component or contaminant in the detector gas with a high electron affinity captures free electrons produced along the ionization track of the detected particle. As the negatively charged gas contaminants are much more massive than electrons, they travel slowly towards the anode (approximately two orders of magnitude slower) and therefore are not integrated in the signal produced by the drifted electrons. The captured electrons cause a reduction in the anode signal and reduce the detector resolution. In the tests performed using the freon/isobutane mixture with the prototype detector, electron attachment did not seem to be a significant problem because the higher Z's (35,36,37) at E/A = 10 MeV were easily resolved. These results were extrapolated back to the much lower gas pressure needed to stop the E/A = 1.8 MeV ions and sufficient energy resolution was anticipated to resolve the Z's. The problem with such an extrapolation is that the gas pressure for the lower energy ions would be lower by a factor of three, so if the outgassing rate for a given detector is assumed to approximately constant, the partial pressure of the contaminant gasses would then be greater. Considering also that the segmented ion chamber had three times as many components in the gas volume that would outgas, such as cables and electronic boards, it is more conceivable that the resolution would

be greatly reduced in the experiment compared to the prototype test. Vineyard, *et al.*[vin87], have demonstrated the ability to obtain energy resolution of better than 1%, compared to the 6% energy resolution obtained from the segmented anode detector.

B Mass Resolution

The energy information from the ion chamber, the ion velocity from the time of flight measurement, and the rigidity from the focal plane position and dipole field measurements can be combined to calculate the ion masses for a selected element (Z). A low resolution value of the mass is calculated from the ion chamber energy measurement and the velocity (eqn. 2.9) and substituted into the rigidity equation (eqn. 2.3) to calculate the ionic charge. A particular ionic charge is selected and the mass is recalculated from the rigidity equation with the ionic charge as an integer value. The mass resolution is then sufficient to separate and identify the masses of interest, since the resolution results only from the errors in the velocity and rigidity. These errors are easily kept smaller than one percent.

The initial mass calculation is made by solving equation 2.9 for A as follows:

$$A = \frac{2Ec^2}{931.5v^2} \tag{2.12}$$

In this equation A is calculated in mass units, E is the total energy from the ion chamber (ΔE_{10}) in MeV, v is the velocity calculated from the time of flight, and c is the speed of light in the same units as v (cm/ns was generally used). The calculation is only valid if an ion is stopped in the ion chamber volume, otherwise ΔE_{10} does not represent the total energy. The ionic charge of the particle is then determined by solving equation 2.3 for q and substituting the value of A from equation 2.12:

$$q = 3.107 \cdot \frac{A}{B\rho}\frac{v}{c} \tag{2.13}$$

In this equation q is expressed in unit charges, A in mass units, $B\rho$ in Tesla-meters, and v and c in cm/ns. The ionic charge in equation 2.13 is not calculated as a discrete value because of the errors in the values used to derive it. However, since ionic charge is an integer quantity, the events that lie in a given q peak are selected in the software and assigned an integer value. Then the masses of these ions are recalculated by solving equation 2.13 for A with q as an integer, and do not reflect the error in the q calculation.

At first, this may seem a circuitous means of deriving the mass; however, if the errors of the measured and calculated values are considered at each step, the merits of the calculation are obvious. For example, in this work ^{65}As is one nucleus of interest. Its mass number (A) is 65, its element number (Z) is 33, and its average charge state (q) in this experiment is calculated to be 20. In order to resolve the mass of this nucleus from the ion chamber and time of flight information alone, the propagated error in equation 2.12 would have to be 1/65 or less. The velocity is known to one part in 150, so the energy measurement in the ion chamber must be known to better than two percent. But by using the value of A from equation 2.12 to calculate q in equation 2.13, the energy resolution required of the ion chamber to resolve the ionic charges is only one part in 20 (five percent). Here, again, the errors on the velocity, bend radius (one part in 600), and dipole field (one part in 10,000) are small compared to that of the ion chamber energy measurement. Then the mass is recalculated with equation 2.13 using the integer value of the selected q. The resolution of this recalculated mass is simply the propagation of the errors in velocity, bend radius, and dipole field, and does not reflect the error in the ionic charge calculation.

This method can be illustrated using the resolved copper isotopes (Z=29) at a spectrometer setting of 0.59 Tesla-meters. Since the energy resolution of the ion chamber (about six percent FWHM) was insufficient to resolve the q's to full-width at

half-maximum, there will be some significant contamination in the mass spectra due to miss-assigned ionic charges from the tails of neighboring q peaks. Such contamination can lead to the false identification of isotopes that were not produced in the reaction. Because of this limitation and the poor resolution of the Z's greater than 30, the results of this particular experiment cannot be used to identify new isotopes. However, the following exercise will illustrate the merits of this method of analysis.

Figure 2.26 shows the mass calculated from equation 2.12 for the copper isotopes using the ion chamber energy signal and the velocity calculated from the time of flight measurement. Though the masses are not resolved, separation in q was obtained using these values in equation 2.13 as shown in Figure 2.27. Then, a particular ionic charge was chosen ($q = 21$) and a tight gate was placed in this peak to minimize contamination from neighboring ionic charges. Equation 2.13 was then solved for the mass (A) with $q = 21$, and the spectrum in Figure 2.28 resulted. In this spectrum, the mass resolution is determined simply by the velocity and rigidity resolution. However, the contamination in these mass spectra due to neighboring ionic charges in the q gate gives a value roughly two mass units higher for $q-1$ or two mass units lower for $q+1$ for a given mass. This re-emphasizes the need for well resolved ionic charges (energy resolution of a few percent or less) in this type of analysis.

The assignments of the q's in Figure 2.27 must be made with some caution. If equation 2.3 is solved for q and the mass from equation 2.9 is substituted, the following expression results:

$$q = \frac{2E}{B\rho v} \tag{2.14}$$

The measurement of $B\rho$ and v correspond to some energy, E_0 of an ion as it passes through the dipole of the spectrometer. However, the measured E of equation 2.14 corresponds to the energy detected in the ion chamber after losing some energy, ΔE, in the Breskin detector and ion chamber windows. So the energy in equation

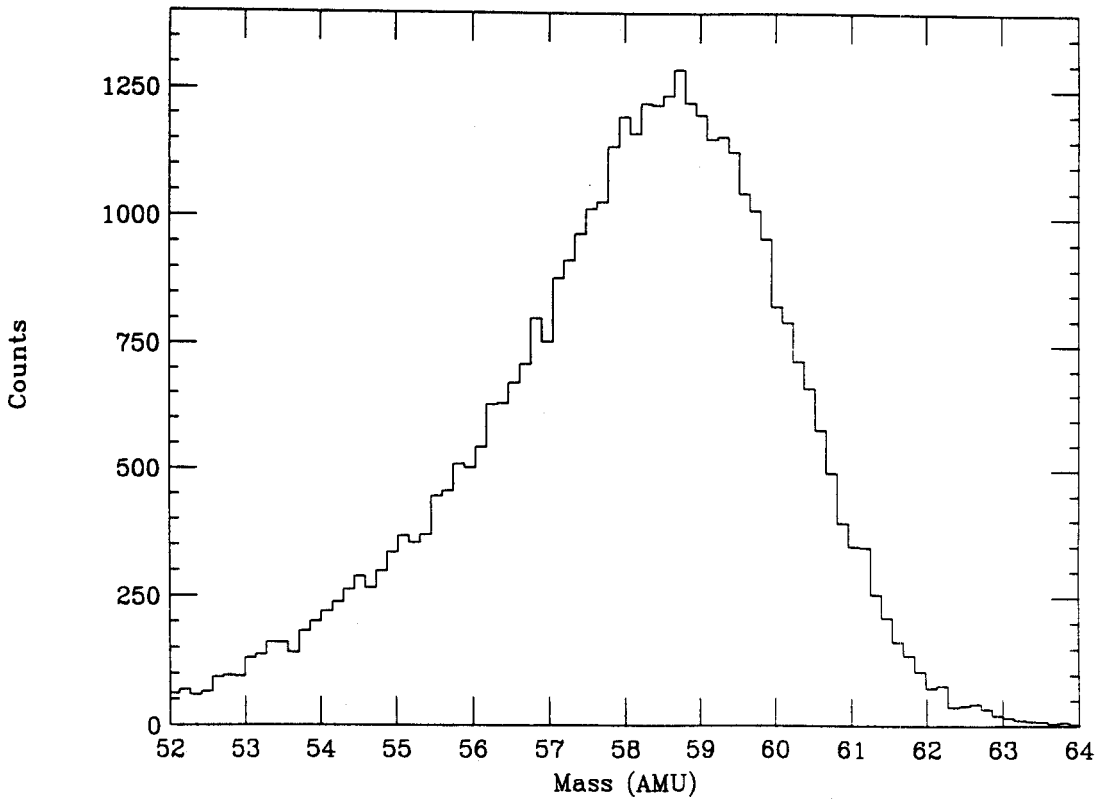

Figure 2.26: Mass of nuclei as calculated using the total energy from the S320 ion chamber.

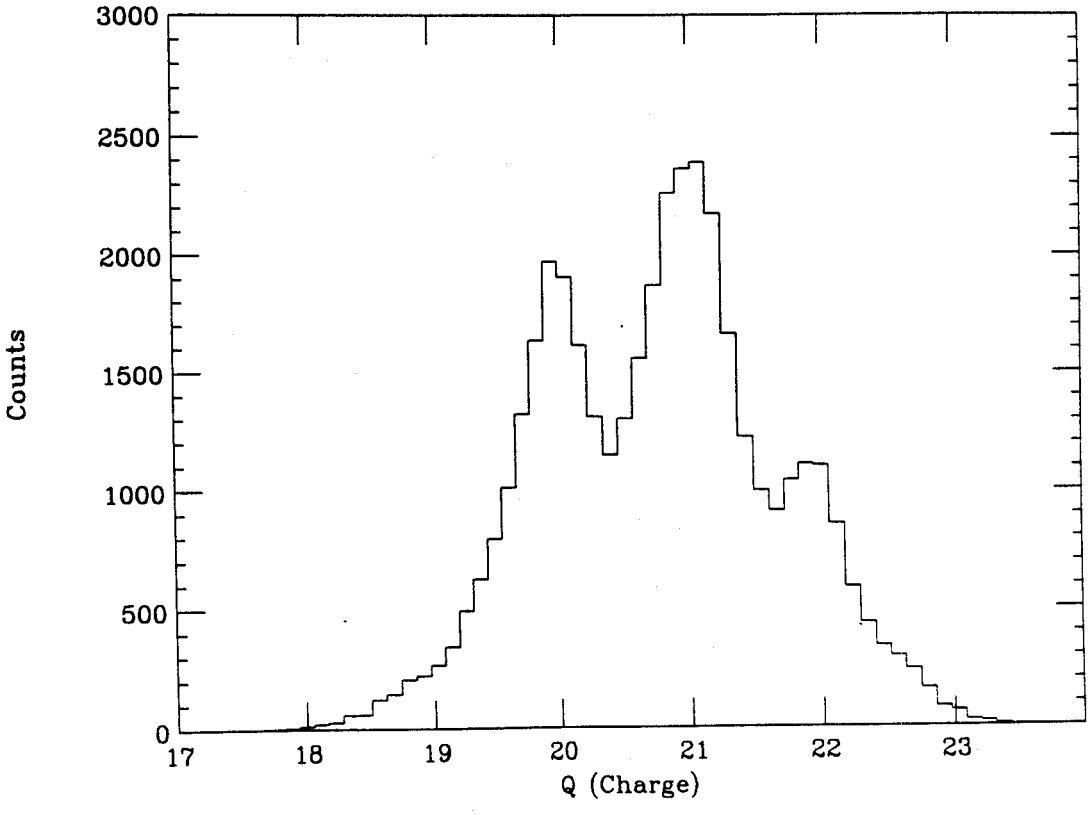

Figure 2.27: Ionic charge spectrum calculated using the masses derived from the S320 ion chamber energy measurement.

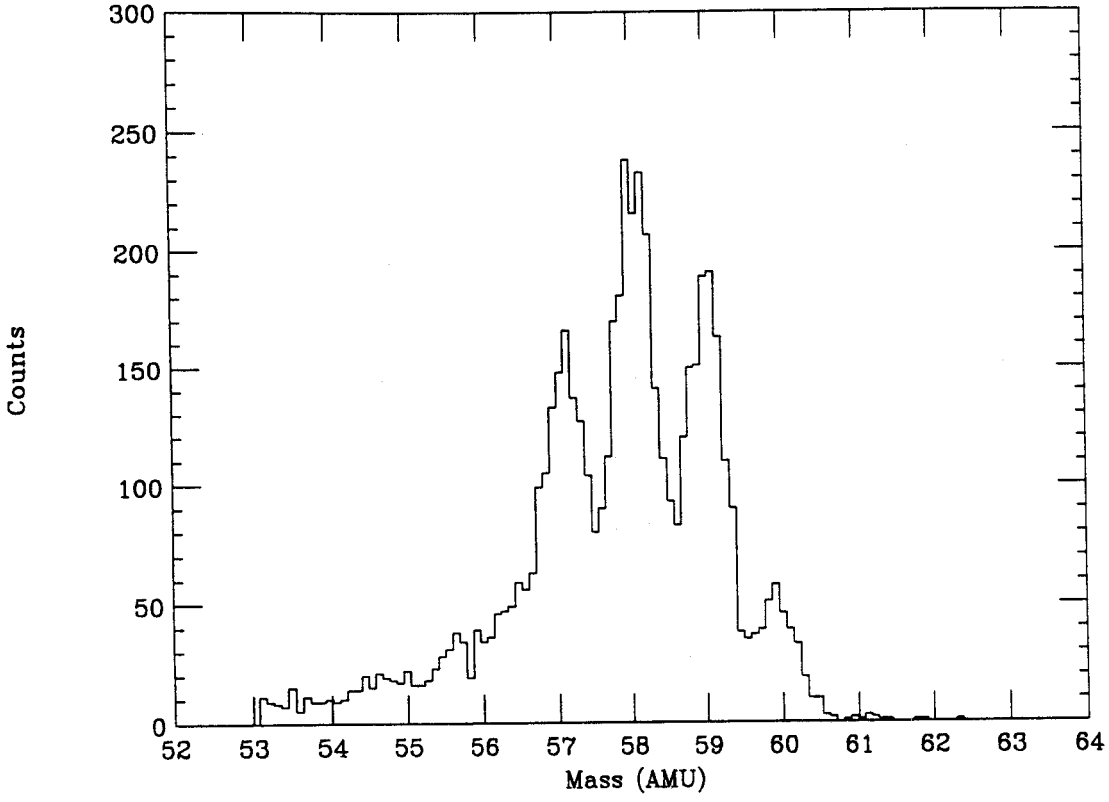

Figure 2.28: Mass spectrum recalculated using the rigidity measurement of the S320, with a selection of q from the ionic charge spectrum.

2.14 is then $E = E_0 - \Delta E$, and therefore the calculated value of q will always be calculated as less than its true value. It is possible to estimate the ΔE using energy loss formulas for a given Z to get an approximate value of E_0. However it is easier to get an estimate of the peak q at a given magnetic field setting by calculating the ionic charge distribution for the mean energy of the element selected[mcm89]. After making this assignment, the masses can be determined as described above. If the resulting mass peaks are spaced one mass unit apart, then the q assignment is correct. If the mass peaks are closer together than one mass unit, the q is still too small. Likewise mass peak spacings greater than one mass unit indicate that the assigned ionic charge is too large. Obviously, this underestimation of the ionic charge can be minimized by reducing the thickness of material before the ion chamber, thus reducing the lost ΔE. However there will only be one solution where the values of mass and ionic charge correspond.

V CONCLUSIONS

The results of the fusion/evaporation data presented in this chapter show that the S320 spectrometer with the permanent magnet dipoles installed may be used to identify the isotopes produced in a compound nucleus reaction, if a focal plane detector with sufficient energy resolution is developed. Clearly the results of this work are limited by the poor energy resolution of the ion chamber detector. The ability to determine both Z and q is diminished enough that no conclusion can be made as to whether the ions of interest – ^{65}As in particular – were produced in the reaction. Ionization detectors have been produced with better than one percent energy resolution by carefully assembling the detector and by taking precautions to purge the detector of any contaminant gas prior to use. With some redesign of the S320 detector configuration and further tests it may provide a viable system for studying slow heavy

ions.

For example, the Breskin detector is not necessary for this experiment. It's job as a timing and position detector can be performed using a thin foil scintillator at the focal plane similar to the start detector, and a windowless wire detector in the first position of the ion chamber volume. The Breskin detector's gas volume window, two field shaping windows, and two cathode windows could be exchanged for a the $100\mu g/cm^2$ plastic scintillator. The windowless wire counter has slightly poorer position resolution than the Breskin detector (0.8mm FWHM compared to 0.7mm FWHM), but there is still sufficient resolution to separate the masses at $A \approx 100$.

A second important improvement be to eliminate as many sources of outgassing in the detector volume as possible. The detector box itself can be redesigned such that cable runs to the outside preamps can be minimized, as the plastic coating of the cables is a major source of contaminant gasses. Also, all screw taps should have small holes drilled at the bottom to allow trapped gasses to be pumped out. Otherwise, each of these tapped holes is a source for a virtual leak of contaminant gasses. Some thought should also be given to the materials used to make the detector, as well as the circuit boards. Various plastics outgas solvents, and excess flux on the circuit boards will contaminate the gas volume. Also, by assembling the detector in a clean environment and baking-out the detector under vacuum prior to use, the problem of electron attachment to contaminant gasses can be further minimized.

Finally, the results of the test runs show that the detector test data cannot simply be extrapolated to various experimental and detector conditions. Care must be taken to test the detector under conditions that accurately simulate the experiment, to document the response of the detector to various gasses, and to have an absolute measure of the ion chamber resolution.

Chapter 3

Isotope Production Using the A1200 Mass Separator

I INTRODUCTION

The identification of new exotic nuclei produced in projectile fragmentation reactions using mass spectrometers has become an important experimental technique. The first successful experiments at relativistic energies by Symons, *et al.*[sym79] and Westfall *et al.*[wes79] at the Lawrence Berkeley Laboratory, have inspired others to attempt similar work at intermediate energies. Experiments using intermediate energy beams and the LISE spectrometer[ann87] at GANIL, the French National Heavy Ion Accelerator Laboratory, have identified new proton-rich[pou87,lan86] and neutron-rich[pou86,gui85,lan85] nuclei. Other new devices include RIPS[ku90], a device similar to LISE built recently at the laboratory RIKEN in Japan, and the Fragment Recoil Separator (FRS)[gei87] in GSI, the German National Laboratory for Heavy Ion Research. The latter device was built to separate and transport relativistic energy beams of radioactive nuclei produced in projectile fragmentation reactions to experimental areas for further study. The FRS is also well suited to identify new nuclei produced in the projectile fragmentation reactions. The recently completed A1200 Mass Separator[sh90] at the National Superconducting Cyclotron Laboratory (NSCL), Michigan State University, is in some

sense a superconducting version of the FRS. The A1200 can separate projectile fragmentation products from intermediate energy reactions and transport them to other experimental areas, or it can be used in a "stand-alone" mode to identify and study the products.

With the availability of such a versatile device as the A1200, it was natural to explore the possibility of producing and studying new exotic nuclei. A good choice for the initial study was to try and produce the nuclei that were not identified in the fusion/evaporation experiment described in chapter 2 – nuclei along the proton-drip line above mass 50. If, for example, ^{65}As and ^{69}Br were bound and could be produced at a reasonable rate, then additional experiments could be designed to measure their halflives and decay properties. The first step was to model the experiment to choose the proper projectile.

The projectile fragmentation reaction mechanism has been described in terms of the abrasion-ablation model[mor78]. In this model, the projectile nucleus and the target nucleus are spheres that cut through each other upon impact (Figure 3.1). Nucleons are removed from the projectile only in the overlap region which can be calculated as a function of impact parameter. The primary distribution of products is thus geometrically calculated and weighted by the probability of the possible impact parameters. No transfer of momentum or nucleons occurs during the collision, and the ratio of neutrons to protons removed is the same as that of the projectile. Each projectile fragment is then assumed to have an excitation energy due to the surface deformation from the removal of nucleons. The deexcitation of the nuclei is calculated using a standard statistical model (as described in the previous chapter), and thus the final distribution of projectile fragments is determined.

All of the features of the projectile fragmentation reaction have been combined into a computer code by Winger[win91a] called INTENSITY, which predicts the ion rates

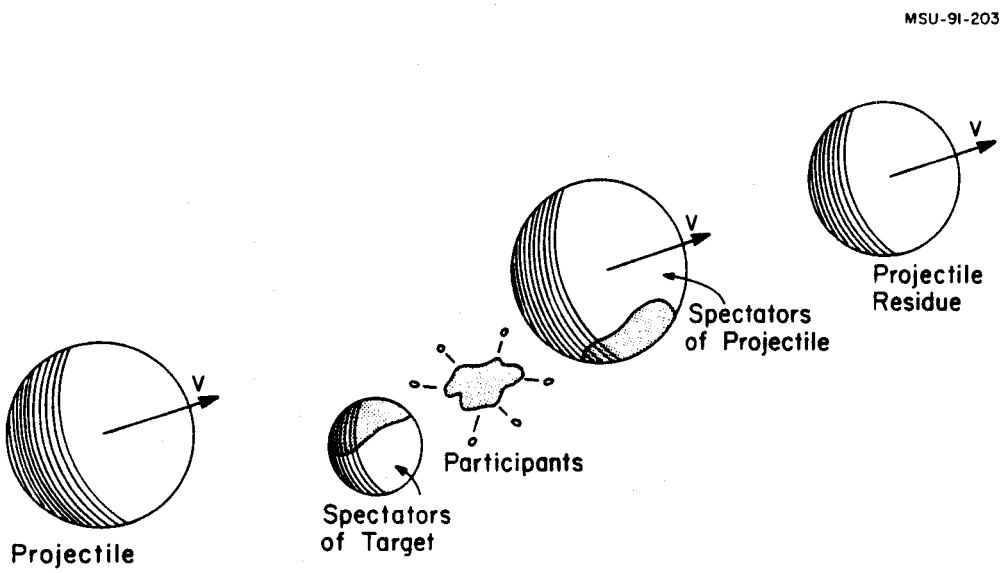

Figure 3.1: Schematic of the projectile fragmentation reaction mechanism.

at the end of a fragment separator. The factors that influence the overall rate can be divided into two groups: the nuclear physical effects, and the atomic physical effects. The nuclear physics is limited to the production cross sections and the momentum distributions. The atomic physics includes energy loss and straggling, ionic charge distributions, and the acceptance of the spectrometer. The nuclear cross sections are taken from the empirical parameterization of Sümmerer and Morrissey[sue90] to predict the nuclei produced in projectile fragmentation reactions. The Goldhaber model[gol74] is then used to determine the momentum and angular phase space distributions of the fragmentation products. An additional width is added to the momentum distribution in the direction transverse to the beam to account for nuclear reaction effects[bib79].

The interaction of the products with the electrons in the target and intermediate detectors in the A1200 must be simulated as well. These processes of energy loss, energy loss straggling, and angular straggling are modeled using the method described by Schmidt, *et al.*[sch87] The distribution of ionic charge states is obtained from a parameterization of known data[win91b], and the products that pass through the magnetic separator is determined using a first order beam optics calculation[gei89].

^{78}Kr proved to be the optimum starting material to produce the beam for the experiment because of its gas phase and availability as an enriched, neutron-deficient, stable isotope. Gas phase materials are easy to use in ion soures, and the isotope enrichment allows reasonable beam currents to be produced. Also, predictions of the resulting products from a ^{78}Kr beam indicate that a number of interesting nuclei can be produced. A beam energy of E/A = 65 MeV was then selected based on the ion source and cyclotron operation limits for producing 0.25 particle-nanoamps of this beam. It should be noted that the Sümmerer and Morrissey parameterization of the cross sections may not be valid at E/A = 65 MeV as the parameterized data were from reactions at higher bombarding energies. For example, the results from the reaction

Table 3.1: Predicted count rates from the INTENSITY code for the fragmentation of E/A = 64.1 MeV ^{78}Kr (0.25 pnA) on a 94 mg/cm^2 ^{58}Ni target (medium acceptance mode). The simulation was optimized for peak production of ^{65}As (B_1 = 0.6762 T, B_2 = 0.6654 T).

Nucleus	Predicted Count Rate (# / sec.)
^{70}Kr	1.9 E−03
^{69}Br	4.1 E−01
^{66}Se	8.6 E−03
^{65}As	7.4 E−01
^{63}Ge	8.6 E−01
^{62}Ge	1.4 E−02
^{61}Ga	1.0 E+00

of E/A = 44 MeV ^{86}Kr[ba90] at the LISE spectrometer indicate that the projectile fragmentation predictions do not reproduce the data at these energies. However, given that there is such limited data for intermediate energy heavy ion reactions, the Sümmerer and Morrissey parameterization was used to calculate the count rates shown in Table 3.1.

II Experiment and Results

The experiment was performed using a beam from the NSCL K1200 Cyclotron at Michigan State University. The reaction occurred at the medium acceptance target position of the A1200 Mass Separator[sh90] and the reaction products were transported to the achromatic focal point of the device where the isotopes were identified. Figure 3.2 shows a schematic layout of the A1200. The device consists of a series of fourteen superconducting quadrupoles and four superconducting dipoles. It has an angular acceptance of 0.8 msr, a 3% momentum acceptance, and a maximum rigid-

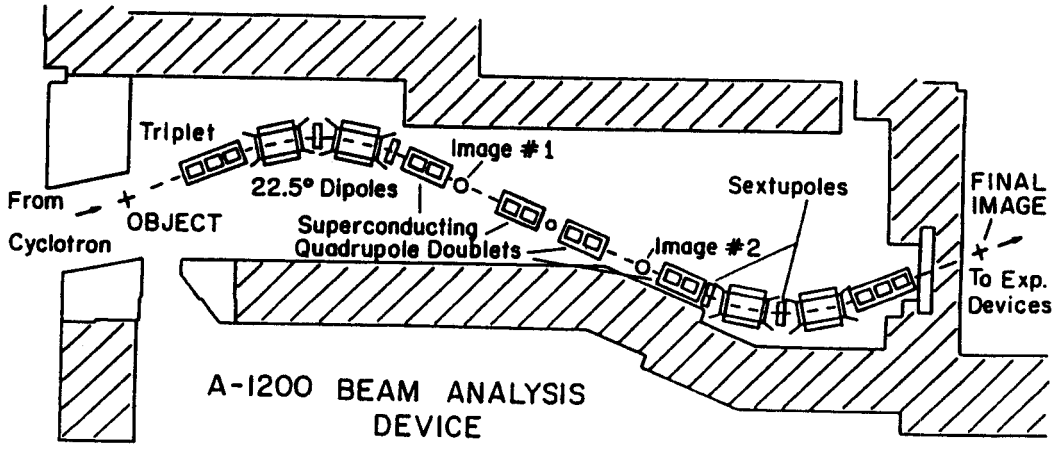

Figure 3.2: Schematic layout of the A1200 beam-analysis device.

ity of 5.4 T-m. The method used to identify the isotopes produced in the present study was similar to that used by Bazin,*et al.*[ba90], with the addition of a precise rigidity measurement. Note that this isotope identification method is similar to the method outlined in chapter two, in which the ΔE, E_{TOTAL}, time-of-flight, and rigidity measurements are combined to give complete and unambiguous isotope identification.

The E/A = 64.1 MeV ^{78}Kr beam bombarded a 99.98% enriched ^{58}Ni target, 94 mg/cm^2 thick, at the object point of the A1200. The ^{58}Ni target was chosen based on previous work at GANIL[mue90], in which an enhancement for proton-rich projectile-like nuclei was found using proton-rich targets. The reaction products were collected by and transported through the A1200 Mass Separator. At the first dispersive focus, labeled image #1 in Figure 3.1, a plastic scintillator detector was used to produce a reference time signal for the ions. An 8 mg/cm^2 (3 mil) Bicron BC404 scintillating foil was mounted on a plastic light guide which was glued to the face of a two-inch RCA RC232 photomultiplier tube. The time difference between the signal from this start detector and the time signal from the first silicon detector at the final image was used to calculate the velocity of each particle over the 14.044(3) meter flight path. The horizontal position of the particle at the second intermediate dispersive focal plane, labeled image #2 in the figure, was measured with a position sensitive parallel plate avalanche detector. This was combined with an NMR measurement of the dipole fields to calculate the rigidity of the products. A four-element silicon detector telescope (ΔE1, ΔE2, E1, and E2) positioned at the final achromatic image point of the A1200, provided energy loss and total energy measurements needed to identify the reaction products. The ΔE detectors were totally depleted ion-implanted silicon detectors, 300 microns thick with an active area of 450 mm^2. The E detectors were surface barrier silicon detectors one millimeter thick with an active area of 300 mm^2. The detectors were cooled to -10°C using a methanol refridgerator and a

special cooling mount (Figure 3.3). The cooling reduced the thermal noise in the detectors, and thus improved the signal-to-noise ratios of the ΔE and E signals. A collimator was placed at the front of the detector mount to limit the detection area to slightly less than 300 mm^2.

A schematic diagram of the electronic modules for the experiment is shown in Figure 3.4. Nineteen signals were read by the front end computer for each triggered event: ADC and TDC signals for each silicon detector (8); ADC and TDC signals for the left, right, up, and down readouts of the PPAC position wires (8); a charge-sensing ADC (QDC) and a TDC signal for the start detector scintillator (2); and an ADC signal from the TAC measuring the flight time from the start detector to the ΔE1 detector (1). The data acquisition once again relied on the standard NSCL hardware and software systems[fox89]. The event trigger was produced by requiring a coincidence between signals in the two ΔE detectors and the not-busy signal from the front end computer. The TDC's and the TAC were operated in common-start mode. As discussed in chapter 2, the time differences obtained from these measurements are really a difference between the flight-time and some delay. Some of the time signals, *i.e.,* the PPAC TDC's, were mostly diagnostic and were monitored simply to make sure that the detectors were behaving properly.

The the detection system was calibrated by transporting the direct beam through the device. A thin (5 mg/cm^2) aluminum target was used to strip the electrons from the primary beam and produced charge states that were identified by the system at different field settings. This information was used to calibrate rigidity versus position at image #2. Knowing the mass (m), charge (q), dipole field (B), and incident energy of the ^{78}Kr ions, the bend radius (ρ) corresponding to the position of each set of the

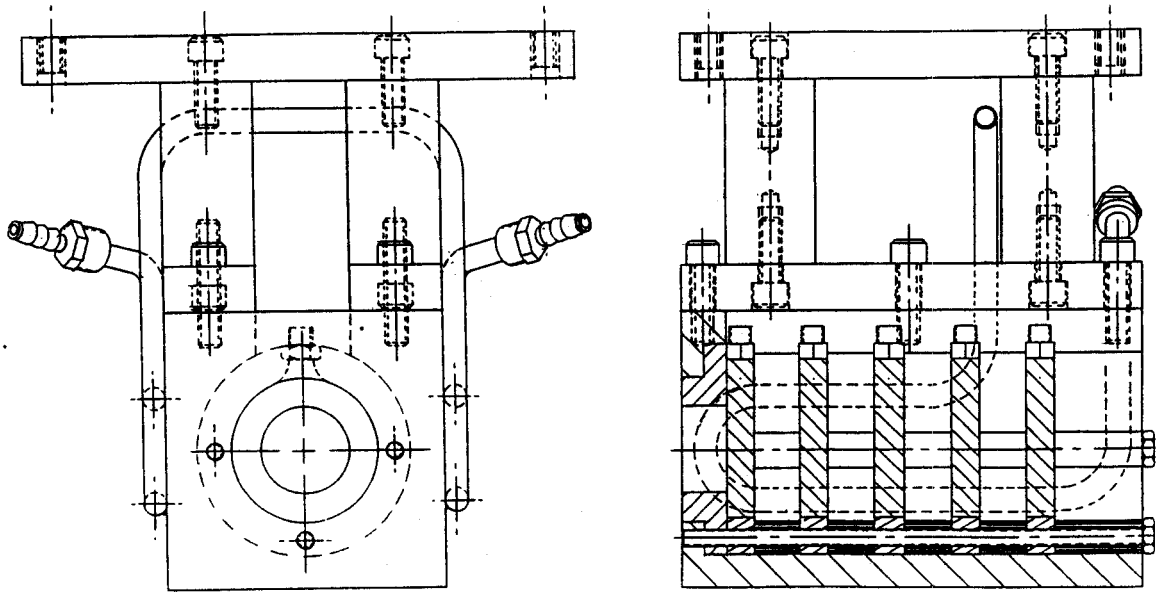

Figure 3.3: Cooling mount for the silicon detector telescope at the achromatic image of the A1200.

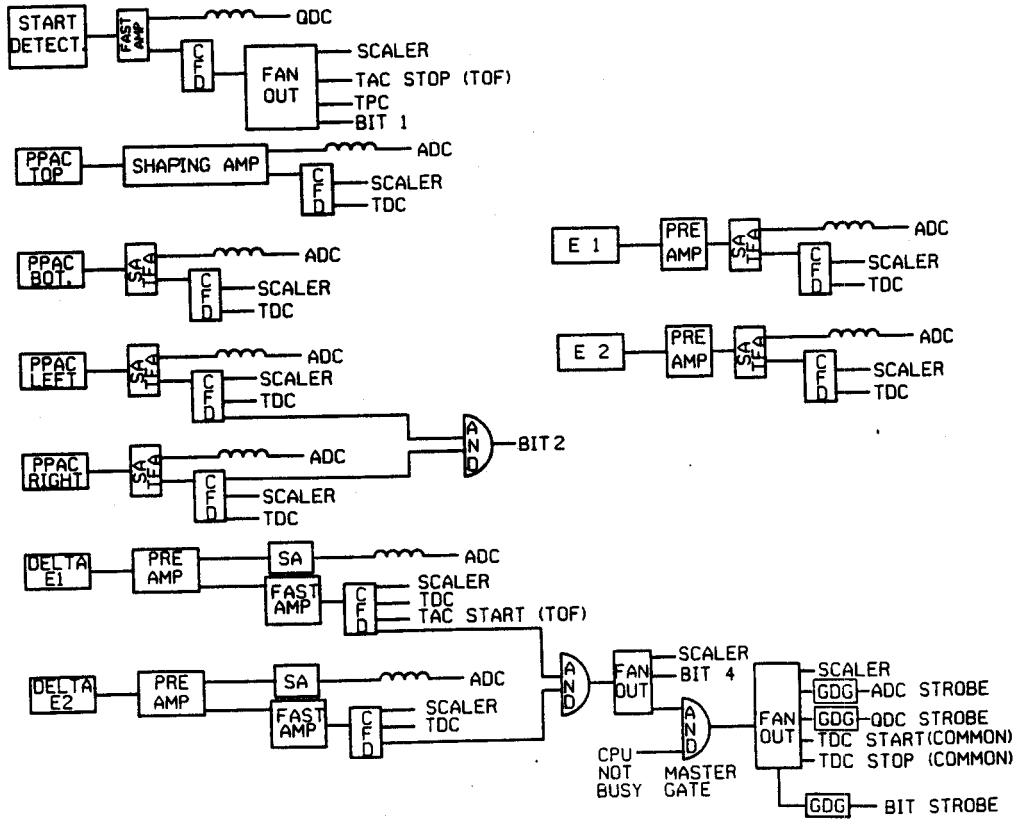

Figure 3.4: Electronics diagram for the A1200 isotope identification experiment.

particles was calculated from the relativistic form of the rigidity:

$$B\rho = \frac{m\beta\gamma}{q}, \tag{3.1}$$

in which

$$\beta = \frac{v}{c} \tag{3.2}$$

and

$$\gamma = \frac{1}{\sqrt{1-\beta^2}}. \tag{3.3}$$

The bend radius was expanded in terms of the detector position as shown in Equation 2.4. A quadratic form was used to obtain the fit shown in Figure 3.5.

The flight time was calibrated by removing the target and setting the magnets in the A1200 so the beam would travel along central trajectory of the device (where the path length is known most accurately). Since the beam energy, and hence its flight time, are known, the arbitrary delay times can be determined and the time-of-flight calibrated. Figure 3.6 shows a schematic diagram of the TDC system for this measurement. The TDC gets a common start from the master gate (MG). The start detector and ΔE1 signals arrive at some later time to stop the TDC timers, and are converted to numbers that are read by the computer. From Figure 3.6 it is clear that these values can be expressed as:

$$t_{\Delta E1} = t_{\Delta E1\ \mathrm{DELAY}} - t_{\mathrm{MG}} \tag{3.4}$$

$$t_{\mathrm{START}} = t_{\mathrm{START\ DELAY}} - t_{\mathrm{FLIGHT}} - t_{\mathrm{MG}} \tag{3.5}$$

In these equations the delay times are the cable delays illustrated in the figure, t_{MG} is the time necessary to create the master gate used as the common start, and t_{FLIGHT} is the flight time through the spectrometer of the particle. The difference between the two TDC times is then:

$$t_{\Delta E1} - t_{\mathrm{START}} = t_{\Delta E1\ \mathrm{DELAY}} - t_{\mathrm{MG}} - t_{\mathrm{START\ DELAY}} + t_{\mathrm{FLIGHT}} + t_{\mathrm{MG}} \tag{3.6}$$

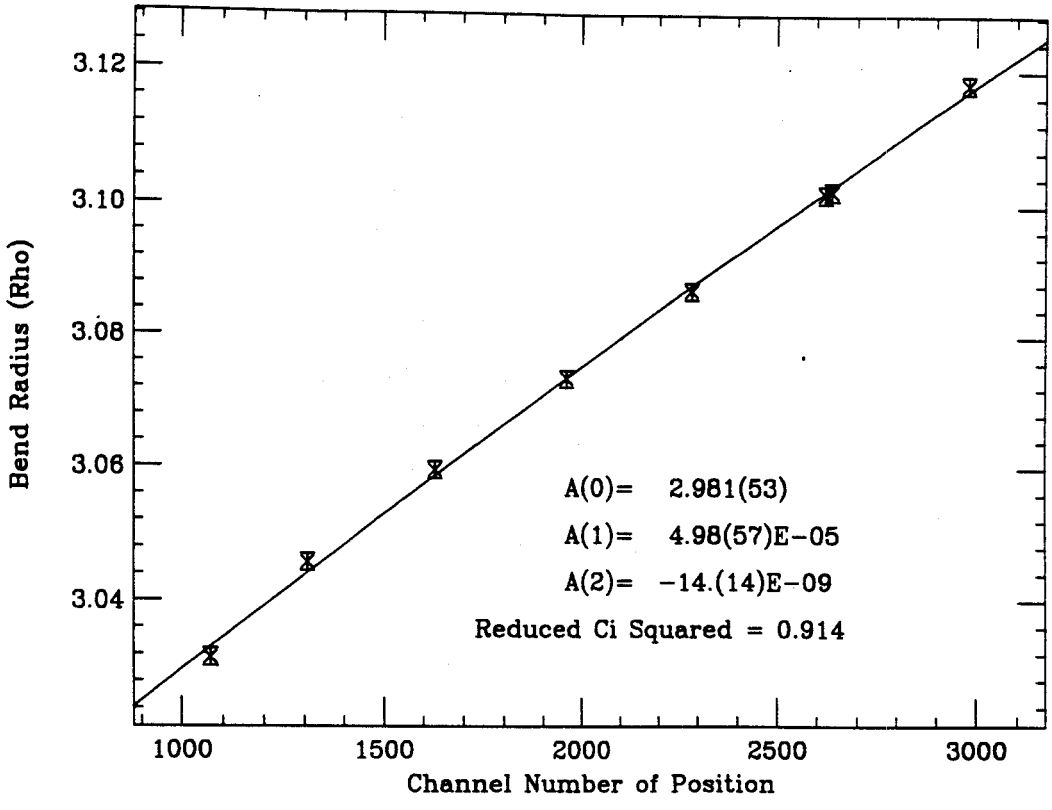

Figure 3.5: Bend radius calibration for the intermediate dispersive image #2 of the A1200.

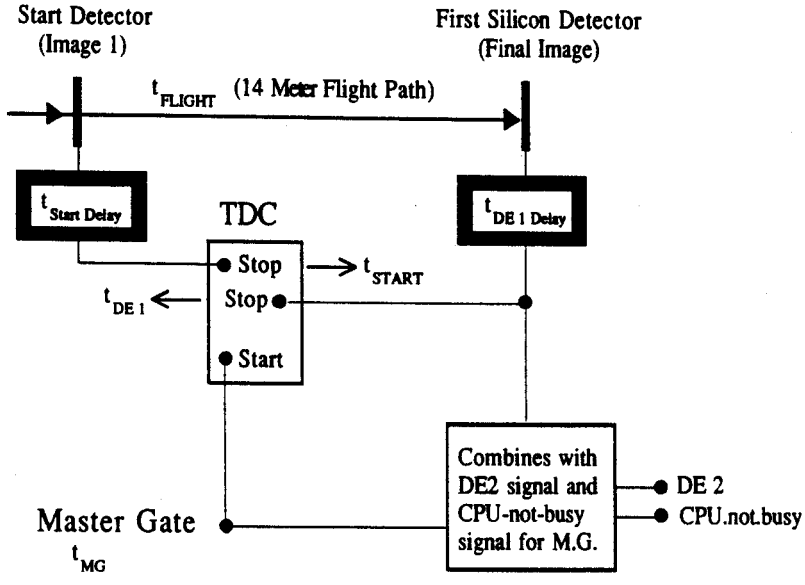

Figure 3.6: Schematic of electronics for Time-to Digital Converters to illustrate TDC time of flight calculation.

$$= t_{\Delta E1\ \mathrm{DELAY}} - t_{\mathrm{START\ DELAY}} + t_{\mathrm{FLIGHT}} \quad (3.7)$$

Notice that regardless of the order of subtraction the term involving the master gate time is subtracted out, thus removing any time fluctuations in the logic electronics. The remaining delay times are essentially due to cable delay times, and are constant values. Equation 3.7 can then be solved for the flight time to give:

$$t_{\mathrm{FLIGHT}} = t_{\Delta E1} - t_{\mathrm{START}} + t_{\mathrm{START\ DELAY}} - t_{\Delta E1\ \mathrm{DELAY}} \quad (3.8)$$

$$= t_{\Delta E1} - t_{\mathrm{START}} + CONSTANT \quad (3.9)$$

Since the flight time for beam particles is known and their TDC times can be measured, equation 3.9 can be solved for the constant representing the difference in cable delays and the time of flight can be calibrated for the reaction products.

The energy loss calibration and isotope identification were obtained by setting the A1200 to detect light nuclei produced in this reaction. The isotopes were initially displayed in a spectrum of relative energy loss versus time-of-flight. As discussed previously, such a spectrum separates by element (Z), and the added selection in momentum by the A1200 (three percent or less) enabled the individual isotopes to be resolved in this spectrum. The isotopes were unambiguously identified by observing the absence of unbound or extremely short lived nuclei. For example, the ΔE1 versus time-of-flight spectrum of the light products (Figure 3.7) has a blank space at the position of ^{16}F. Then by collecting data at overlapping rigidity settings, a continuous isotope spectrum was obtained which permitted unambiguous identification of the heavy reaction products.

Figures 3.8 and 3.9 show the ΔE1 and ΔE2 versus time-of-flight isotope spectra for the region of interest. The two ΔE measurements provide a redundant isotope identification. Sixteen isotopes from various regions of these spectra were chosen with software gating as calibration nuclei. Each selected nucleus was then projected in a

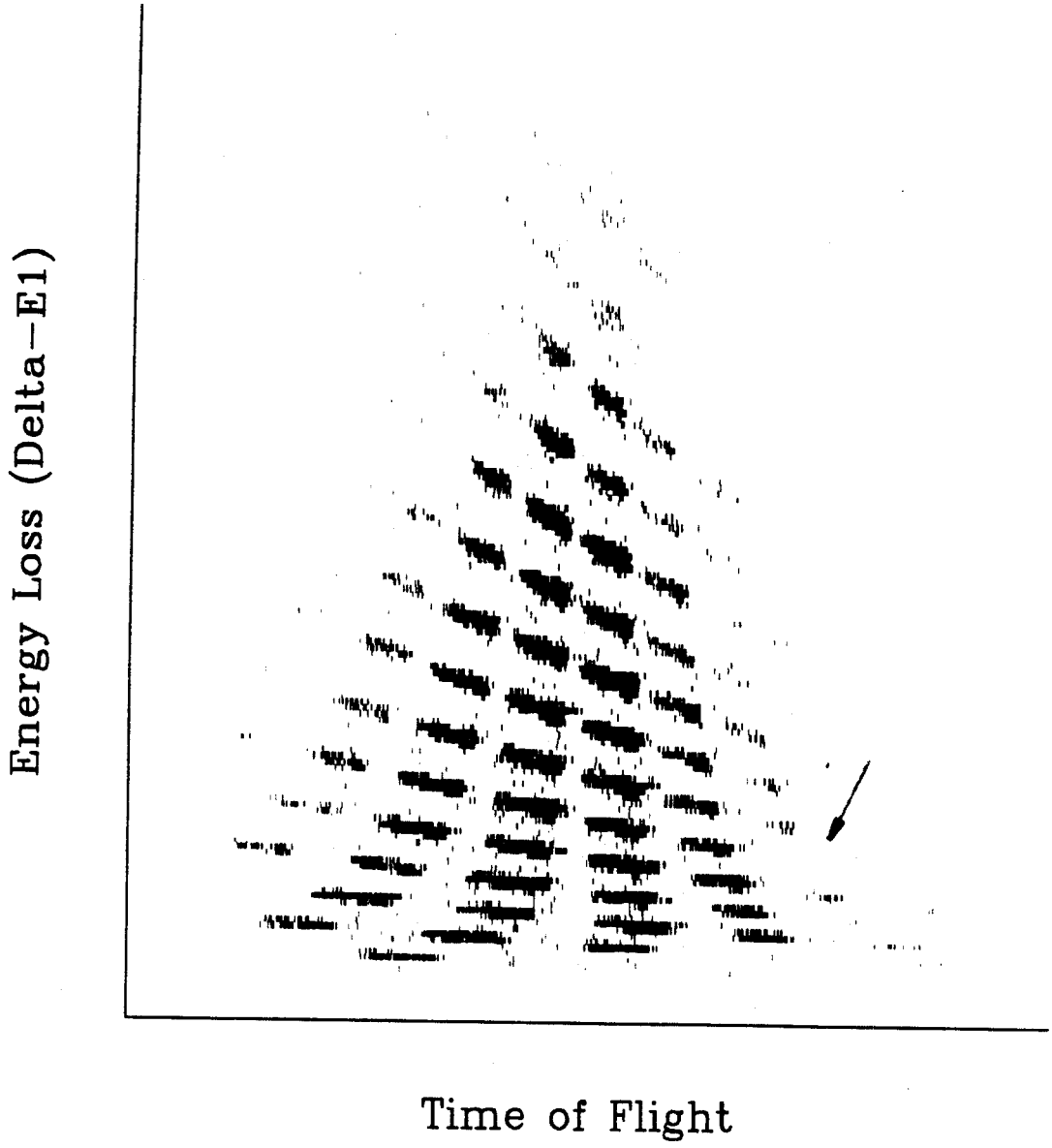

Figure 3.7: Energy loss versus time of flight for the light isotopes. A space at the position of ^{16}F is indicated.

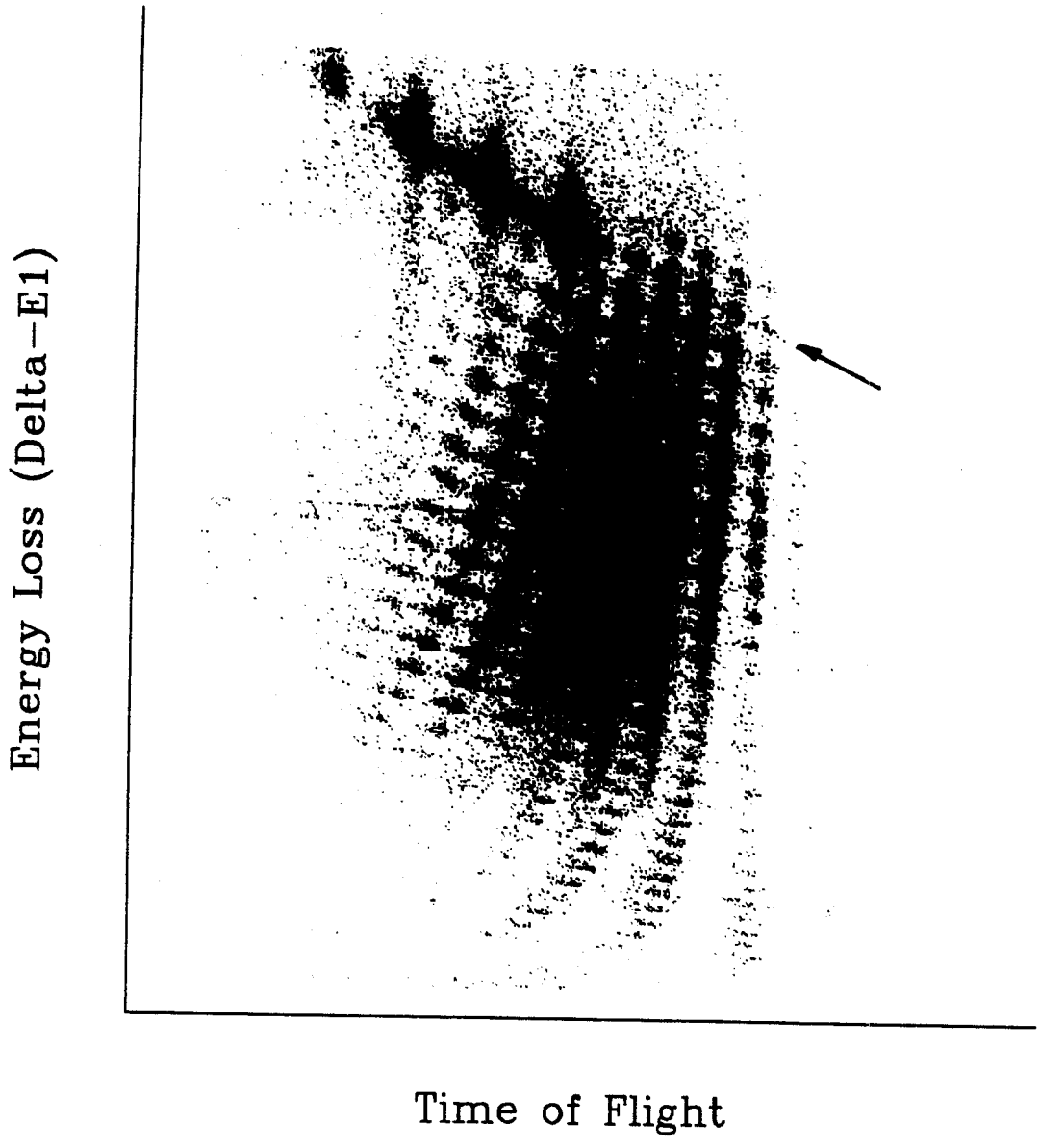

Figure 3.8: ΔE1 versus time of flight for the region of interest.

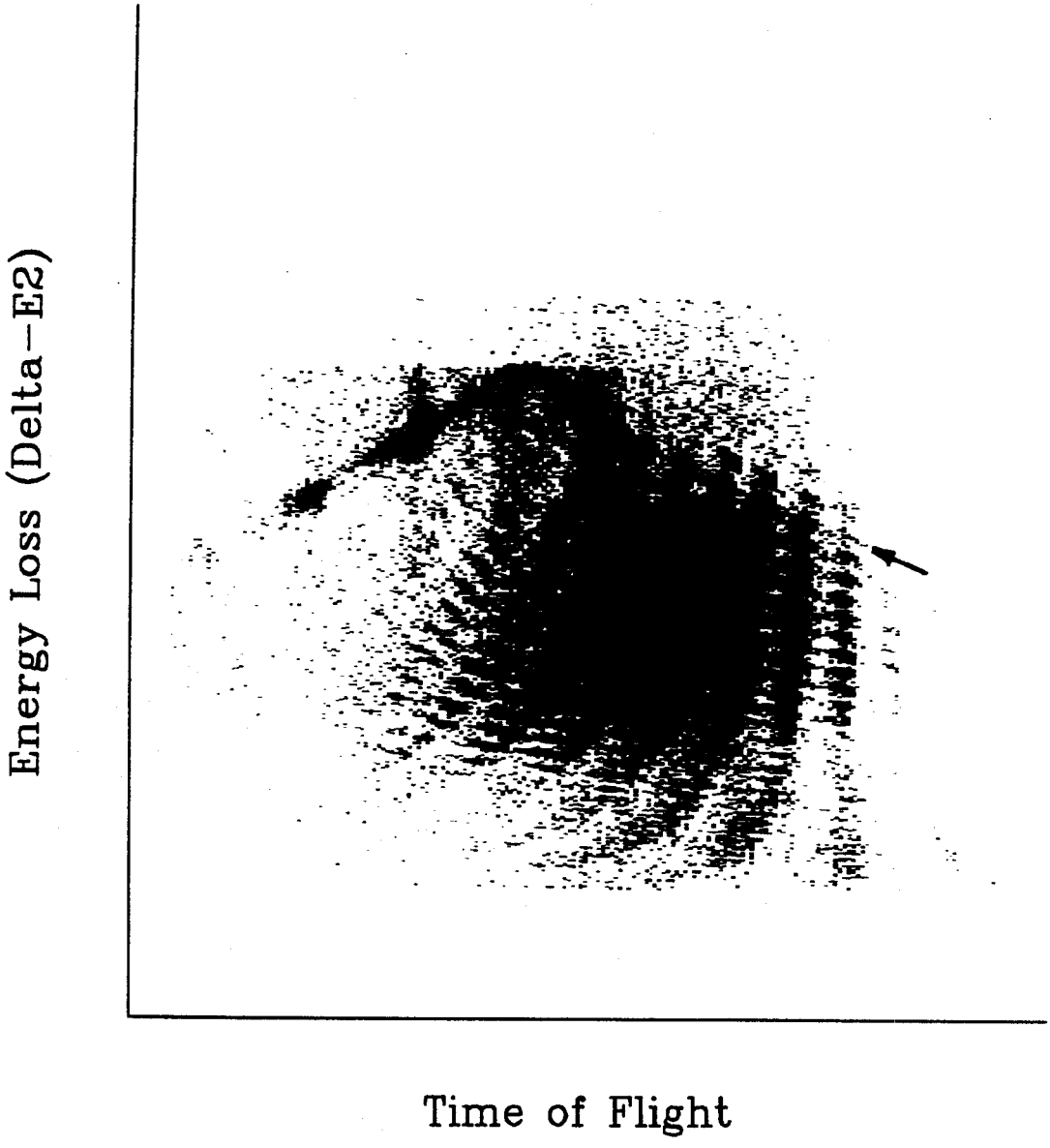

Figure 3.9: ΔE2 versus time of flight for the region of interest.

time- of-flight versus image #2 position spectrum, as shown for ^{62}Cu in Figure 3.10. Contamination in the ΔE1 versus time-of-flight gate due to neighboring isotopes was easily distinguished in this spectrum, and a software condition was placed to chose only the isotope of interest, as shown in the figure. Then, a 0.5% selection of the A1200 central rigidity was used to reduce the the spread in time and energy of the calibration isotopes. Using these software conditions, the energy spectra from the silicon detectors and the time-of-flight spectra were created for the isotopes. A representative set of spectra for ^{62}Cu is shown in Figure 3.11.

The flight times of the calibration nuclei were calculated from the equation:

$$t_{\mathrm{FLIGHT}} = \frac{\ell}{c}\left[\left(\frac{3.10711 \cdot A}{qB\rho}\right)^2 + 1\right]^{\frac{1}{2}}, \tag{3.10}$$

where ℓ is the path length between the time measuring detectors. This expression can be derived by substituting the simple expression:

$$v = \frac{\ell}{t_{\mathrm{FLIGHT}}} \tag{3.11}$$

into equation 3.1 and solving for t_{FLIGHT}. Values of the flight time in nanoseconds were plotted against the difference in channel numbers between the cetroids of the ΔE1 TDC signal and the start detector TDC signal. In the linear function that results, shown in Figure 3.12, the slope corresponds to the conversion from channels to nanoseconds in the TDC's, and the intercept is the delay time constant from equation 3.9. These values of the slope and intercept should be the same as those derived from the beam calibration (as was the case in this work).

The energy deposited in each silicon detector was calculated using the formalism of Hubert, *et al.*[hu89] It was assumed that the beam would lose energy through half of the target, the reaction would take place at the center, and the reaction products would lose energy through the second half of the target. The products would then lose

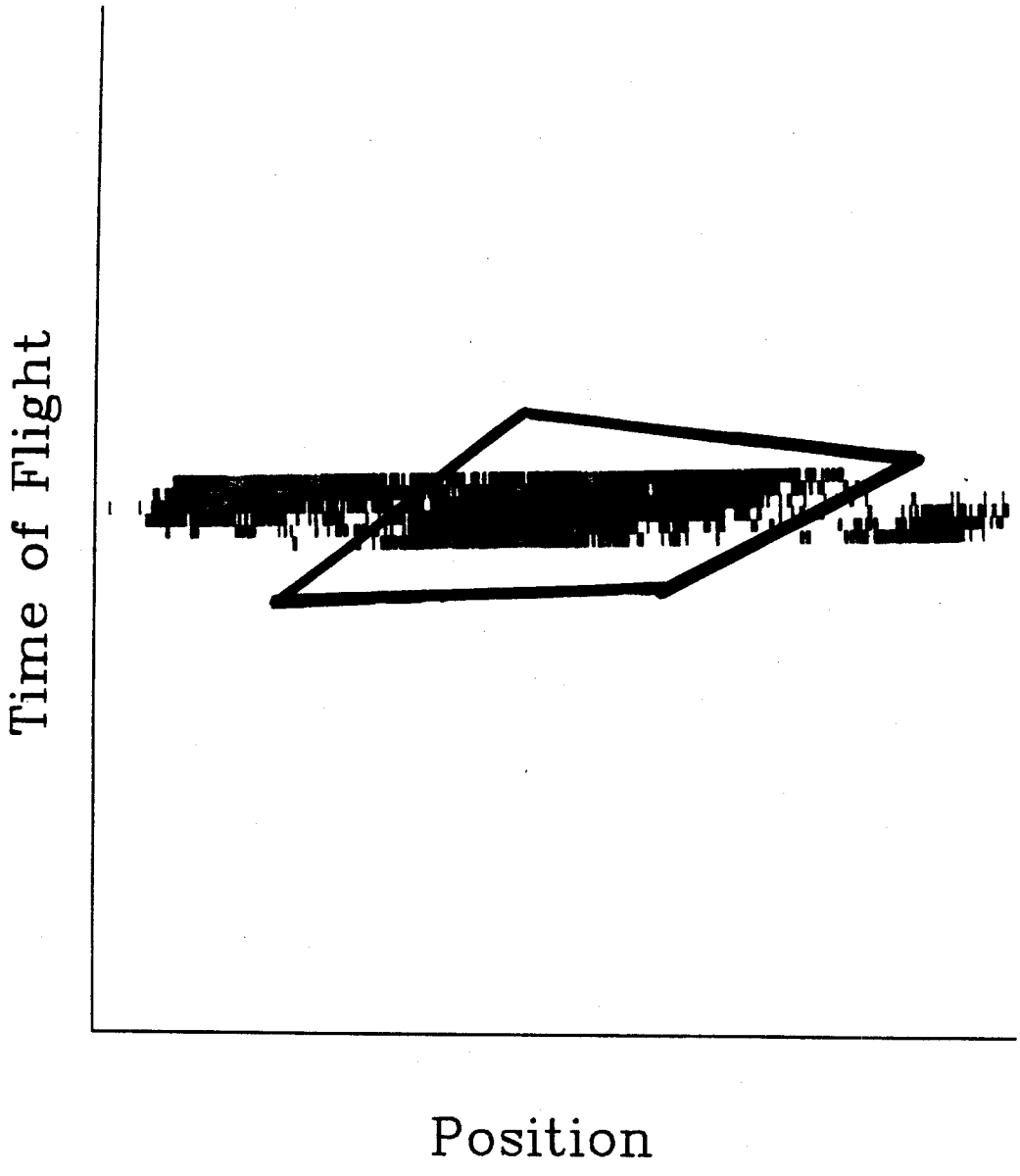

Figure 3.10: Time of flight versus image # 2 position for ^{62}Cu.

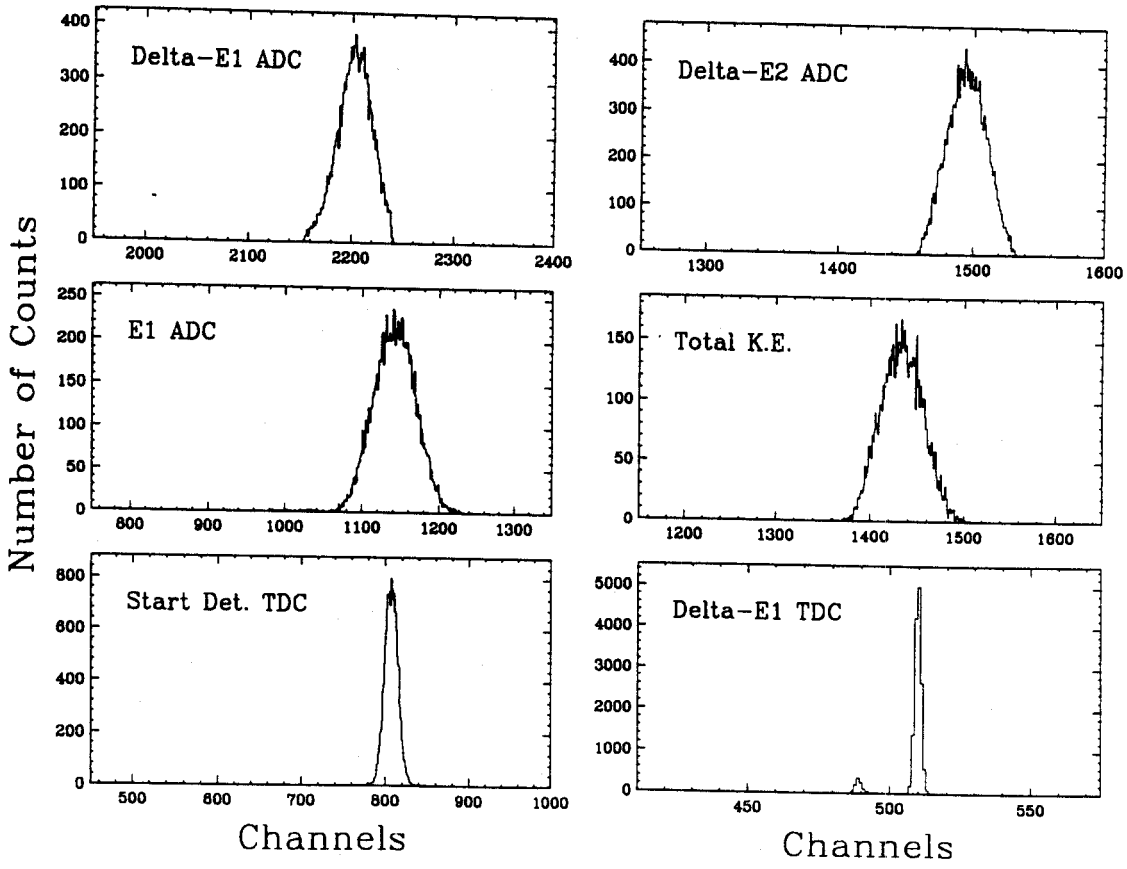

Figure 3.11: A representative set of calibration spectra for ^{62}Cu.

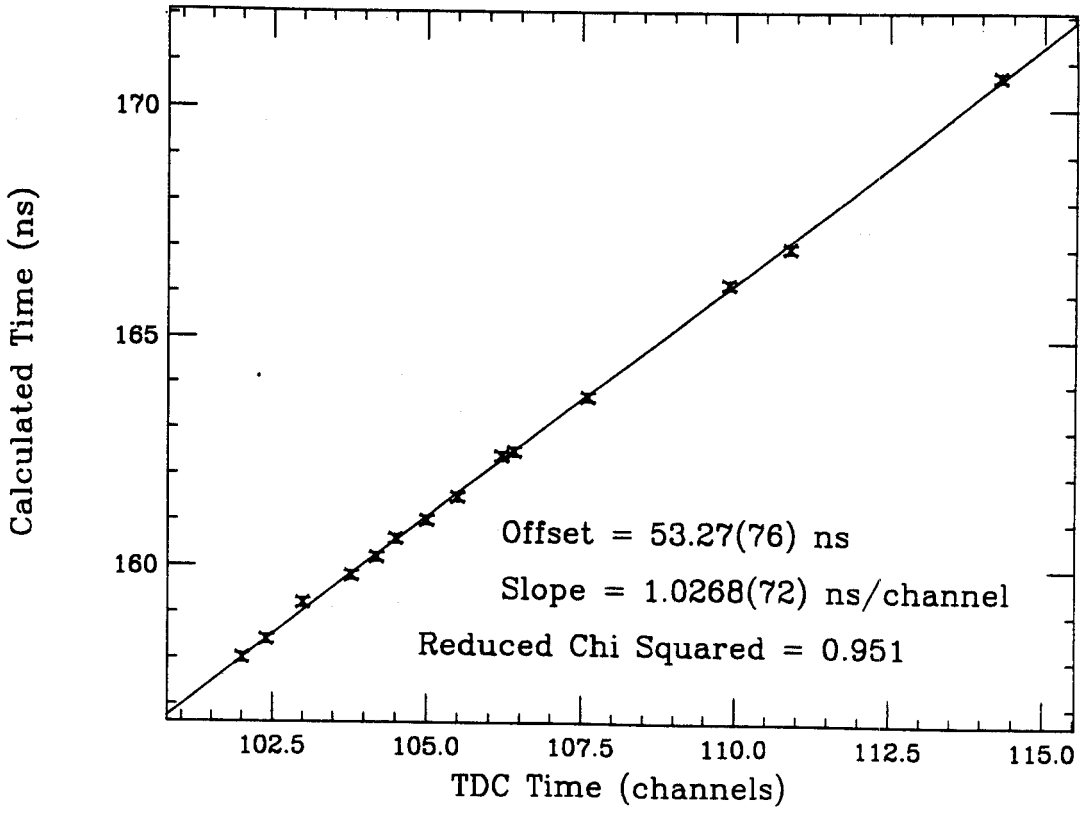

Figure 3.12: Time of flight calibration fit.

Table 3.2: Data and calculated values of energy losses in ΔE1, ΔE2, and E1 for each of the sixteen calibration isotopes selected.

Nuclei	ΔE1 Peak (chan)	ΔE1 Energy (MeV)	ΔE2 Peak (chan)	ΔE2 Energy (MeV)	E1 Peak (chan)	E1 Energy (MeV)
^{29}Si	516.	156.70(25)	316.	179.70(56)	1208.	918(50)
^{34}S	689.	213.90(35)	425.	253.50(79)	1232.	931(51)
^{47}Sc	1269.	402.80(65)	827.	530.8(17)	1116.	813(44)
^{50}V	1442.	460.40(75)	939.	608.2(19)	1230.	900.(49)
^{53}Mn	1632.	521.50(85)	1058.	691.5(22)	1336.	978(53)
^{59}Co	1989.	638.2(10)	1354.	907.9(28)	1068.	753(41)
^{62}Cu	2203.	708.8(12)	1494.	1011.6(32)	1140.	801(44)
^{67}Ge	2571.	830.8(14)	1754.	1208.4(38)	1172.	799(43)
^{70}As	2780.	901.0(15)	1948.	1367.7(43)	1007.	622(34)
^{72}Br	2958.	961.3(16)	2036.	1427.5(44)	1179.	768(42)
^{75}Kr	3179.	1036.0(17)	2252.	1608.3(50)	989.	564(31)
^{59}Ni	2012.	646.0(10)	1333.	889.1(27)	1293.	934(51)
^{63}Zn	2284.	735.8(12)	1535.	1040.0(32)	1240.	878(48)
^{56}Co	1827.	586.10(95)	1184.	780.8(24)	1432.	1050(57)
^{66}Ge	2508.	810.9(13)	1682.	1152.1(36)	1306.	917(50)
^{71}Se	2868.	930.9(15)	1992.	1396.7(44)	1093.	696(38)

energy in the start detector, the image #2 PPAC, and finally come to rest and deposit their remaining energy in the silicon telescope. The calculated values of the energy loss in each detector were plotted against the channel number of the signals from each isotope and fitted with a line to obtain a calibration of energy versus channel number. The slope, of course, gives this value and the intercept represents any small zero offset that may be present in the ADC's. These fits are shown in Figure 3.13, and the data used to produce the fits are given in Tables 3.2 and 3.3. Since the ions of interest in this work stop in the E1 detector, the E2 detector calibration was performed with the lighter isotopes isotopes from the A1200 settings corresponding to Figure 3.7.

The element (Z) resolution was obtained from the ΔE1 and ΔE2 versus total energy spectra shown in Figures 3.14 and 3.15. The specific value of Z was calibrated

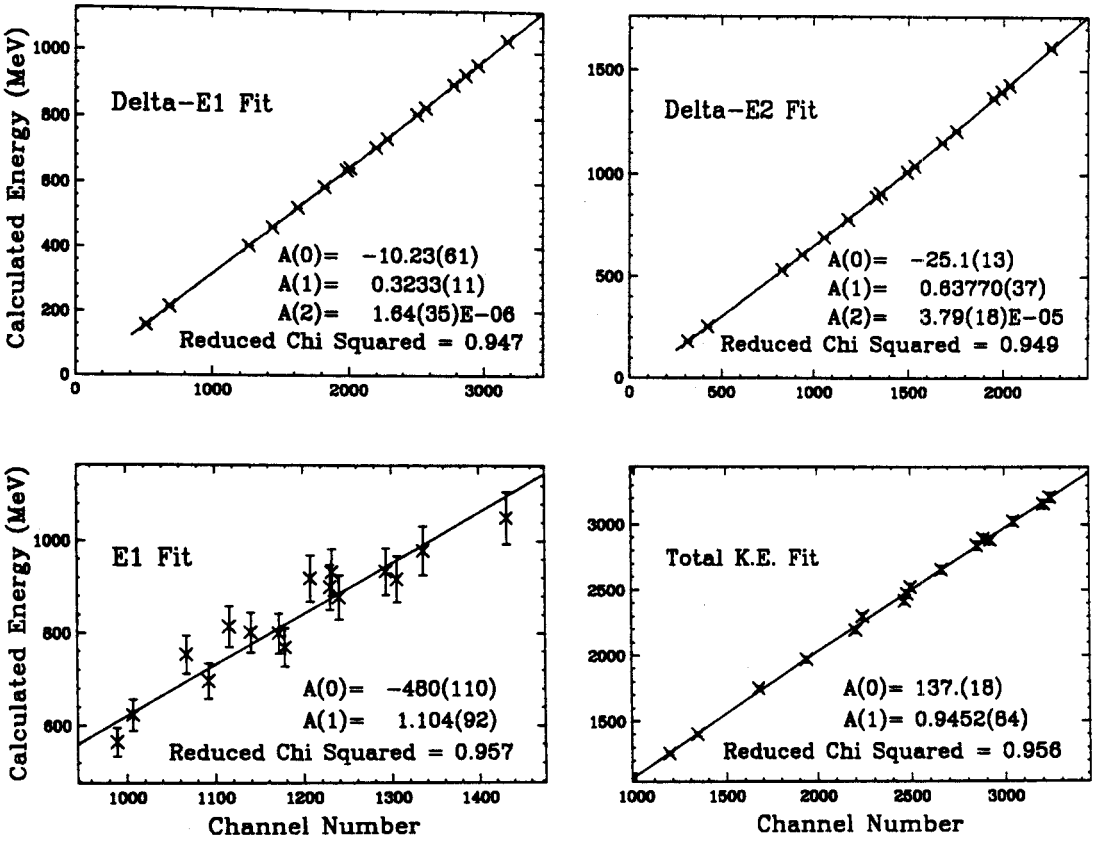

Figure 3.13: Silicon detector calibration fits.

Table 3.3: Data and calculated values of Total Kinetic Energy (TKE) and time of flight for each of the sixteen calibration isotopes selected.

Nuclei	TKE Peak (chan)	TKE Energy (MeV)	TDC Peak (chan)	TDC Time (ns)
^{29}Si	1185.	1255(13)	N/A	N/A
^{34}S	1342.	1399(15)	N/A	N/A
^{47}Sc	1678.	1748(18)	114.3	170.70(9)
^{50}V	1940.	1968(21)	109.9	166.20(9)
^{53}Mn	2203.	2191(23)	106.2	162.40(9)
^{59}Co	2241.	2299(24)	110.9	167.00(9)
^{62}Cu	2498.	2522(26)	107.6	163.70(9)
^{67}Ge	2850.	2838(30)	104.5	160.60(9)
^{70}As	2884.	2891(30)	106.4	162.50(9)
^{72}Br	3210.	3158(33)	102.0	158.00(9)
^{75}Kr	3244.	3208(34)	103.8	159.80(9)
^{59}Ni	2479.	2469(26)	105.5	161.50(9)
^{63}Zn	2664.	2654(28)	105.0	161.00(9)
^{56}Co	2465.	2417(25)	103.0	159.20(9)
^{66}Ge	2923.	2880(30)	102.4	158.40(9)
^{71}Se	3046.	3024(32)	104.2	160.20(9)

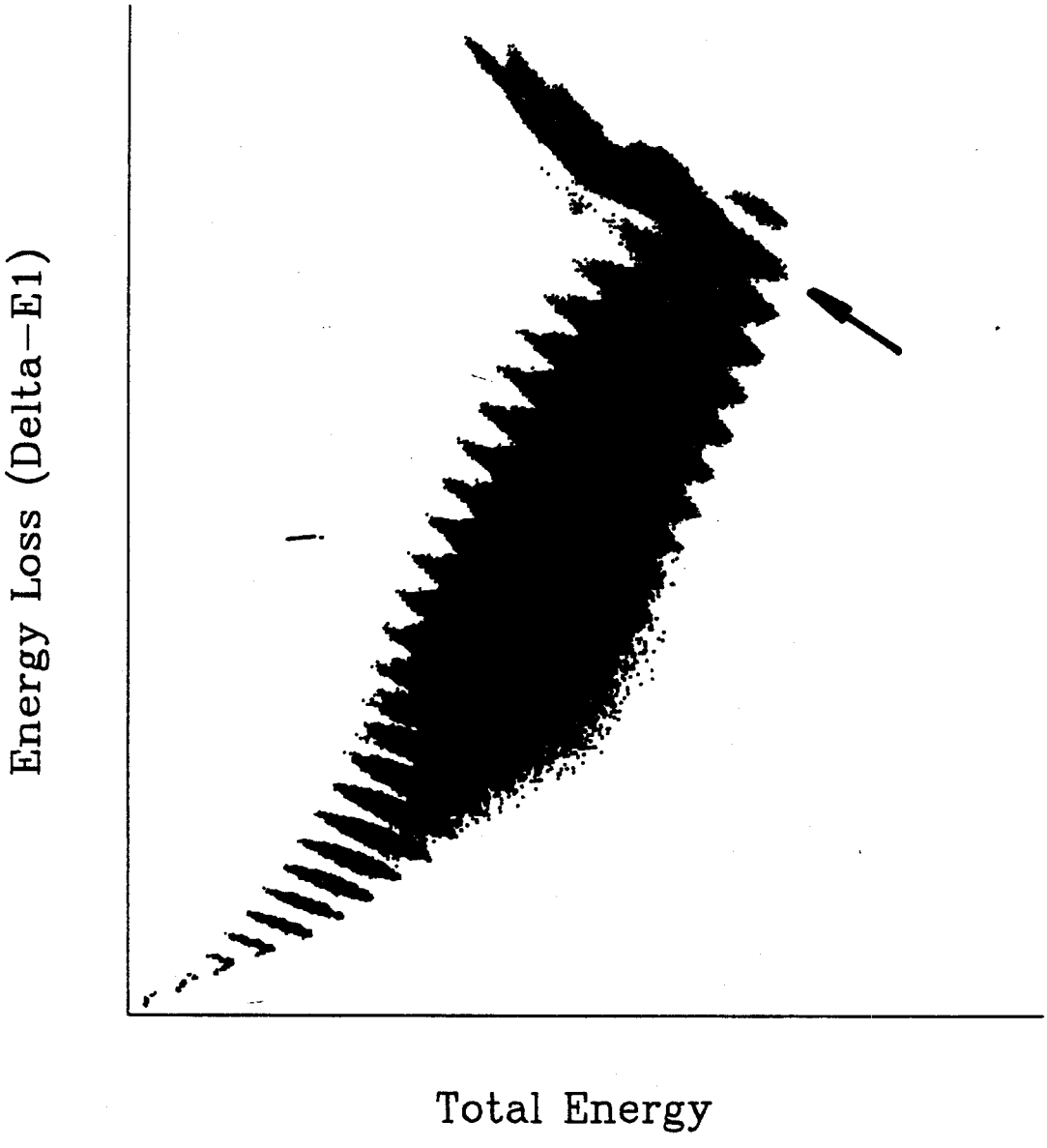

Figure 3.14: Z spectrum from ΔE1 versus total energy.

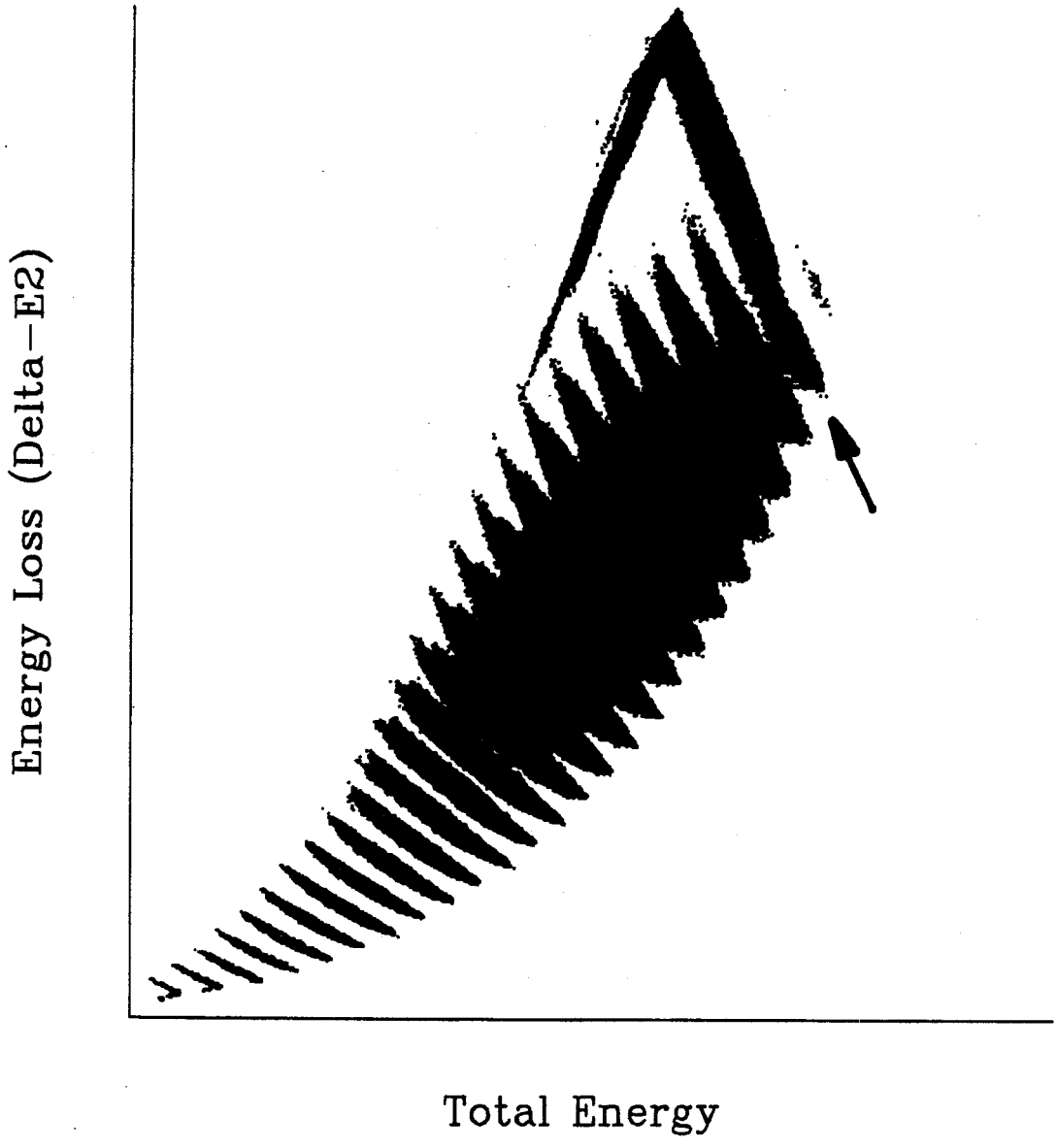

Figure 3.15: Z spectrum from ΔE2 versus total energy.

in two ways: initially, by gating on a known Z group in the ΔE versus time-of-flight spectrum and producing the corresponding group in the ΔE versus total energy spectrum. In addition, scattered beam that enters the detector and lower ionic charge states of the beam reach the final image and appear in the Z spectrum in the Z=36 band, as indicated in Figures 3.14 and 3.15.

The masses of the isotopes of a given Z were calculated with the same method described in chapter 2. Briefly, the mass was calculated from the total kinetic energy and the time of flight and substituted into the rigidity equation. This rigidity equation was solved for q, and the individual ionic charges were selected with software gates. The rigidity equation was then rewritten for mass using an integer value of q to produce the mass spectrum. The only difference in the present case is that the relativistic form of the equations were used because the ions had velocities that were approximately 40% of the speed of light. The mass calculated from the total energy and the time-of-flight is then:

$$A = \frac{E_{\mathrm{TOTAL}}}{931.496 \cdot (\gamma - 1)} \tag{3.12}$$

where A is in atomic mass units, and E_{TOTAL} is in MeV. This is substituted into equation 3.1, which is then solved for q:

$$B\rho = 3.10711 \beta\gamma \frac{A}{q} \tag{3.13}$$

$$q = \frac{3.10711}{931.496} \frac{E_{\mathrm{TOTAL}}}{B\rho(\gamma - 1)} \cdot \beta\gamma. \tag{3.14}$$

In the above equation, q is calculated in units of electon charge and $B\rho$ is in units of Tesla-meters. A representative q spectrum is shown in Figure 3.16 for the gallium isotopes (Z=31) at $B = 0.6453$ T. Most of the ions produced in this reaction were in the fully stripped ionic charge state, q = Z. Software gate selected those fragments with q = Z for the Z's of interest, and the masses were recalculated with the q entered

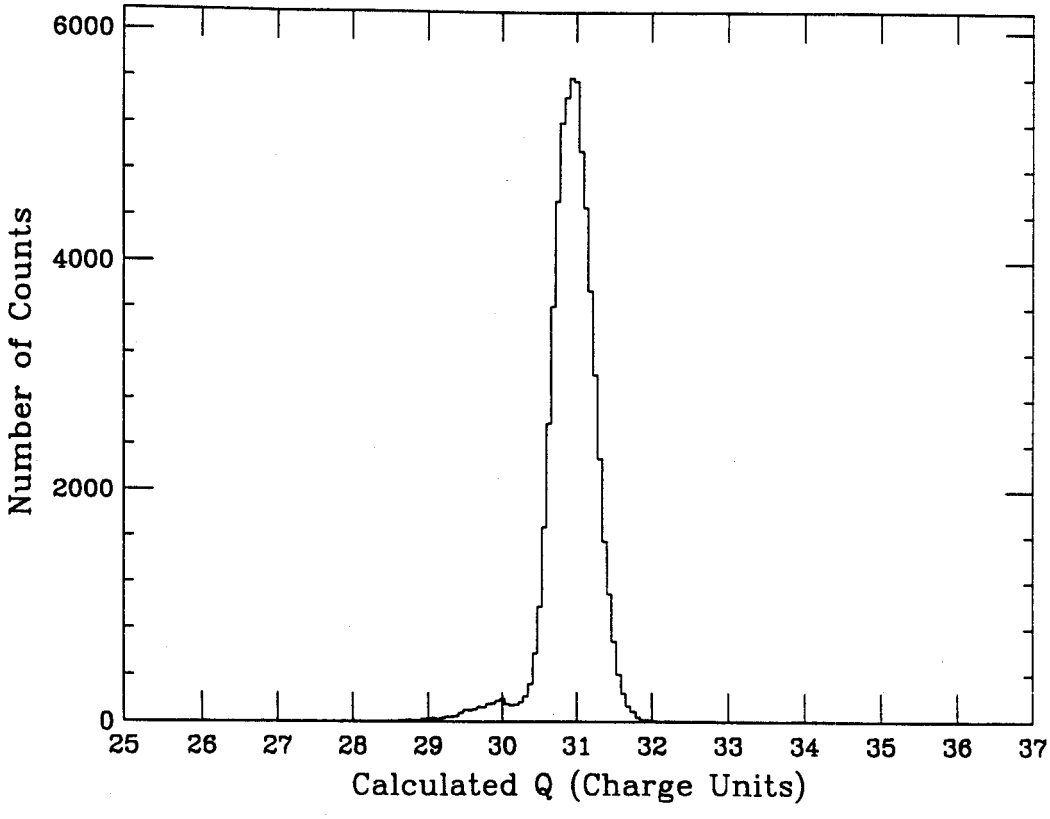

Figure 3.16: Ionic charge state spectrum for gallium isotopes.

as an integer value:

$$A = \frac{B\rho q}{3.10711\beta\gamma}, \tag{3.15}$$

giving A in atomic mass units. Figure 3.17 shows the resulting mass spectra for residues with $31 \leq Z \leq 38$. The arrows indicate nuclei identified for the first time in this work: ^{61}Ga, ^{62}Ge, ^{63}Ge, ^{65}As, ^{69}Br, and ^{75}Sr. Two events corresponding to ^{60}Ga and one event for ^{70}Kr are also observed; however, it is difficult to conclude from such a small number of events whether these nuclei were in fact identified. The observation of an isotope in the present experiment implies that the ion lives longer than its flight time through the A1200, which is of the order of 150 ns. Therefore it is possible that some of the observed nuclei are actually proton unbound with partial halflives greater than times of this order. The non-observation of an isotope in this work implies: (a) that it has a half life short compared to the flight time, (b) that its production rate was too low to make it observable, or (c) that the nucleus is not bound.

III Discussion and Conclusions

The isotope yields obtained by integrating the peaks in the mass spectra can now be compared to the calculations from the INTENSITY code. This comparison is made by calculating the production rates using the A1200 magnetic field settings, beam current, and target corresponding to those of a particular run in the experiment. The program calculates the rates at the achromatic focal plane in events - per - second, which are multiplied by the total data collection time (corrected for data acquisition dead time) to give comparable isotope yields. Figure 3.18 shows a comparison of the isotope yields for zinc through strongtium isotopes to those predicted by the INTENSITY code. The figure represents data taken at a central rigidity of 1.984 T-m ($B_{1,2} = 0.65805$T, $B_{3,4} = 0.64530$T) for 170 minutes with an average beam intensity

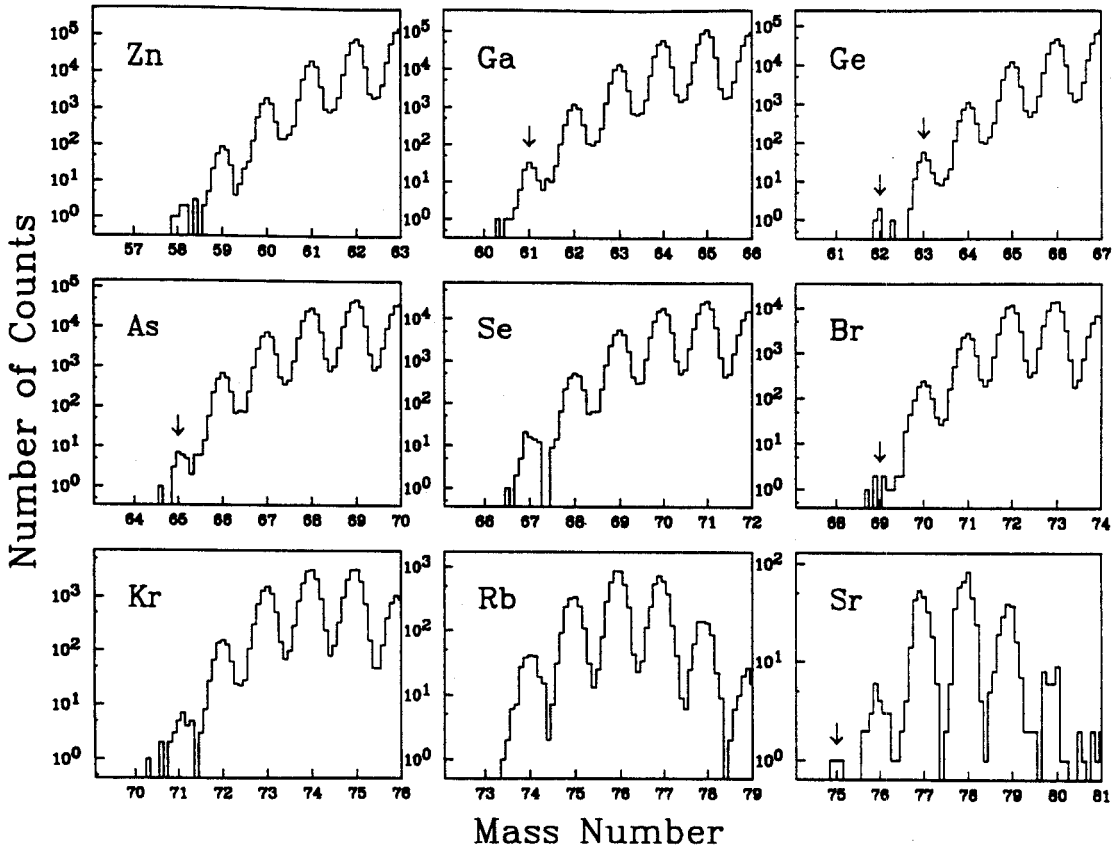

Figure 3.17: Mass spectra showing the number of counts in each mass peak for Z = 30–38 (zinc through strontium) on a logarithmic scale. The new nuclei are indicated with arrows.

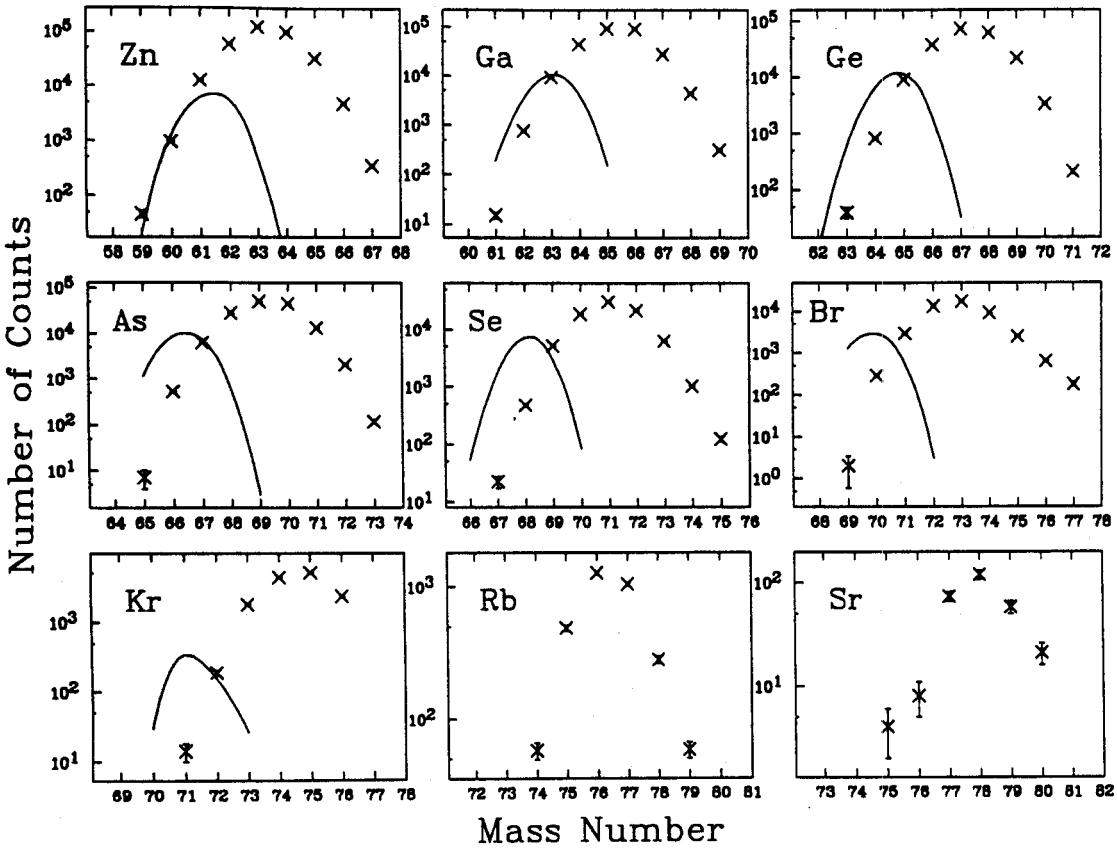

Figure 3.18: Comparison of the mass yields for zinc through strontium isotopes to the predictions of the INTENSITY code.

of 0.25 pnA on the ^{58}Ni target. The INTENSITY calculation clearly underpredicts the widths of the mass yield at this setting. Notice also that transfer products are seen which are not predicted by the parameterization of Sümmerer and Morrissey. Unfortunately, time constraints limited the ability to take systematic data at neighboring $B\rho$ settings needed to construct the momentum distributions. The momentum distributions of the products give additional information on the mechanism of residue production[mor89] and can be compared to various model predictions (see, for example, the results of the ^{86}Kr experiment of Bazin, *et al.*[ba90]).

A case can be made that ^{74}Rb is the lightest bound rubidium nucleus since there are several hundred counts in its peak, and there is not a single event attributable to ^{73}Rb. This is consistent with the previous results of D'Auria *et al.*[dau77], in which rubidium isotopes were studied in proton spallation reactions at ISOLDE.

The proton-drip line is shown as a dashed line in Figure 3.19 for one of the more reliable mass predictions [jan88] in this region, as indicated by the Haustein comparison of deviations from measured masses[ha88]. The nuclei identified for the first time in the present experiment are shown as circles in the figure. All of these isotopes are important to the rp-process (recall the detailed discussion in chapter 1). The figure also shows the mass flow calculated[woo85] for the nuclei above mass A = 56 for the particular case of the x-ray burst[lew83]. The rate at which the flow continues depends on the degree of binding of ^{61}Ga, ^{65}As and ^{69}Br. If the proton binding energy is less than 250 keV or so [ta85,ho90] photodisintegration will destroy a large fraction of these nuclei before they can be processed to higher mass nuclei. The absence of ^{73}Rb already indicates a significant slowing of the process at ^{72}Kr. In order to proceed to higher masses, ^{72}Kr must β decay to ^{72}Br so that subsequent proton captures and β decays may continue. But since the half-life of ^{72}Kr is on the order of the time of the thermonuclear explosion, there will be at least a significant slowing of the process at

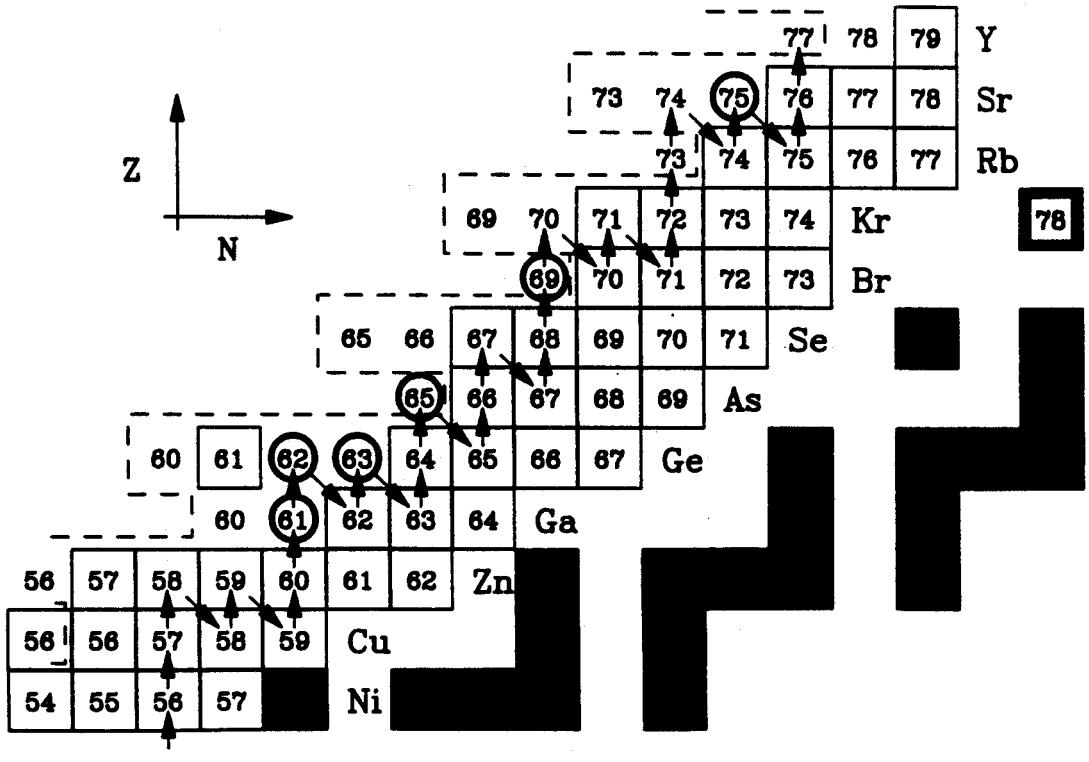

Figure 3.19: Mass flow predicted by Wallace and Woosley. Filled sqares are stable nuclei, and the projectile (^{78}Kr) is marked. Open squares are nuclei previously identified, circles indicate nuclei identified for the first time in this work. The dashed line is the drip line prediction of Jänecke and Masson [jan88].

this point.

Although the identification of ^{61}Ga, ^{65}As, ^{69}Br, and the absence of ^{73}Rb are advancements in understanding the limits of the rp-process, more information is needed about these and other nuclei along the proton-drip line. Further development of ion source technology will enable other identification experiments to be performed with neutron-deficient beams such as ^{92}Mo and ^{96}Ru. These studies will allow the proton-drip line to be mapped to higher masses and thus determine the possible pathways of the process. Also, experiments are being designed to measure the halflives of the new nuclei and obtain some information about their decay properties. The experimental setup of the A1200 will incorporate all of the components necessary in this work to identify the nuclei, with additional detectors and electronics to measure the lifetimes and distinguish whether the decay particles are protons or β^+'s. The lifetime measurements will provide information for waiting point nuclei along the dripline, which cannot capture protons and must wait for a beta or proton decay before they can be processed to higher masses. Their lifetimes are needed to calculated the flow rate to higher masses, especially since these tend to be the rate-limiting steps in the process. Finally, if the beta and/or proton decay energies can be measured, estimates of the masses of the nuclei can be made to a few hundred keV. Recall from chapter 1 that the masses are important for calculating the rate of photodissociation. Ultimately, the masses of these nuclei are needed to a few keV. However this may prove difficult experimentally, partly because the production rates are so low for some nuclei.

Chapter 4

Summary

Two methods for producing exotic nuclei of atrophysical interest were presented in this dissertation. Chapter 2 described the modifications made to the S320 spectrometer so that it could be used to identify products from the fusion/evaporation reaction of an E/A = 8 MeV ^{36}Ar beam on a ^{40}Ca target. The goals of this experiment were twofold: first, to identify any new isotopes produced in the reaction; and second, to measure the zero degree momentum distributions of the products. With such information, the the predictive powers of the model calculations could be compared and future experiments could be designed to study the decay properties of nuclei produced.

Three major modifications were made to the S320 for this work. First, a permanent magnet dipole was constructed and placed behind the target to separate the reaction products from the beam-like particles before they entered the spectrogaph aperture. This was particularly important for reducing the background rate for the zero degree measurement and also provided a means of monitoring the beam current during the experiment. Second, a start detector made of a thin-foil plastic scintillator mounted to a photomultiplier tube was installed at the aperture of the spectrometer to measure the time of flight of the nuclei to the focal plane of the spectrometer. The time of flight could not be measured against the cyclotron radio frequency since the flight times were much longer than the period between beam bursts. Third, a new

focal plane detector system was designed to detect the slow, heavy ions produced. A low-pressure multi-wire proportional counter was used to measure the position at the focal plane and to provide a prompt timing signal. This was followed by an ion chamber volume with multiple anode segments to measure energy loss and total energy, and windowless resistive wires to measure the incident angle in the detector.

The results of this experiment were quite limited because of the poor energy resolution of the ion chamber. This was attributed to contamination of the detector gas because of outgassing from components of the detector. The nuclei produced in the reaction could not be uniquely identified; however, an analysis technique was demonstrated that may provide complete isotope identification given sufficient energy loss and total energy resolution in the focal plane detectors. Some suggestions were made to improve the focal plane detector performance by eliminating the sources of outgassing in the ion chamber. This can be accomplished by eliminating shielded cables from the gas volume and drilling small holes in screw taps to remove virtual leaks. Careful consideration should be given to assembly materials and the cleanliness of the assembly environment as well. The results of Vineyard, *et al.*[vin87], have shown that such careful assembly and preparation can produce a detector with energy resolution of better than one percent.

The second method for producing exotic nuclei, discussed in chapter 3, relied on projectile fragmentation reactions. For this work an E/A = 65 MeV ^{78}Kr beam was focussed on a ^{58}Ni target, and the reaction products were collected and identified in the A1200 Mass Separator. The purpose of this experiment was to identify exotic nuclei at the proton-drip line and measure their production rates so that experiments could be designed to measure their halflives, decay modes, and masses. The A1200 was operated in the medium acceptance mode with the products identified at the achromatic focal point. A thin scintillator start detector at the first dispersive image

was used to provide a time signal relative to that from the final focus. At the second dispersive image, the position of each particle was measured with a position-sensitive parallel-plate avalanche counter. At the final focus, a silicon detector telescope was used to measure the energy loss and total energy of the nuclei, and to provide a signal to measure the time relative to the start detector. The analysis method, adapted from the work of Bazin, *et al.*[ba90], was similar to that of the fusion/evaporation experiment with the addition of relativistic corrections.

The results of this work showed that six new nuclei were identified: ^{61}Ga, ^{62}Ge, ^{63}Ge, ^{65}As, ^{69}Br, and ^{75}Sr. Two events corresponding to ^{60}Ga and one event for ^{70}Kr were also observed; however, further verification of these nuclei is necessary. The absence of ^{73}Rb supports the previous observations of D'Auria, *et al.*[dau77], that this nucleus is unbound. Future identification experiments were suggested to probe further the limits of the proton-drip line, and experiments are being planned to measure the halflives and decay modes of the new nuclei. In particular, it is important for the astrophysical rp-process of hydrogen burning that ^{61}Ga, ^{65}As, and ^{69}Br be studied.

The relative merits of the two isotope production methods illustrated in this work are difficult to compare because the results of the fusion/evaporation experiment were limited by the poor detector peformance. The isotope identification techniques were nearly identical for the two experiments, with the major difference being that the fragmentation reaction produces nuclei at a much higher velocity than the fusion/evaporation reaction. In both cases the energy loss and total energy measurements determine which elements were produced, while the rigidity, time of flight, and total energy measurements combine to determine which masses of each element were produced. However, the higher velocity (and hence higher energy) ions made in the fragmentation reactions are easier to identify and resolve with readily available detectors. The low energy fusion/evaporation products require special detectors with

relatively small dynamic energy ranges. These detectors must be carefully designed so that the unmeasured energy losses and energy loss straggling are minimized.

Certainly, from the standpoint of detector development, dynamic range, testing, and preparation time, the A1200 fragmentation experiments are much easier to perform than the S320 fusion/evaporation experiments. The results of fragmentation experiments using the LISE spectrometer in GANIL and the A1200 work presented here have shown that this technique has been very fruitful in producing both proton-rich and neutron rich exotic nuclei. Still, experimenters have been very successful using the Daresbury recoil mass separator[hot88] to identify and study the low energy nuclei produced in fusion/evaporation experiments, and a recoil mass separator is being built at the ATLAS facility at Argonne National Laboratory[dav88] for similar work. However, unless a unique situation requires the use of the fusion/ evaporation setup of the S320, the future of exotic nuclei studies at the NSCL clearly lies with the utilization of the A1200 mass separator.

References

[ann87] R. Anne, D. Bazin, A.C. Mueller, J.C. Jacmart, and M. Langevin, Nucl. Instr. and Meth. **A257**(1987)215, and references therein.

[ay82] S. Ayasli and P.C. Joss, Astrophys. Journal **256**(1982)267.

[ba90] D. Bazin, *et al.*, Nucl. Phys. **A515** (1990) 349.

[bb36] H.A. Bethe and R.F. Bacher, Rev. Mod. Phys. **8**(1936) 82.

[bib79] K. Van Bibber, D.L. Hendrie, D.K. Scott, H.H. Weiman, L. S. Schroeder, J.V. Geaga, S.A. Cessin, R. Trehauft, Y.J. Grossiord, and J.O. Rasmussen, Phys. Rev. Lett. **43**(1979)840.

[bir81] P. Birien and S. Valero, Note CEA No. 2215.

[bow74] J.D. Bowman, A.M. Poskanzer, R.G. Korteling, and G.W. Butler, Phys. Rev. **C9**(1974)836.

[br77] A. Breskin and N. Zwang, Nucl. Instr. and Meth. **144**(1977)609.

[cu34] I. Curie and F. Joliot, Nature **133**(1934)201.

[cur86] M. Curtain, L.H. Harwood, J.A. Nolen, B. Sherrill, Z.Q. Xie, and B.A. Brown, Phys Rev. Lett. **56**(1986)34.

[dau77] J.M. D'Auria, *et al.*, Phys. Lett. **66B** (1977)233.

[dav85] N.J. Davis, J.A. Kuehber, A.A. Pilt, A.J. Trudel, M.C. Vetterli, C. Bamber, E.K. Warburton, J.W. Olness, and S. Raman, Phys. Rev. **C32**(1985)713.

[dav88] C.N. Davids and B.R. Back, Technical Specifications for Electrostatic and Magnetic Elements for the Fragment Mass Analyzer at ATLAS, Argonne National Laboratory, Physics Division Specification Nos. FMA–001 to FMA–006, February 1988.

[des76] M. de Saint-Simon, L. Lessard, W. Reisdorf, L. Remsberg, C. Thibault, E. Roeckl, R. Klapish, I.V. Kuznetsov, Yu. Ts. Oganessian, and Yu. E. Penionshkevitch, Phys. Rev. **C14**(1976)2185.

[des81] M. de Saint-Simon, R. Fergeau, M. Jacotin, J.F. Kepinski , R. Klapisch, M. Langevin, and D. Guillemaud, Nucl. Instr. and Meth. **186** (1981)87.

[duf86a] J.P. Dufour, R. Del Moral, A. Fluery, F. Hubert, D. Jean, M.S. Pravikoff, H. Delgrange, H. Geissel, and K.-H. Schmidt, Z. Phys **A324**(1986)487.

[duf86b] J.P. Dufour, R. Del Moral, H. Emmermann, F. Hubert, D. Jean, M.S. Pravikoff, A. Fluery, H. Delgrange, and K.-H. Schmidt, Nucl. Instr. Meth. **A248**(1986)267.

[fae84] T. Faestermann, A. Gillitzer, K. Hartel, Pkienle, and E. Nolte, Phys. Lett. **137B**(1984)23. Also A. Gillitzer, T. Faestermann, K. Hartel, Pkienle, and E. Nolte, Z. Phys. **A326**(1987)107.

[fif85] L.K. Fifield, P.V. Drumm, M.A.C. Hotchkis, T.R. Ophel, and C.L. Woods, Nucl. Phys. **A437**(1985)141.

[fra] B. Franszak, Private communication (via B. Sherrill).

[fox] R. Fox, Private communication.

[fox89] R. Fox, R. Au, and A. VanderMolen, IEEE Trans. Nucl. Sci.(1989)1562.

[gav80] A. Gavron, Phys. Rev. **C21**(1980)230.

[gei87] H. Geissel, P. Armbruster, B. Franczak, B. Langenbeck, O . Klepper, F. Nickel, E. Roeckl, D. Schardt, K.-H. Schmidt, D. Schüll, K. Sümmerer, G. Münzenberg, J.P. Dufour, M.S. Pravikoff, H.-G. Clerc, E. Hanelt, T. Schwab, H. Wollnik, and B. Sherrill, Projectile Fragment Separator, A proposal for the SIS-ESR Experimental Program, 1987.

[gei89] H. Geissel, et al., Nucl. Instr. and Meth. **A282**(1989)247.

[gil84] R. Gilman, H.T. Fortune, L.C. Bland, R.R. Kiziah, C.F. Moore, P.A. Seidl, C.L. Morris, and W.B. Cotingame, Phys. Rev. **C30**(1984) 958.

[gil86] A. Gillibert, L. Bianchi, A. Cunsolo, B. Fernandez, A. Foti, J. Gastebois, Ch. Gregoire, W. Mittig,A. Peghaire, Y. Schutz, and C. Stephan, Phys. Lett. **176B**(1986)317.

[gil87] A. Gillibert, W. Mittig, L. Bianchi, A. Cunsolo, B. Fernandez, A. Foti, J. Gastebois, C. Gregoire, Y. Schutz, and C. Stephan, Phys. Lett. **192B**(1987)39.

[gol74] A.S. Goldhaber, Phys. Lett. **53B**(1974)306.

[goo74] D.R. Goosman and D.E. Alburger, Phys. Rev. **C10**(1974)756.

[gor87] J. Görres, T. Chapuran, D.P. Balamuth, and J.W. Arrison, Phys. Rev. Lett. **58**(1987)662.

[gor91] Joachim Görres and Michael Wiescher, private communication.

[gr76] J. Grindlay and J. Heise, Inter. Astron. Union Circular No. 2879.

[gui85] D. Guillemaud-Mueller, A.C. Mueller, D. Guerreau, F. Pougheon, R. Anne, M. Bernas, J. Galin, J.C. Jacmart, M. Langevin,F. Naulin, E. Quiniou, and C. Detraz, Z. Phys. **A322**(1985)415.

[ha52] Hauser and Feshbach, Physical Rev. **87**(1952)366.

[ha88] 1986-1987 Atomic Mass Predictions, ed. P.E. Haustein, Atomic Data and Nuclear Data Tables **39**(1988)185.

[ho75] W.F. Hornyak, Nuclear Structure, Academic Press, New York, 1975.

[ho90] W.M. Howard, *et al.*, Proceedings of the Workshop on the Science of Intense Radioactive Ion Beams, eds. J.B. McClelland and D.J. Vieira, Los Alamos National Laboratory, October, 1990, p68.

[hof82] S. Hofmann, W. Reisdorf, G. Münzenberg, F.R. Hessberger, J. R.H. Schneider, and P. Armbruster, Z. Phys. **A305**(1982)111.

[hot88] M.A.C. Hotchkis, *et al.*, Manchester Nuclear Physics Report, Schuster Laboratory, University of Manchester, Manchester, England pp. 13-16, 87-88.

[hour89] E. Hourani, *et al.*, Z. Phys. **A344**(1989)277.

[hu89] F. Hubert, R. Bimbot, and H. Gauvin, Nucl. Instr. Meth. **B36**(1989)357.

[jan88] J. Jänecke and P.J. Masson, Atomic Data and Nuclear Data Tables **39**(1988)265.

[kl82] O. Klepper, T. Batsch, S. Hofmann, R. Kirchner, W. Kurcewicz, W. Reisdorf, E. Roeckl, D, Schardt, and G. Nyman, Z. Phys. **A305**(1982)125.

[koz88] R.L. Kozub, J.F. Shriner, M.M. Hindi, R. Holzmann, R.V.F . Janssens, T.-L. Khoo, W.C. Ma, M. Drigert, U. Garg, and J.J. Kolata, Phys. Rev. **C37**(1988)1791.

[ku90] T. Kubo, M. Ishihara, T. Nakamura, H. Okuno, K. Yoshida, S . Simoura, K. Asahi, H. Kumagai, and I. Tanihata, Radioactive Nuclear Beams, The First

International Conference, eds. W.D. Myers, J.M. Nitschke, E.B. Norman, Berkeley, Ca., October,1989, World Scientific Publishing, p563.

[lan85] M. Langevin, E. Quiniou, M. Bernas, J. Galin, J.C. Macmart, C. Detraz, D. Guerreau, D. Guillemaud-Mueller, and A.C. Mueller, Phys. Lett. **150B**(1985)71.

[lan86] M. Langevin, A.C. Mueller, D. Guillemaud-Mueller, M.G. Saint-Laurent, R. Anne, M. Bernas, J. Galin, D. Guerreau, J.C. Jacmart, S.D. Hoath, F. Naulin, F. Pougheon, E. Quiniou, and C. Detraz, Nucl. Phys. **A455**(1986)149.

[lew83] W.H.G. Lewin and P.C. Joss, Accretion Driven Stellar X-Ray Sources, eds. W.Lewin, E. van den Heuvel, Cambridge Univ. Press, Cambridge, p. 41, 1983.

[lis90] C.J. Lister, *et al.*, Phys. Rev. C **42**(1990)R1191.

[mat90] G.J. Mathews, Proceedings of the Workshop on the Science of Intense Radioactive Ion Beams, eds. J.B. McClelland and D.J. Vieira, Los Alamos National Laboratory, October, 1990, p213, and references therein.

[mcm89] M.A. McMahan, R.F. Lebed, and B. Feinberg, Lawrence Berkeley Laboratory Report LBL-25930. Also presented at the 1989 IEEE Particle Accelerator Conference, Chicago, Il, March 20-23, 1989.

[mik88] D. Mikolas, B.A. Brown, W. Benenson, L.H. Harwood, E. Kashy, J.A. Nolen, B. Sherrill, J. Stevenson, J.S. Winfield, Z.Q. Xie, and R. Sherr, Phys. Rev. **C37**(1988)766.

[mj55] M.G. Mayer and J.H.D. Jensen, Elementary Theory of Nuclear Shell Structure, Wiley, New York, 1955.

[mo88] M.F. Mohar, E. Adamides, W. Benenson, C. Bloch, B.A. Brown , J. Clayton, E. Kashey, M. Lowe, J.A. Nolen, W.E. Ormand, J. van der Plicht, B . Sherrill, J. Stevenson, and J.S. Winfield, Phys. Rev. **C38**(1988)737.

[mor78] D.J. Morrissey, W.R. Marsh, R.J. Otto, W. Loveland, and G.T. Seaborg, Phys. Rev. **C18**(1978)1267, and references therein.

[mor89] D.J. Morrissey, Phys. Rev. **C39**(1989)460.

[mue90] Alex C. Mueller, private communication.

[nan80] H. Nann, K.K. Seth, S.G. Iversen, M.O. Kaltka, D.B. Barlow, and D. Smith, Phys. Lett. **B96**(1980)261.

[nn65] P. Nathan and S.G. Nilsson, Alpha-, Beta-, and Gamma-Ray Spectroscopy. K. Siegbahn, ed. North Holland, Amsterdam, 1965.

[nor87] E. Norbeck, R. Dubbs, and L. Sobotka, Nucl. Instr. and Meth. **A262**(1987)546.

[nor70] L.C. Northcliffe and R.F. Schilling, Atomic and Nuclear Data Tables **7**(1970)1.

[ope89] R. Openshaw, R. Henderson, W. Fraszer, D. Murphy, M. Salomon, and G. Sheffer, IEEE Transactions on Nuclear Science **36**(1989)567 .

[pan81] A.D. Panagiotou, I. Paschopoulos, A. Huck, and N. Schulz , Phys. Lett. **103B**(1981)297.

[pla78] F. Plasil, Phys. Rev. **C17**(1978)823.

[pou86] F. Pougheon, D. Guillemaud-Mueller, E. Quiniou, M.G. Saint-Larent, R. Anne, D. Bazin, M. Bernas, D. Gerreau, J.C. Jacmart, S.D. Hoath, A.C¿ Mueller, and C. Detraz, Europhys. Lett **2**(7)(1986)505.

[pou87] F. Pougheon, J.C. Jacmart, E. Quiniou, R. Anne, D. Bazin, V. Borrel, J. Galin, D Guerreau, D. Guillemaud-Mueller, A.C. Mueller, E. Roeckl, M.G. Saint-Laurent, and C. Detraz, Z. Phys. **A327**(1987)17.

[pu77] F. Puhlhofer, Nucl. Phys. **A280**(1977)267.

[rei76] W. Reisdorf, M. de Saint-Simon, L. Reisdorf, L. Lessard, C. Thibault, E. Roeckl, and R. Klapisch, Phys. Rev. **C14**(1976)2189.

[ri80a] P. Ring and P. Schuck, The Nuclear Many-Body Problem, Springer Verlag Press, New York, 1980, p4.

[ri80b] P. Ring and P. Schuck, The Nuclear Many-Body Problem, Springer Verlag Press, New York, 1980, p44.

[ri80c] P. Ring and P. Schuck, The Nuclear Many-Body Problem, Springer Verlag Press, New York, 1980, p15.

[ro90] J.D. Robertson, J.E.Reiff, T.F. Lang, D.M. Moltz, and J. Cerny, Phys. Rev. C **42**(1990)1922.

[sch84] J.P. Achapira, F. Azaiez, S. Fortier, S. Gales, E. Hourani, J. Kumpulainen, and J.M. Maison, Nucl. Instr. and Meth. **A224**(1984)337.

[sch87] K.-H. Schmidt, et al., Nucl. Instr. and Meth. **A260** (1987)287.

[sco74] D.K. Scott, B.G. Harvey, D.L. Hendrie, L. Krauss, C.F. Maguire, J. Mahoney, Y. Terrien, and K. Yagi, Phys. Rev. Lett. **33**(1974) 1343.

[set78] K.K. Seth, H. Nann, S. Iversen, M. Kaletka, J. Hird, and H.A. Thiessen, Phys. Rev. Lett. **41**(1978)1589.

[sh85] B. Sherrill, Doctoral Dissertation, 1985; B. Sherrill, K. Beard, W. Benenson, C. Bloch, B.A. Brown, E. Kashy, J.A.Nolen, A.D. Panagiotou, J. van der Plicht, and J.S. Winfield, Phys. Rev. **C31**(1985)875.

[sh90] B.M. Sherrill, W. Benenson, D. Mikolas, D.J. Morrissey, J. A. Nolen Jr., and J.A. Winger, Proceedings of the International Conference on Accelerator Applications, Denton, Texas, Nov. 1990, Nucl. Instr. and Meth., in press. See also Radioactive Nuclear Beams, The First International Conference, eds. W.D. Myers, J.M. Nitschke, E.B. Norman, Berkeley, Ca., October,1989, World Scientific Publishing, p. 72.

[sue90] K. Suemmerer, et al., Phys. Rev. **C42**(1990)2546. See also D.J. Morrissey and K. Suemmerer, Proceedings of the First International Conference on Radioactive Nuclear Beams, October 16-18, 1989, Berkeley, California, J.M. Nitschke, ed.

[sym79] T.J.M. Symons, Y.P. Viyogi, G.D. Westfall, P. Doll, D.E. Greiner, H. Faraggi, P.J. Lindstrom, D.K. Scott, H.J. Crawford, and C. McParland, Phys. Rev. Lett. **42**(1979)40.

[ta85] R.E. Taam, Ann. Rev. Nucl. Sci.**35**(1985)1.

[tho84] C.E. Thorn, J.W. Olness, E.K. Warburton, and S. Raman, Phys. Rev. **C30**(1984)1442.

[uno82] M. Uno and M. Yamada, INS Report NUMA-40 (1982).

[vie86] D.J. Vieira, J.M. Wouters, K. Vaziri, R.H. Kraus, H. Wollnik, G.W. Butler, F.K. Wohn, and A.H. Wapstra, Phys. Rev. Lett. **57**(1986)3253.

[vin87] M.F. Vinyard, B.D. Wilkins, D.J. Henderson, D.G. Kovar, C. Beck, C.N.

Davids, and J.J. Kolata, Nucl. Instr. and Meth. **A255**(1987) 507. Also, private communications with J.J. Kolata regarding recent progress.

[wes79] G.D. Westfall, T.J.M. Symons, D.E. Greiner, H.H. Heckmann, P.J. Lindstrom, J. Mahoney, A.C. Shotter, D.K. Scott, H.J. Crawford, C¿ McParland, T.C. Awes, C.K. Gelbke, and J.M. Kidd, Phys. Rev. Lett. **43**(1979)1859.

[wie91] M. Wiescher, L. Van Wormer, J. Görres, and F.K. Thielemann, Procedings of the Second International Conference on Radioactive Nuclear Beams, Louvain-la-Neuve, Belgium, August 19-21, 1991, to be published.

[wil73] K.H. Wilcox, N.A. Jelley, G.J. Wozniak, R.B. Weisenmiller, H.L. Harvey, and J. Cerny, Phys. Rev. Lett. **30B**(1973)866.

[win91a] J.A. Winger, D.J. Morrissey, and B. Sherrill, 1990 National Superconducting Cyclotron Laboratory Annual Report.

[win91b] J.A. Winger, unpublished results.

[wa81] R.K. Wallace and S.E. Woosley, Astrophys. Journ. Suppl. **45**(1981)389.

[wa84] R.K. Wallace, High Energy Transients in Astrophysics, AIP conference proceedings No. 115, Santa Cruz, 1984, p.319.

[we35] C.F. von Weizsäcker, Z. Phys. **96**(1935)431.

[win90] J.S. Winfield and J. van der Plicht, The S320 Manual, revised 1990. See also B.M. Sherrill, Doctoral Dissertation, 1985.

[wod85] C.L. Woods, L.K. Fifield, R.A. Bark, P.V. Drumm, and M.A .C. Hotchkis, Nucl. Phys. **A437**(1985)454.

[wod86] P.J. Woods, R. Chaoman, J.L. Durell, J.N. Mo, R.J. Smith , B.R. Fulton, R.A. Cunningham, P.V. Drumm, and L.K. Fifield, Phys. Lett. **182B**(1986)297.

[woo76] S.E. Woosley and R.E. Taam, Nature **263** (1976)101.

[woo85] S.E. Woosley, Proceedings of the Accelerated Radioactive Beams Workshop, eds. L. Buchmann, J.M. D'Auria, Parksville, Canada, TRIUMF Report TRI-85-1, p.4, 1985, and references therein.

[zie85] J.F. Ziegler, J.P. Biersack, and U. Littmark, The Stopping Power and Range of Ions in Solids, Volume 1 of The Stopping and Ranges of Ions in Matter, Pergamon Press, J.F. Ziegler, ed., 1985.